

EXPERIMENTAL CHARGE DENSITY STUDIES OF HIGHLY POLAR BONDS

Dissertation zur Erlangung des
naturwissenschaftlichen Doktorgrades
der Bayerischen Julius-Maximilians-Universität Würzburg

vorgelegt von
Nikolaus Kocher
aus Gunzenhausen

Würzburg 2003

Eingereicht am: _____

bei der Fakultät für Chemie und Pharmazie

1. Gutachter: _____

2. Gutachter: _____

der Dissertation

1. Prüfer: _____

2. Prüfer: _____

3. Prüfer: _____

des öffentlichen Promotionskolloquiums

Tag des öffentlichen Promotionskolloquiums: _____

Doktorurkunde ausgehändigt am: _____

There can be no doubt that when a compound has to be identified there is nothing to beat a crystal structure determination (...) The final outcome – a drawing of the molecule, (...) will silence all but the most stubborn critics!

Kenneth N. Trueblood

Danksagung

Die vorliegende Arbeit wurde in der Zeit von September 2000 bis November 2003 im Arbeitskreis von Prof. Dr. D. Stalke am Institut für Anorganische Chemie der Universität Würzburg angefertigt. An dieser Stelle soll allen Dank ausgesprochen werden, die zum Gelingen dieser Arbeit beigetragen haben.

Die Arbeit an dieser interessanten und kontrovers diskutierten Thematik war eine große Herausforderung für mich. Mein besonderer Dank gilt daher Herrn Prof. Dr. Dietmar Stalke, der mir dieses Thema vorgeschlagen hat. Die stetige Diskussionsbereitschaft in ausgesprochen freundschaftlicher Atmosphäre sowie die Unterstützung in allen anderen Bereichen sind dabei ebenso hervorzuheben wie die große wissenschaftliche Freiheit bei der Bearbeitung des Themas und die Ermöglichung der Teilnahme an nationalen und internationalen Konferenzen.

Allen gegenwärtigen und ehemaligen Arbeitskreismitgliedern danke ich für die Unterstützung sowie das hervorragende Arbeitsklima, das den Laboralltag nie wirklich zu diesem werden ließ. Namentlich danke ich:

Der Muddi (verschiedenen Firmen, die Preise vergeben auch bekannt unter dem Namen Dr. Dirk Leusser) für die herausragende Zusammenarbeit während der gesamten drei Jahre. Ob Elektronendichteverteilung, Diffraktometer, Fahrradtouren, Camping-ausrüstung oder Schnäppchenjagd bei Decathlon – in allen Bereichen hat er durch sein Interesse bemerkenswerte Beiträge geliefert warum sich jemandem die Faltung einer Funktion oder eine Fouriertransformation leichter erschließt als ein 4-bindiges Kohlenstoffatom, bleibt mir allerdings immer noch ein Rätsel...

Unserem Computer-Koreaner Hwan Jeong für die außergewöhnliche Leistung, das Linux-System so zu konfigurieren, dass alle nötigen Programme für die Arbeit stabil gelaufen sind.

Den Synthetikern Dr. Carola Selinka, Alexander Murso und Katja Strohfeld für die Geduld bei der Bereitstellung von Einkristallen ihrer Verbindungen, ohne die diese Arbeit nicht möglich gewesen wäre.

Thomas Stey (AkR *in spe*) für die Entlastung in allen Bereichen der Arbeit mit den Lehramt-StudentInnen. In diesem Zusammenhang auch ein großes Dankeschön an Frau Kromm und Herrn Kilian für die tolle Unterstützung bei der Durchführung der Lehramtpraktika.

Unserem Neu-Diplomanden Stephan Deuerlein für die Hilfe bei Computerproblemen in der Endphase der Arbeit.

Prof. Dr. D. Kost und seiner Arbeitsgruppe von der Ben-Gurion University of the Negev in Beer-Sheva, Israel, für die unkomplizierte und effektive Zusammenarbeit.

Verschiedenen Angestellten unseres Institutes bin ich zu besonderem Dank verpflichtet. Die Herren Alfred Schertzer (Hauswart), Wolfgang Obert (Elektronik), Alois Ruf (Schlosserei) und Manfred Reinhart (Feinmechanik) haben mit Geduld und Einfallsreichtum immer eine Lösung für meine Sonderwünsche bzgl. Modifikationen am Einkristalldiffraktometer oder Stereomikroskop gefunden.

Mein ganz herzlicher Dank gilt meiner Mutter, meinem Vater und meiner Freundin, Mara Götz, für die nicht enden wollende Geduld den Abschluss meiner Ausbildung abzuwarten (...to be continued...)

Contents

1	Introduction.....	1
2	Theoretical Background.....	7
2.1	Principles	7
2.2	Independent Atom Model (IAM).....	8
2.3	Multipole Model	9
2.4	Functions and Moments derived from the Charge Density Distribution.....	11
2.4.1	Deformation Density.....	11
2.4.2	Electrostatic Potential	11
2.4.3	Dipole Moment	12
2.5	Theory of “Atoms in Molecules” (AIM)	13
2.5.1	Critical Points	13
2.5.2	The Laplacian	15
2.5.3	Electronic Energy Density	15
2.5.4	Integration over Topological Basins.....	16
2.5.5	Classification of Bonds.....	17
3	Experimental Section.....	20
3.1	Data Collection	20
3.2	Data Processing.....	22
3.3	Refinements	23
3.3.1	IAM Refinement	23
3.3.2	Multipole Refinement	24
3.3.3	Testing the Results.....	25
4	Methodical Development – Multipole Refinement of a Twinned Sample	28
4.1	Refinement Strategy	30
4.2	Structure Discussion	33
4.3	Discussion of Electronic Properties.....	36

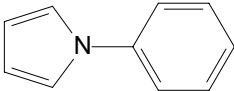
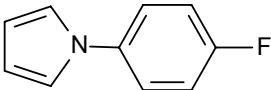
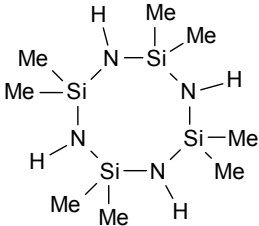
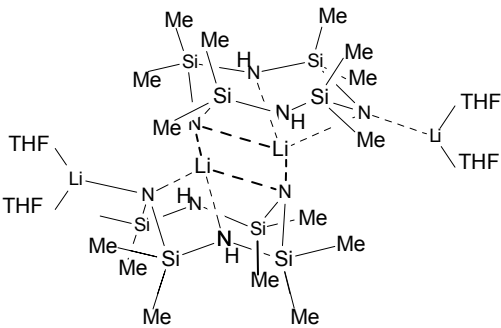
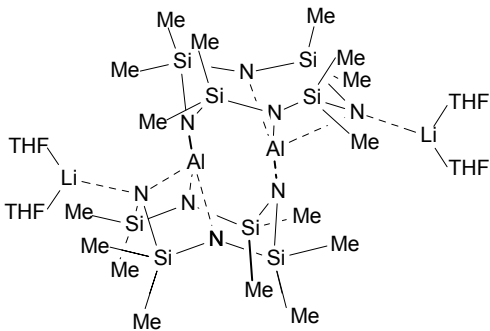
5	Results and Discussion	43
5.1	Multipole Refinement and Topological Analysis of Highly Polar Bonds	43
5.2	Charge Density Studies on Compounds containing Si–N Bonds	44
5.2.1	Si–N in Tetracoordinated Silicon Compounds.....	45
5.2.1.1	Molecular Structures	46
5.2.1.2	Multipole Refinement	51
5.2.1.3	Topological Analysis.....	59
5.2.1.4	Molecular Properties from the Charge Density Distribution	71
5.2.2	Si–N in a Hexacoordinated Organosilicon Compound	75
5.2.2.1	Molecular Structure.....	75
5.2.2.2	Multipole Refinement	76
5.2.2.3	Topological Analysis.....	77
5.2.2.4	Molecular Properties from the Charge Density Distribution	84
5.3	Charge Density Study on a Lithiated Picolylphosphane.....	86
5.3.1	Molecular Structure.....	86
5.3.2	Multipole Refinement	87
5.3.3	Topological Analysis.....	91
5.3.4	Molecular Properties from the Charge Density Distribution	95
5.4	Comparison of E–N (E = Al, Si, P, S) Bonds	97
5.5	Charge Density Study on <i>tert</i> -Butyllithium-(–)-Sparteine	100
5.5.1	Molecular Structure.....	101
5.5.2	Multipole Refinement	102
5.5.3	Topological Analysis.....	106
5.5.4	Molecular Properties from the Charge Density Distribution	109
5.6	Comparison of Li–E (E = C, N, O) Bonds	110
6	Conclusion.....	115
7	Zusammenfassung.....	118
8	References	122

Abbreviations

ADP	anisotropic displacement parameter
AIM	atoms in molecules
at	atomic
BCP	bond critical point
CC	charge concentration
CCD	charge coupled device
CD	charge density
CP	critical point
CSD	Cambridge structural database
DMSDA	differences of mean-square displacement amplitudes
ED	electron density
eq	equation
esd	estimated standard deviation
ESP	electrostatic potential
GoF	goodness of fit
IAM	independent atom model
iso	isotropic
IUCr	international union for crystallography
kin	kinetic
LP	lone-pair
max	maximum
Me	methyl
min	minimum
MO	molecular orbital

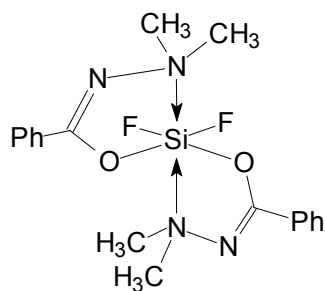
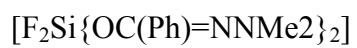
MSDA	mean-square displacement amplitude
no.	number
obs	observed
param	parameters
Ph	phenyl
pot	potential
R	residual
RCP	ring critical point
refl	reflections
SF	scaling factor
<i>t</i> Bu	<i>tert.</i> -butyl
<i>n</i> BuLi	<i>n</i> -butyllithium
<i>t</i> BuLi	<i>tert</i> -butyllithium
THF	tetrahydrofuran
VSCC	valence shell charge concentration

Compounds

no.	Compound	Lewis diagram
I	N-phenylpyrrole $C_{10}H_9N$	
II	N-(4-fluorophenyl)pyrrole $C_{10}H_8NF$	
III	Octamethylcyclotetrasilazane (OMCTS) $[c\text{-}\{Me_2Si\text{-}N(H)\}_4]$	
IV	Dilithioctamethyl- cyclotetrasilazane (dianion) $[(thf)_2Li_2\text{-}c\text{-}\{Me_2Si\text{-}N(H)\text{-}Me_2Si\text{-}N\}_2]_2,$	
V	Alumolithioctamethyl- cyclotetrasilazane (tetraanion) $[(thf)_2LiAl\text{-}c\text{-}\{Me_2SiN\}_4]_2$	

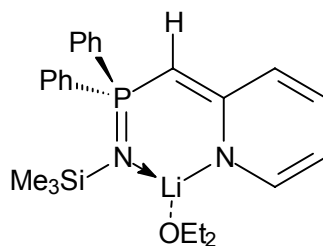
VI

Difluoro-bis-[N-(dimethylamino)-
phenylacetimidato-N,O]silicon



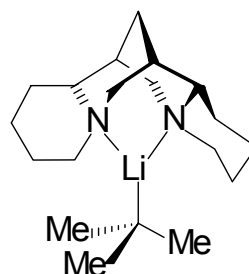
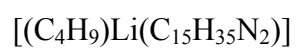
VII

Lithiated Picolylphosphane



VIII

*t*BuLi·(-)-sparteine



1 Introduction

Knowledge of the molecular structure is one of the fundamental aims of chemistry and essential for a proper understanding of the chemical and physical properties of materials. Therefore, X-ray structure analysis has become the most important analytical tool in chemistry. Since the first diffraction experiment, performed from Laue, Friedrich and Knipping in 1912 to prove the electromagnetic nature of X-rays¹ and the first structure determination by Bragg,² the technique of X-ray structure determination has changed dramatically. Tremendous progress has affected all parts of this field. Innovation of low-temperature devices for crystal application and data collection extended the method to very sensitive samples.³ The two major improvements in the last decade were the development of area detectors and the improving computing power. The first reduces considerably the time for the diffraction experiment, the latter accelerates the data processing, including the final structure refinement.

However, the vast majority of current X-ray structure determinations still use the spherical-atom assumption, assigning the maxima of the electron density to nuclear positions. This approach is limited to the determination of atomic positions and the evaluation of distances and angles between the coordinates associated to this positions. Nevertheless, the electron density distribution in a crystal is not only made up of spherical contributions around the atomic core. Aspherical distributions of the valence shell caused from chemical bonding or intra- and intermolecular interactions are also present and accessible from a diffraction experiment. In 1971, Hirshfeld developed a formalism to obtain information related to chemical bonds from diffraction methods.⁴ Since the late 70s, another model, the Hansen-Coppens multipole formalism,⁵ has gained general acceptance to derive extensive information from a diffraction experiment. The formalism allows not only to get more exact atomic positions but supplies much more detailed information about the electron density in the crystal including aspherical bonding densities. Physical properties like the dipole moment or the electrostatic potential are directly available from experiments exploiting this approach. A monograph from Coppens describes the method in detail.⁶ The recent research on this topic is summarized in reviews from Spackman⁷ and Koritsanszky.⁸

In addition, employment of Bader's quantum theory of 'Atoms in Molecules' (AIM)⁹ yields topological properties of the electron density distribution derived from the

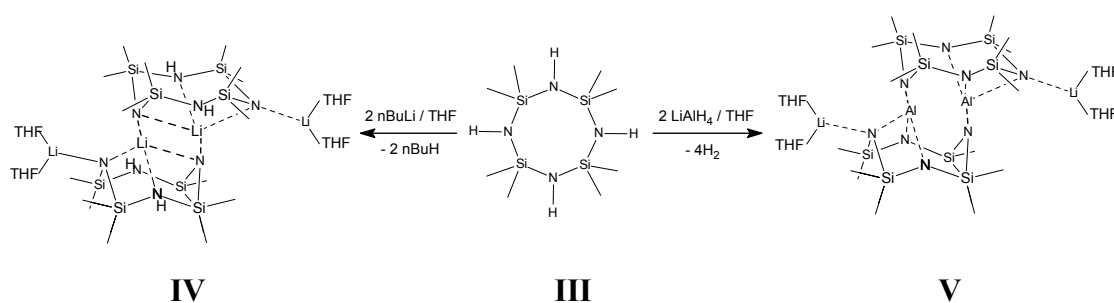
multipole model, which allow the classification of chemical bonds. Hence, electron density in a crystal, spherical and aspherical contributions, determining the physical and chemical properties of a molecule, is an observable within an X-ray diffraction experiment.

The multipole formalism and subsequent topological analysis was introduced to our research group by Leusser¹⁰. A major part of his work was the optimization of the diffraction experiment and the data processing strategy. The established procedure was tested by the topological analyses of S–N bonds in polyimido sulfur compounds.¹¹ This study was mainly based on the second derivative of the electron density, the Laplacian, and its spatial distribution as well as on the topological properties at an important point in Bader's AIM theory, the so called 'bond critical point'. In the present thesis, the analysis of the charge density distribution includes additional properties like the electrostatic potential and the examination is no longer limited to the bond critical point. The topological properties of the interesting bonds are monitored along the whole bond path or in the total space related to an atom. While the early charge density studies were focused on organic compounds and bonding characteristics of C–C bonds,⁸ the application is now open for a greater variety of chemical systems. However, only very few studies on highly polar bonds containing a third-row element and on metal–non-metal interactions with a main group metal are published. Hence, this thesis is focussed on the two latter bonding types to further extend the limits of the method. The challenge was to classify the bonds in terms of shared and closed-shell interactions with dominant covalent or ionic contributions, respectively, with the properties available from charge density analyses.

In addition to the analysis of highly polar bonds, the first chapter in this thesis comprises a methodical development. Normally, the aspherical atom formalism is restricted to high-class single crystals because of their higher scattering power, leading to Bragg reflections to a resolution of $\sin\theta/\lambda_{\max} \geq 1.0\text{\AA}^{-1}$. Normally, dealing with low quality data would not result in convergent refinement due to numerous parameters and correlations during the refinement procedure. Chapter 4.1 deals with the refinement of a twin, namely not a single crystal and thus not of the required 'high-class' at all. However, this chapter documents that the multipole algorithm is suitable to identify and refine twinning successfully. The results of the structure determination of twinned N-phenylpyrrole, **I**, are compared to the closely related 4-Fluoro-(N-phenylpyrrole), **II**, which is assumed to have similar topological properties. Compound **I** and **II** were synthesised from Zachariasse et al.

Two types of novel compounds synthesised and crystallized in our research group are silicon-nitrogen and phosphorus-nitrogen complexes. There is a constant vigorous debate about the nature of the E–N (E = Si, P) bonds in these compounds. Some answers are provided with theoretical approaches,¹² but experimental studies are rare or even missing.¹³ Obviously, the nature of bonding is directly related to the electron density distribution. Therefore, a multipole refinement based on experimental data is the key experiment to elucidate the bonding.

The solid-state structure of octamethylcyclotetrasilazane (OMCTS), **III**, is known since the early 60s.¹⁴ With numerous Si–N bonds this compound is ideal for an investigation of the Si–N bonding type. Since the oligo- and polysilazanes (RR'SiNR'')_n are known to yield Si₃N₄ ceramics on pyrolysis,¹⁵ cyclic silazanes like OMCTS and its derivatives are particularly interesting as potential precursors as well.¹⁶ Metallated OMCTS is a promising precursor to multinary materials based on Si₃N₄ such as nitridosilicates.¹⁷ The deprotonation and metallation of OMCTS is only achieved with strong bases as deprotonating agents. Reaction of OMCTS, **IV**,¹⁸ with *n*-butyllithium yields the dilithiated dianion, employment of LiAlH₄ gives the fully deprotonated OMCTS as a tetraanion, **V**. The chemical reactions are presented in Scheme 1.1. A complete homologous series of alkalimetallated derivatives of OMCTS, **III**–**V**, was published by Stalke et al.¹⁹ and saved for a detailed study of the Si–N bonding type. From this series not only the Si–N bonding can be evaluated, but the changes in the electron density distribution of this bonding type after deprotonation at the nitrogen atom are further accessible.



Scheme 1.1 Synthesis of the dianion, **IV**, and the tetraanion, **V**, from the parent OMCTS, **III**.

Si–N bonds are also present in numerous hexacoordinated organosilicon compounds synthesised by Kost et al.²⁰ Hexacoordinated difluorobis[N-(dimethylamino)phenyl-acetimidato-N,O]silicon,²¹ **VI**, is a convenient example with three different highly polar bonds at the central silicon atom. The results of the studies on the Si–N bond of the

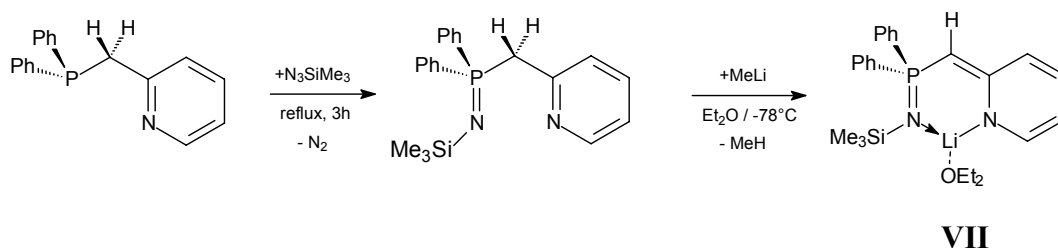
tetracoordinated silicon in **III-V** are compared to the Si–N bond of this hexacoordinated silicon atom with different geometrical properties.

For more than two decades there is general interest in silicon compounds with more than four substituents at the central silicon atom due to another fact: the dispute whether this silicon is hypervalent or high-coordinated is a paradigmatic case where the presence or absence of a bond is believed to be deducible from merely geometrical features extracted from routine structure determinations.²² This problem, as well as the Si–N bonding, is tackled with the charge density studies of this thesis.

Naturally, the concept of hypervalency in molecules, which hold more than eight valence electrons at the central atom, is a topic of constant debate not limited to silicon compounds. Since the landmark work of Wittig and Staudinger on phosphonium ylides²³ and iminophosphoranes,²⁴ respectively, these isoelectronic analogues of phosphaneoxides are well established species in organometallic and organic syntheses.²⁵ Particularly the Wittig reaction and its extensions play an outstanding role in the (stereo)selective transformation of ketones and aldehydes to olefins. The P=N bond in polyphosphazenes is known to be thermally very robust and gives access to inert polymeric materials, but the Si–N bond in silylated iminophosphoranes of the general type $R_3P=NSiMe_3$ can easily be cleaved in reactions with main group-²⁶ or transition metal-halides,²⁷ leading to phosphoraneiminato complexes, containing the $[R_3PN]^-$ - building block. Recently, Stephan et al. proved the high catalytic activity of these complexes towards ethylene polymerisation.²⁸ Consequently, P=E bonding (E = C, N, O) is an issue of experimental and theoretical debate because of the chemical importance of ylides, iminophosphoranes and phosphaneoxides.²⁹

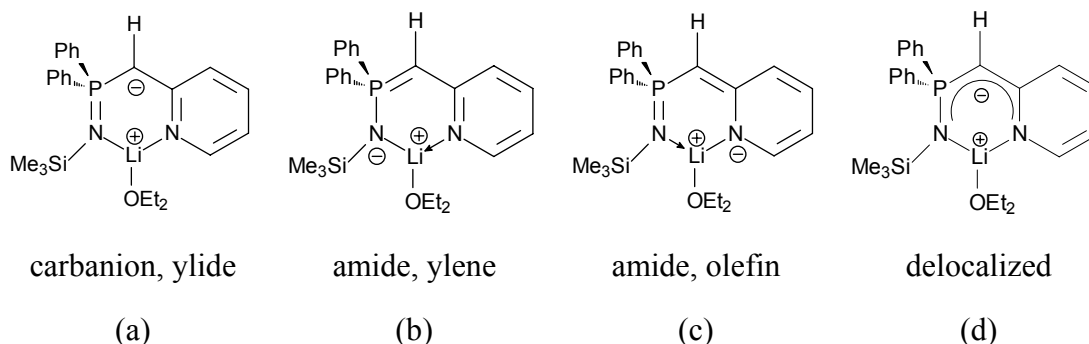
Phosphorus based ligand systems with one or more donating atoms in the periphery gain increasing importance in catalysis and in the design of self assembling ligands.³⁰ The incorporation of heteroaromatic substituents at the phosphorus centre instead of common alkyl and phenyl groups alters and augments the coordination capability of the ligand system and leads to the design of multidentate *Janus head* ligands.³¹ The common features of these ligands are acidic protons which open the way to generate delocalized monoanionic species.³² The concept of side-arm donation, which has already proved to be useful in various catalytic reactions involving hard/soft coordination site selective chelating phosphanes³³ can also be achieved *via* ring heteroatoms. Introduction of alkyl bridges between the phosphorus atom and the heterocycle in iminophosphoranes leads to higher geometrical adaptability and a higher degree of delocalization.

Combining both concepts, we synthesised the lithiated phosphorus complex $[(Et_2O)Li\{Ph_2P(ChPy)(NSiMe_3)\}]$, **VII**, depicted in Scheme 1.2.³⁴

Scheme 1.2 Synthesis of **VII**.

The geometrical features of **VII** suggest canonical formulae as depicted in Scheme 1.3. However, all of them require valence expansion at the phosphorus atom, not obeying the eight electron rule, but chemical reactivity neither supports P=N nor P=C double bonds because both are easily cleaved in various reactions.

The question whether the phosphorus atom is hypervalent can be answered by investigating the character of the P–E (E = C, N) bonds by means of direct determination of the electron density distribution and subsequent topological analysis.



Scheme 1.3 Resonance forms of $[(\text{Et}_2\text{O})\text{Li}\{\text{Ph}_2\text{P}(\text{CHPy})(\text{NSiMe}_3)\}]$, **VII**: (a) indicates a carbanionic ylidic contribution; (b) shows the amidic ylenic resonance structure; (c) emphasizes the amidic olefinic resonance form and (d) visualizes the delocalization of the negative charge.

Experimental charge density studies on highly polar metal–non-metal Li–E (E = C, N, O) and Al–N contacts, present in several compounds discussed in this thesis, are very rare in literature.³⁵ Theoretical results differ remarkably concerning the ionic contributions in these bonding types.³⁶ Therefore, the metal–non-metal interactions Li–E (E = N, O) and Al–N of the samples **IV**, **V** and **VII** are investigated in detail. The electronic features of the Li–C bonds are deduced from the lithium–carbon bond in the solid-state structure of *t*BuLi(–)-sparteine, **VIII**, the first crystal structure with monomeric *tert*-butyllithium, recently synthesised by Strohmman et al.³⁷

Topological analysis of the experimentally determined charge density provides a powerful tool to elucidate the nature of the bonding far beyond bond lengths and angles consideration. The results of the multipole refinements and topological analysis of the highly polar bonds in **III-VIII** are summarized and compared at the end of this thesis. Hereby, one chapter contains the properties of the third-row elements bonded to nitrogen E–N (E = Al, Si, P, S), the other the Li–E' (E' = C, N, O) contacts.

2 Theoretical Background

2.1 Principles

X-ray structure determinations are based on intensity measurements of X-ray beams elastically scattered (diffracted) by crystals. From the position of this intensity I it is possible to determine its index triple (h, k, l) . Based on the diffraction pattern obtained from X-ray scattering of the periodic assembly of molecules or atoms in the crystal, the electron density can be reconstructed. The question arises, how to get from the diffraction data to a model of the structure? There is a relationship between the observed X-ray intensities and the scattering amplitudes F . The intensities of the diffraction pattern and the arrangement of atoms in the unit cell of the crystal structure are related to each other by Fourier transformation: the diffraction pattern is the Fourier transform of the electron density and *vice versa*. According to the kinematical theory of scattering,³⁸ the scattering amplitudes are related to the observed X-ray intensities as follows:

$$I \sim |F(\mathbf{H})|^2, \quad (2.1)$$

where the scattering vector \mathbf{H} is given by $\mathbf{H} = h\mathbf{a}^* + k\mathbf{b}^* + l\mathbf{c}^*$ with integral components with respect to the reciprocal axes. Within this theory the scattering amplitude of the diffracted beam is the Fourier transform of the static electron density in the crystal defined as:

$$F(\mathbf{H}) = \int_V \rho(\mathbf{r}) \exp(2\pi i \mathbf{H} \mathbf{r}) d\mathbf{r}, \quad (2.2)$$

where F is the structure factor.

The structure factor can be simplified by approximating the electron density of the crystal by a summation over atomic densities, each centered at the nuclear position \mathbf{r} :

$$\rho(\mathbf{r}) = V^{-1} \sum_{\mathbf{H}} F(\mathbf{H}) \exp(-2\pi i \mathbf{H} \mathbf{r}), \quad (2.3)$$

where $\rho(\mathbf{r})$ is the electron density (ED), also referred to as the electronic charge density. This direct evaluation of $\rho(\mathbf{r})$ is subject to a number of restrictions:

- experimental errors of the observed structure factors
- only a finite number of reflections can be collected in the experiment

- the information about the phases is lost during the measurement (phase problem)

Due to these limitations the interpretation of X-ray data involves modelling the ED and optimizing its parameters by adjusting the calculated structure factors (F_c) to those observed (F_o) in a least square procedure.

In the diffraction analysis the electron density is averaged over pure vibrational states.³⁹ This thermal average can be expressed within the convolution approximation⁴⁰ according to which the total ED is described as a superposition of density following the motion of the nucleus it is attached to.

In the harmonic approximation the thermal motion is described by a probability distribution function:

$$P_0(\mathbf{u}) = (2\pi)^{-3/2} (\det \mathbf{U})^{-1/2} \exp(-1/2 \mathbf{u}' \mathbf{U}^{-1} \mathbf{u}), \quad (2.4)$$

where \mathbf{u} is the nuclear displacement vector and \mathbf{U} the mean square displacement amplitude (MSDA), respectively.

Sometimes, the thermal vibration is insufficiently described by the harmonic approximation. The Gram-Charlier expansion⁴¹ is a model that can serve for small anharmonicities. In this approach the anharmonic motion is described as:

$$P(\mathbf{u}) = \left(1 + \frac{1}{3!} C_{jkl} H_{jkl} + \frac{1}{4!} C_{jklm} H_{jklm} + \dots \right) P_0, \quad (2.5)$$

where the $H_{jkl(m)}$ are the tree-dimensional Hermite polynomials, which are functions of \mathbf{U} and \mathbf{u} . The expansion coefficients $C_{jkl(m)}$ denote the refined moments in the least squares procedure.

Different approaches for the structure factors F ,

$$F(\mathbf{H}) = \sum_q f_q(\mathbf{H}) t_q(\mathbf{H}) \exp(2\pi i \mathbf{H} \mathbf{r}_q), \quad (2.6)$$

where $f_q(\mathbf{H})$ is the scattering factor and $t_q(\mathbf{H})$ denotes the temperature factor, respectively, lead to two atomic models used in the refinement procedures - a simple spherical independent atom model (IAM) and a more flexible multipole model

2.2 Independent Atom Model (IAM)

Within this conventional approach the atomic ED is described as superposition of sperical atomic densities. The IAM does not take into account any deformation of the ED due to chemical bonding or lone-pair densities. The more dominant the core scattering relative to the valence scattering, the better the approximation this IAM

provides. For light atoms, however, the neglect of directional characteristics biases the interpretation of the data. This leads to a significant bias in the least square procedure and thus to errors in the refined parameters.⁴² Especially the positions of the hydrogen atoms are severely affected from bonding densities, because its whole electronic cloud is shifted towards the bonded atom, ending up in a position much too close to this atom. The sum of the spherical densities of the isolated atoms, often referred to as promolecule density $\rho_{\text{pro}}(\mathbf{r})$, in the IAM is defined:

$$\rho_{\text{pro}}(\mathbf{r}) = \sum_q \rho_q^{\text{at}}(r'), \quad (2.7)$$

This leads to the spherical scattering factor

$$f_q(\mathbf{H}) = \int_{V_q} \rho_q^{\text{at}}(r') \exp(2\pi i \mathbf{H} \mathbf{r}') dV_q, \quad (2.8)$$

The parameters of the IAM are:

- 3 fractional coordinates x, y, z
- plus
- 6 anisotropic displacement parameters U_{ij} for non-hydrogen atoms or
 - 1 isotropic displacement parameter U_{iso} for the hydrogen atoms.

The bias implemented in the IAM is reduced if only high-order reflections (e. g. $\sin\theta/\lambda \geq 0.85 \text{ \AA}^{-1}$) are included in the refinement because these reflections almost exclusively represent the sharp core density; the contribution of the much more diffuse valence or bonding density is neglectable. Hence, using a refinement emphasizing high order results in a promolecule density is less biased from the IAM inadequacies and therefore leads to structural parameters comparable to those derived from other methods, e. g. neutron diffraction data (with the exception of the position for hydrogen atoms).^{43,44} Nevertheless, the isolated (=independent) atom model ignores the effect of chemical bonding on the electron density.

2.3 Multipole Model

As atoms in a molecule or a crystal are in a non-spherical environment, an accurate description of the atomic electron density requires non-spherical density functions. Hence, the accuracy of the structural parameters can significantly be increased by implementing an aspherical density model that accounts for the deformation of the ED in order to describe the atomic densities. A commonly applied model is the nucleus-

centered finite multipole expansion, first developed by Stewart⁴⁵ and modified by Hansen and Coppens.⁵ This model, implemented in the XD program package,⁴⁶ was used for the refinements of all compounds in this thesis.

In this multipole formalism the atomic ED $\rho(\mathbf{r})$ is divided into *three components* :

$$\rho_q^{\text{at}}(\mathbf{r}) = \rho_c(r) + P_v \rho_v(\kappa r) + \rho_d(\kappa' \mathbf{r}), \quad (2.9)$$

where $\rho_c(\mathbf{r})$ and $\rho_v(\mathbf{r})$ denote the *spherical core* and *spherical valence* densities, respectively. The term accounting for the *deformation density* $\rho_d(\mathbf{r})$ is:

$$\rho_d(\kappa' \mathbf{r}) = \sum_l R_l(\kappa' r) \sum_{m=-l}^l P_{lm} Y_{lm}(\mathbf{r}/r). \quad (2.10)$$

The spherical and aspherical valence density are modified by the radial scaling parameters κ and κ' , respectively, to account for the radial expansion or contraction of the valence shell. The Y_{lm} are the density-normalized real spherical harmonics while R_l are simple Slater type radial functions with energy optimized exponents α_l .⁴⁷

$$R_l(r) = \frac{\alpha_l^{n(l)+3}}{(n(l)+2)!} r^{n(l)} \exp(-\alpha_l r), \quad (2.11)$$

The core and spherical valence densities are calculated from Hartree-Fock (HF)⁴⁸ or relativistic HF atomic wave functions⁴⁹ given in the International Tables of Crystallography.⁴¹ The corresponding scattering factor following the multipole expansion is:

$$f_q(\mathbf{H}) = f_c(H) + P_v f_v(H/\kappa) + \sum_l \langle J(H/\kappa')_l \rangle \sum_{m=-l}^l P_{lm} Y_{lm}(\mathbf{H}/H), \quad (2.12)$$

where f_c and f_v are the Fourier transforms of ρ_c and ρ_v , respectively, and $\langle J_l \rangle$ the 1th order Fourier-Bessel transform of R_l .

The multipole model offers much more parameters to describe atomic densities than the IAM. In addition to 3 positional and 6 harmonic vibrational parameters this model allows the refinement of a maximum of 25 population parameters together with the mentioned contraction/expansion parameters κ (spherical valence density) and κ' (aspherical deformation density) to account for the populations of the spherical valence density (P_v) and those of the aspherical valence density (P_{lm}) for each non-hydrogen atom. This maximum of 36 parameters per atom leads to a much more flexible model for the description of the atomic densities including density deformations due to chemical bonding and lone-pairs. Thus, the multipole model is a powerful tool to elucidate the charge density distribution in molecular crystals subsequent to a high-resolution X-ray diffraction experiment at ultra-low temperature.

2.4 Functions and Moments derived from the Charge Density Distribution

Once a charge density distribution has been obtained experimentally, various chemical and physical properties can be derived. The calculations of these properties in this thesis were performed with XDPROP, implemented in the XD program package.⁴⁶ Several of these properties are used for the analysis of the refined compounds. They are presented in the following chapters.

2.4.1 Deformation Density

Since the total density is (in almost all cases) dominated by the core electrons and only slightly affected by chemical bonding, difference densities maintaining from the deviation of a reference density are often used to illustrate bonding features. A commonly used function is the deformation density $\Delta\rho(\mathbf{r})$, defined as the difference between the total density $\rho(\mathbf{r})$ and the density corresponding to the sum of the spherical atoms. A widely used reference state is the spherical atomic density of the IAM defined in equation (2.7). Typically, the static deformation density is used in recent publications:

$$\Delta\rho_{\text{static}}(\mathbf{r}) = \rho(\mathbf{r}) - \sum_q \rho_q^{\text{at}}(\mathbf{r}), \quad (2.13)$$

For this $\Delta\rho_{\text{static}}(\mathbf{r})$ the spherical averaged density from independent atoms, is subtracted from the thermally averaged total density modeled from the multipole formalism. Therefore, the static deformation density is, in contrast to Fourier densities, not limited to a finite resolution of the experimental data set. The deformation density shows the accumulation of density in the bonding and lone-pair regions of a molecule. However, for elements with more than half filled valence shells, bonding peaks in the deformation densities may be absent due to the neutral, spherically averaged reference atom which contains more than one electron in each orbital of the valence shell.^{50,51} Nevertheless, deformation density maps are widely used and an important tool in the analysis of bonds.

2.4.2 Electrostatic Potential

Another density related property of chemical interest is the electrostatic potential (ESP). The ESP at a given point in space, defined as the energy required to bring a positive unit of charge from infinite distance to this point, is suitable for the study of chemical reactivity. For an atom, composed from a positive charge at a certain point, the nucleus, and a continuous distribution of negative electronic charge around this point, we obtain:

$$\Phi(\mathbf{r}) = \sum_q \frac{Z_q}{|\mathbf{R}_q - \mathbf{r}'|} - \int \frac{\rho(\mathbf{r})}{|\mathbf{r} - \mathbf{r}'|} d\mathbf{r}, \quad (2.14)$$

where Z is the charge of the nucleus q located at \mathbf{R} . The first term of the equation describes the nuclei contributions, from which the second part, the electron distribution term, is subtracted.

As electrostatic forces are relatively long-range forces, they determine the path a reactant uses to reach the reactive parts of a molecule. Hence, in chemical terms nucleophilic reagents are attracted to regions with positive potential while electrophiles approach the negative.

For the calculation of the ESP from X-ray diffraction data the formalism introduced from Su and Coppens⁵² was applied in this thesis. It evaluates the ESP from the experimental electron density as described by the multipole formalism for a molecule isolated from the crystal environment.

2.4.3 Dipole Moment

The dipole moment μ is directly accessible from the multipole populations after an aspherical atom refinement. It is of considerable importance since it occurs in the expressions for intermolecular interactions and lattice energies. The dipole moment vector results from the molecular charge distribution, and both, its magnitude and its direction can be extracted from accurate X-ray diffraction data.^{53,54}

A charge q at a certain point with the distance d to another point with an opposite sign results in an electric dipole with the dipole moment μ :

$$\mu = q \cdot d, \quad (2.15)$$

A given molecule reveals a dipole moment if the centre of all positive charges located at the nuclei is not identical with the centre of the negative charge:

$$\mu_{i,j,k} = \int_V \rho(\mathbf{r}) x^i y^j z^k d\mathbf{r} \quad (2.16)$$

with the unit vectors \mathbf{i} , \mathbf{j} , \mathbf{k} in the Cartesian frame. The direction of the dipole vector is oriented from the positive to the negative charge. Dipole moments derived from X-ray data are generally larger than those calculated for isolated molecules because the first contain contributions from polarization and the effect of the packing arrangement.

2.5 Theory of “Atoms in Molecules” (AIM)

Much more information about the electronic situation in molecules, independent from the use of any reference state, can be extracted if the modeled electron density from the X-ray diffraction experiment is analyzed in terms of Bader’s quantum theory of ‘atoms in molecules’ (AIM).⁹

The topological analysis of the total density, developed by Bader and coworkers, leads to a scheme of natural partitioning of a molecule into atomic basins. Within this theory, an atom in a molecule is a region in real space, containing one nucleus, bound to other atoms by surfaces (called ‘zero flux surfaces’, defined by $\nabla\rho = 0$). The atoms can exchange charge and momentum across this interaction surface. The AIM theory leads inevitably to a completely new idea of atoms in the field of chemistry because atoms of the same element are no longer identical, only their cores are.

2.5.1 Critical Points

The charge density, $\rho(\mathbf{r})$, is a physical quantity which has a definite value at each point in space. It is a scalar field defined over three dimensional space. The topological properties of such a scalar field are summarized in terms of the number and type of its critical points (CPs). A critical point denotes an extremum in $\rho(\mathbf{r})$, a point where the first derivative, $\nabla\rho(\mathbf{r})$, vanishes:

$$\nabla\rho(\mathbf{r}) = \mathbf{i}\frac{\partial\rho}{\partial x} + \mathbf{j}\frac{\partial\rho}{\partial y} + \mathbf{k}\frac{\partial\rho}{\partial z} = 0 \quad (2.17)$$

where \mathbf{i} , \mathbf{j} , \mathbf{k} are the unit vectors in the Cartesian frame. The CPs denote maxima, minima and saddle points in the the charge density. A CP is characterized by the rank (ω) of the Hessian matrix $\mathbf{H}(\mathbf{r})$, defined as the symmetric matrix of the nine second derivatives of $\rho(\mathbf{r})$ and by the algebraic sum of the signs (σ) of the principal curvatures of $\rho(\mathbf{r}_{\text{CP}})$:

$$\mathbf{H}(\mathbf{r}) = \begin{pmatrix} \frac{\partial^2\rho}{\partial x^2} & \frac{\partial^2\rho}{\partial x\partial y} & \frac{\partial^2\rho}{\partial x\partial z} \\ \frac{\partial^2\rho}{\partial y\partial x} & \frac{\partial^2\rho}{\partial y^2} & \frac{\partial^2\rho}{\partial y\partial z} \\ \frac{\partial^2\rho}{\partial z\partial x} & \frac{\partial^2\rho}{\partial z\partial y} & \frac{\partial^2\rho}{\partial z^2} \end{pmatrix}_{\mathbf{r}=\mathbf{r}_{\text{CP}}} \quad (2.18)$$

The eigenvectors (λ_i) of $\mathbf{H}(\mathbf{r})$, obtained by diagonalization of this matrix, are the three principal curvatures at \mathbf{r} :

$$\mathbf{D}(\mathbf{r}) = \begin{pmatrix} \frac{\partial^2 \rho}{\partial x^2} & 0 & 0 \\ 0 & \frac{\partial^2 \rho}{\partial y^2} & 0 \\ 0 & 0 & \frac{\partial^2 \rho}{\partial z^2} \end{pmatrix}_{\mathbf{r}=\mathbf{r}_{\text{CP}}} = \begin{pmatrix} \lambda_1 & 0 & 0 \\ 0 & \lambda_2 & 0 \\ 0 & 0 & \lambda_3 \end{pmatrix} \quad (2.19)$$

with the eigenvalues λ_1, λ_2 and λ_3 of the Hessian matrix, where $\lambda_1 \leq \lambda_2$.

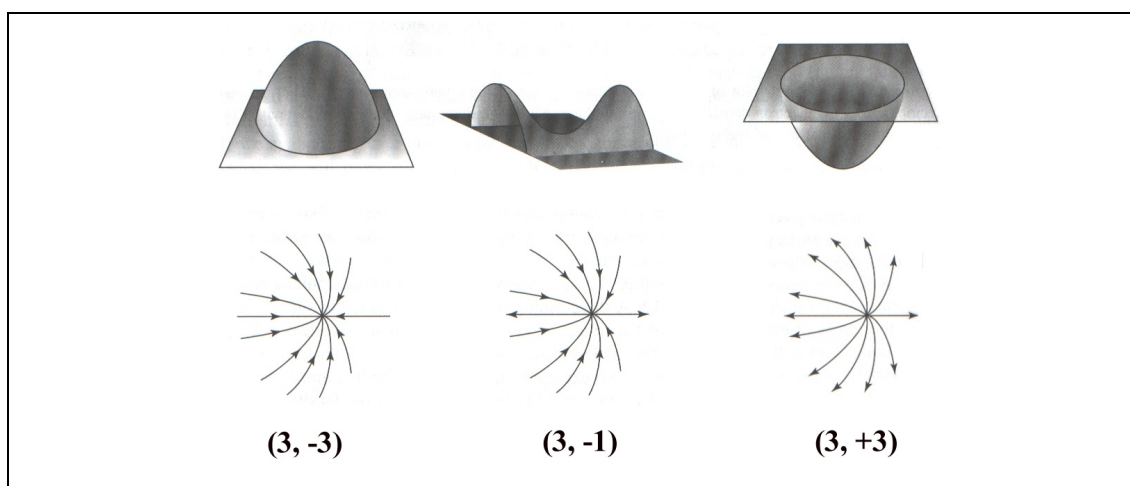


Figure 2.1 Classification of critical points (CPs): (3, -3)CP: local maximum (atom position); (3, -1)CP: saddle point/bond critical point; (3, +3)CP: local minimum.⁵⁵

There are just four possibilities for signature values for CPs of rank three:

- (3, - 3) All curvatures are negative and ρ is a local maximum at \mathbf{r}_{CP} . This type is found at the atom positions.
- (3, - 1) Two curvatures are negative and ρ is a maximum at \mathbf{r}_{CP} in the plane defined by their corresponding axes. ρ is a minimum at \mathbf{r}_{CP} along the third axes being perpendicular to the plane made up of the first two curvatures. (3, -1) CPs in ρ (saddle points) are the characteristic criterion for the formation of a chemical bond; therefore this type of CP is termed bond critical point (BCP).
- (3, + 1) Two curvatures are positive and ρ is a minimum at \mathbf{r}_{CP} in the plane defined by their corresponding axes. ρ is a maximum at \mathbf{r}_{CP} along the third axes being perpendicular to the plane made up of the first to curvatures. This type of CP is found inside a ring of at least three

bonded atoms, also called ring critical point (RCP)

(3, + 3) All curvatures are positive and ρ is a local minimum at \mathbf{r}_{CP} .

2.5.2 The Laplacian

While the topology of the electron density ρ provides a faithful mapping of the concepts of atoms, bonds and structure, it provides no indication of maxima in $\rho(\mathbf{r})$ corresponding to electron pairs of the Lewis model.⁵⁶ However, the details of the density distribution becomes rapidly apparent when the Laplacian, defined as the scalar derivative of the gradient vector field of the electron density (equation (2.17)), is examined (Figure 2.2). In mathematics:

$$\nabla^2 \rho(\mathbf{r}) = \nabla \cdot \nabla \rho(\mathbf{r}) = \frac{\partial^2 \rho}{\partial x^2} + \frac{\partial^2 \rho}{\partial y^2} + \frac{\partial^2 \rho}{\partial z^2}. \quad (2.20)$$

The quantity $\nabla^2 \rho(\mathbf{r})$ determines whether electronic charge is locally concentrated, $\nabla^2 \rho(\mathbf{r}) < 0$, or depleted, $\nabla^2 \rho(\mathbf{r}) > 0$. The local charge concentrations provide a mapping of the electron pairs of the Lewis and VSEPR model.⁵⁷

The Laplacian is a very sensitive tool to display the shell structure of an atom and to analyze small changes in the spatial distribution of the electron density in the valence shell of an atom.

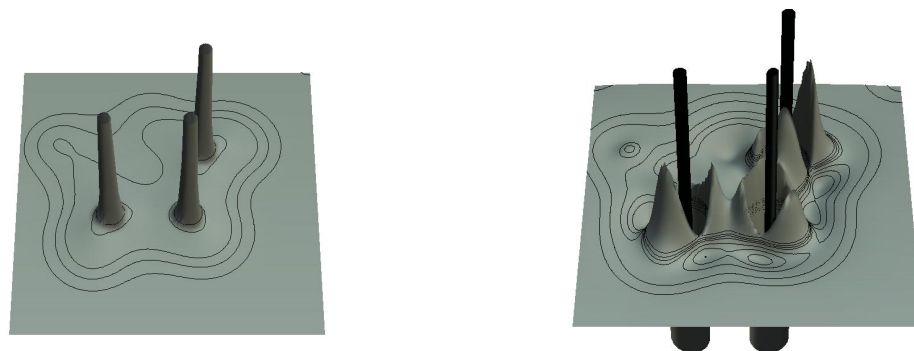


Figure 2.2 Electron density $\rho(\mathbf{r})$ (left) and Laplacian $\nabla^2 \rho(\mathbf{r})$ (right) in a plane of three carbon atoms.

2.5.3 Electronic Energy Density

The Laplacian of $\rho(\mathbf{r})$ and thus local concentrations and depletions of the electrons in the internuclear space are connected with the features of the electronic energy distribution *via* the local form of the virial theorem:⁵⁸

$$-L(\mathbf{r}) \equiv \left(\frac{\hbar^2}{4m} \right) \nabla^2 \rho(\mathbf{r}) = 2G(\mathbf{r}) + V(\mathbf{r}). \quad (2.21)$$

The latter expression gives an exact explicit relationship between the second derivative of the electron density $\nabla^2 \rho(\mathbf{r})$, the electronic kinetic energy density $G(\mathbf{r})$ (calculated using the Kirzhnits approximation⁵⁹) and the electronic potential energy density $V(\mathbf{r})$. The electronic energy density,⁵⁸

$$H_l(r) = G(r) + V(r), \quad (2.22)$$

is more straight criterion for the recognition of the atomic interaction type: $H_l(\mathbf{r}) < 0$ at the BCP is observed in shared-type (covalent) atomic bonding, while $H_l(\mathbf{r}) \geq 0$ is observed in purely closed-shell (ionic) interactions.⁶⁰

2.5.4 Integration over Topological Basins

Bader's AIM theory provides a well defined procedure of partitioning a molecule into atomic regions: according to Bader, an atom, free or bound, is the union of an attractor of the corresponding trajectories of the electron density gradient vector field and its associated basin with zero flux surfaces (ZFS) as boundaries. The attractors are maxima in $\rho(\mathbf{r})$ ((3, - 3) CPs) or in other words the nuclei of the atoms (2.5.1). The boundaries of the basins are never crossed by a gradient vector. Since the surface is not crossed by any gradient line, it is referred to as surface of zero flux. The total boundary surface of the basin Ω is defined by:

$$\nabla \rho(\mathbf{r}) \cdot \mathbf{n}(\mathbf{r}) = 0 \quad (2.23)$$

with the vector normal of the surface $\mathbf{n}(\mathbf{r})$. As a result, each basin uniquely defines an atomic volume which can be integrated over all elements τ of this volume:

$$V(\Omega) = \int_{\Omega} d\tau \quad (2.24)$$

A result of the integration, performed with TOPXD⁶¹ is the atomic charge. The atomic charge is, according to Bader, the difference between the charge of the positive atomic core and the electronic populations of this atom.

In contrast to theoretical ab initio or DFT calculations of isolated molecules, an atom in a crystal is surrounded by neighbours in all directions of space. Therefore, the shape of an atom, directly related with the charge density distribution around this atom, often differs extremely from a sphere. Because of this complex shape of the ZFS the integration over the atomic basin is very demanding and computer-time consuming.

The electroneutrality of a molecule serves as test for the accuracy of the integration - the sum of all integrated atomic charges of a neutral molecule is zero. However, due to the time consuming procedure this test was not available for the compounds under study in this thesis. Despite, the quality of the integrations are tested with the Lagrangian L. For a proper integration, with a small error in the determination of the total energy of a quantum atom, it should vanish. The Lagrangian should not be significantly above $5 \cdot 10^{-4}$ kJ/mol for second row atoms and not exceed values of $5 \cdot 10^{-3}$ kJ/mol for atoms with higher energy, e.g. third row atoms.⁶²

2.5.5 Classification of Bonds

Several criteria are discussed in this thesis to characterize and classify bonds. Recent publications proved^{11,35} that the criteria from Coppens⁶ quoted just a few years ago are no longer sufficient for a classification as covalent or ionic. For this reason some additional properties are listed to enable a classification based on various arguments.⁶³

The listed properties were calculated with the programs XDPROP⁴⁶, TOPXD⁶¹ and WinXPRO.⁶⁴

a) Bond critical point (BCP)

The definition and classification of a chemical bond in the topological analysis is based on (i) the existence of a BCP in the total electron density between two neighbouring atoms, and (ii) on a bond path which follows the maximum electron density and terminates at the neighbouring atom. The presence of a bond path is a necessary and sufficient condition for bonding in the AIM theory. These requirements are far beyond the comparison and interpretation of geometrical features from a routine structure determinations to establish a bond.⁶⁵

b) Amount of electron density $\rho(\mathbf{r})$

The charge density in the bonding region increases with the number of assumed electron pair bonds. Values for polar covalent bonds cluster around unity for $\rho(\mathbf{r}_{\text{BCP}})$; for ionic bonds the value at the BCP should be significantly below unity.

The dimension of ρ is $\text{e}\text{\AA}^{-3}$.

c) Laplacian of ρ , $\nabla^2\rho(\mathbf{r})$

The Laplacian, the algebraic sum of the three principal curvatures λ_1 , λ_2 and λ_3 of $\rho(\mathbf{r})$, is the most important tool to localize and characterize regions of charge concentration and depletion. The nature of the atomic interaction depends on the

dominant curvatures. Shared interactions (covalent bonds) are dominated by the negative curvatures (λ_1, λ_2); charge is concentrated in the internuclear region. This charge concentration is reflected in a relatively large value of $\rho(\mathbf{r}_{\text{BCP}})$ and in a large negative value of the Laplacian $\nabla^2\rho(\mathbf{r}_{\text{BCP}})$. For closed-shell interactions (ionic bonds), the positive curvature λ_3 is dominant; charge is depleted in the entire interatomic region as a result of the contraction of $\rho(\mathbf{r}_{\text{BCP}})$ towards each nucleus and the spatial distribution of the Laplacian is mostly atomic-like. This charge depletion is characterized by a relatively low value of $\rho(\mathbf{r}_{\text{BCP}})$ and by a low positive value of $\nabla^2\rho(\mathbf{r}_{\text{BCP}})$.⁸ As the position of the BCP is vital and the values differ dramatically with slight variations of the position, the Laplacian is monitored along the whole bond path for the studied highly polar bonds in this thesis.⁶⁶ Nevertheless, the value of the Laplacian of ρ at the BCP remains important for comparison with other samples⁸ and thus is tabulated for all bonds of interest.

Moreover, the inspection of the valence shell for (3, - 3) critical points in the spatial distribution of $-\nabla^2\rho(\mathbf{r})$ facilitates the localization and quantification of maxima of the charge concentration in the bonding and non-bonding regions in the valence shell of an atom; these areas are so called valence shell charge concentrations (VSCCs). This procedure furnishes information about the Laplacian distribution apart from the bonding regions. In addition the number of VSCCs around an atom allows to deduce the hybridization state of this atom.^{11,67}

The unit of the Laplacian is $\text{e}\text{\AA}^{-5}$.

d) Ratio of $|\lambda_1|/\lambda_3$

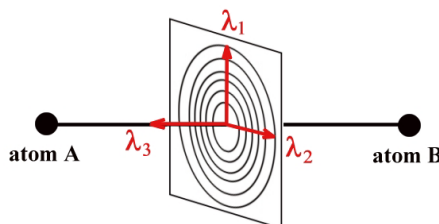
The ratio of the largest contraction perpendicular to the bond, λ_1 , and the concentration parallel to the bond, λ_3 , is much below 1 for closed-shell interactions. For shared interaction, the value increases with respect to bond strength and ionicity of a bond.

The ratio of $|\lambda_1|/\lambda_3$ is dimensionless.

e) Ellipticity, $\varepsilon = (|\lambda_1|/|\lambda_2|) - 1$

The ratio of the two contractions perpendicular to the bond, λ_1 and λ_2 , is a sensitive tool to measure the bonding order. For cylindrical non-polar homonuclear C–C- and C≡C-bonds the ellipticity is close to zero while ε is higher than zero for elliptical C=C-double bonds. As for the Laplacian, it is necessary to monitor the ellipticity of polar bonds along the whole bond path. Bader et al. showed, that

values for this property change permanently along the whole path in heteronuclear bonds.⁶⁸ At the BCP, pure σ -bonds should adopt an ellipticity below 0.1 (cylindrical symmetry) along the bond path. π -bonds show an almost symmetric ‘bell-shape’ with $\varepsilon > 0.2$ in the entire bonding region, while contribution of lone-pairs to bonding density results in ε values above 0.15 and an asymmetric distribution of ε with a distinct maximum in the basin of the atom with the lone-pair. Spatial orientation of the eigenvalues λ_i :



As a ratio of similar entities the ellipticity is dimensionless.

f) Charges from integrated basins

Reliable atomic charges can be derived from the integration of the electron density over the atomic basin. As already mentioned, these basins are the result of a partitioning of a molecule into atomic regions with boundaries according to Bader's AIM theory (2.5.4). Charges following Bader's partitioning scheme are higher than those obtained with other methods^{69,70} because polarization effects are more operative in a crystal. However, Bader-charges are very helpful to get an impression of the bonding situation, especially in polar bonds, and they are rather invariant with regard to changes in the multipole model used in the refinement.

The charges are given in electrons (e).

g) Electronic energy density at the BCP

The electronic energy density H_1 of covalent bonds is negative, while purely ionic bonds have values of $H_1 \geq 0$. Typical values for covalent bonds are -0.2 - -0.5 .⁶⁰ H_1 is given in atomic units (au).

3 Experimental Section

The charge density distribution and topological analysis of all compounds in this thesis is based on data from X-ray diffraction experiments (graphite-monochromated $\text{Mo}_{\text{K}\alpha}$ radiation, $\lambda = 0.71073 \text{ \AA}$). The requirements on the accuracy of the diffraction experiments for a subsequent multipole refinement are extremely high. Compared to a standard diffraction experiment up to a diffraction angle of $\sin\theta/\lambda = 0.625 \text{ \AA}^{-1}$ ($2\theta_{\text{max}} = 50^\circ$, $\text{Mo}_{\text{K}\alpha}$), reflections up to at least $\sin\theta/\lambda = 1.08 \text{ \AA}^{-1}$ ($2\theta_{\text{max}} = 100^\circ$, $\text{Mo}_{\text{K}\alpha}$) have to be collected. The reflections at high diffraction angles are necessary to get reliable atomic positions (chapter 2.2). Furthermore, the high-angle reflections are needed for a satisfying data-to-parameter ratio (minimum: 15:1) due to the increasing number of parameters in a multipole refinement. To get the best estimate of the scattering factors, high redundancies of the low-angle reflections, from which the more diffuse parts of the electron density distribution are extracted, have to be collected. The quality of the reflections has to be superior, that means sharp reflections with half-widths better than 0.5 of a degree and sufficient intensities ($I \geq 2\sigma(I)$) even at high diffraction angles. Due to the high redundancies and a stepwidth of only 0.2° per frame at the low Bragg angles and long exposure times as well as a stepwidth of 0.3° per frame for the high-order reflections the strategy for the data collection has to be optimized to cover the whole reciprocal space within a minimum of time.

All these conditions are oblique for an X-ray diffraction experiment with subsequent multipole refinements, but they do not guarantee a successful refinement – many other details have to be taken into consideration to succeed in an appropriate determination of the charge density distribution.

3.1 Data Collection

During the application process the oil-coated crystals were mounted on a glass fibre glued in the goniometer head of the X-ray diffractometer. All data sets for the compounds studied in this thesis were collected on a Bruker Apex-CCD diffractometer with a D8 three-circle goniometer, equipped with an open circle liquid nitrogen cooling device.³ To minimize thermal motion, the aim was to measure all compounds at a temperature of 100(2)K. However, for some of the studied compounds phase transition was observed as they cracked during the cooling process from room temperature down

to the experimental temperature. Therefore, the cooling process was monitored *via* a video camera to find the lowest possible temperature before the phase transition occurred (Table 3.1).

The strategy for the data collection of all compounds was identical. The data were collected exclusively in omega-scan mode with only two detector positions and a sample detector distance of 5cm. The data collection was monitored with SMART.⁷¹ Data collected at the first detector position is called “low-angle batch”, while those at the second position (including the reflections of the high diffraction angles) is termed “high-angle batch”, respectively. This strategy leads to a completeness of almost 100% up to $\sin\theta/\lambda_{\max} = 1.14\text{\AA}^{-1}$ even for systems with low symmetry. The applied strategy bears a limitation in the overlap regions for both detector positions. This can lead to scaling problems for the two batches. For this reason all reflections of the high-angle batch, detected in the overlap region ($(\sin\theta/\lambda)_{\max} < 0.625\text{\AA}^{-1}$), were removed and the two batches treated independently during all following steps of data processing. In addition, for all subsequent refinements an individual scaling factor was assigned for the two batches, no.1 for the low-angle batch and no.2 for the high-angle batch, respectively. Details of the data collection are presented in Table 3.1.

Table 3.1 Details of the data collection of compounds I–VIII.

compound	I	II	III	IV
identification code	mpi1	mpi2	OMCTS	dianion
crystal size [mm]	0.40x0.20x0.05	0.40x0.40x0.05	0.35x0.25x0.20	0.60x0.50x0.30
temperature [K]	100	100	100	173
detector positions (2 θ) [°] (low-angle, high-angle)	32, 75	32, 75	31, 80	31, 80
ϕ -positions (low-angle) [°]	0, 45, 90, 135, 180, 225, 270, 315	0, 90, 180 (2 times each), 45, 135, 225, 270, 315	0, 90, 180, 270 (2 times each), 45, 135, 225, 315,	0, 45, 90, 135, 180, 225 (2 times each), 270, 315
no. frames per run / $\Delta\omega$ [°] / exposure time [s]	895 / -0.2 / 10	895 / -0.2 / 10	901 / -0.2 / 6	906 / -0.2 / 10
ϕ -positions (high-angle) [°]	0, 45, 90, 180, 225, 270	0, 45, 90, 135, 180, 225, 270, 315	0, 45, 90, 135, 180, 225, 270	0, 45, 90, 135, 180, 225, 270, 315
no. frames per run / $\Delta\omega$ [°] / exposure time [s]	895 / -0.2 / 90	901 / -0.2 / 60	901 / -0.2 / 80	606 / -0.3 / 150
$\sin\Theta / \lambda_{\max}$ [\AA^{-1}]	1.069	1.041	1.141	1.143
reflections collected (low-angle batch)	20609	29212	54595	54632
reflections collected (high-angle batch)	25467	45273	74651	80137

compound	V	VI	VII	VIII
identification code	tetra	kost17	feuer	spaten
crystal size [mm]	0.45x0.40x0.15	0.65x0.55x0.50	0.60x0.57x0.55	0.50x0.40x0.30
temperature [K]	130	100	100	100
detector positions (2 θ) [°] (low-angle, high-angle)	31, 80	31, 80	31, 80	31, 75
ϕ -positions (low-angle) [°]	0, 90, 180, 270 (2 times each), 45, 135, 225, 315,	0, 45, 90, 135, 180, 225, 270, 315 (2 times each)	0, 45, 90, 135, 180, 225, 270, 315 (2 times each)	0, 45, 90, 135, 180, 225, 270, 315 (2 times each)
no. frames per run / $\Delta\omega$ [°] / exposure time [s]	901 / -0.2 / 20	901 / -0.2 / 10	901 / -0.2 / 4	906 / -0.2 / 20
ϕ -positions (high-angle) [°]	0, 45, 90, 135, 180	0, 90, 135, 180, 225, 270	0, 45, 90, 135, 180, 225, 270, 315	0, 45, 90, 135, 180
no. frames per run / $\Delta\omega$ [°] / exposure time [s]	604 / -0.3 / 300	606 / -0.3 / 90	604 / -0.3 / 90	606 / -0.3 / 300
$\sin\Theta / \lambda_{\max}$ [Å ⁻¹]	1.079	1.142	1.145	1.106
reflections collected (low-angle batch)	88122	24118	51465	43137
reflections collected (high-angle batch)	96212	29791	74909	27890

3.2 Data Processing

The data processing was almost identical for all data sets; differing procedures were exclusively used during absorption correction. The low- and high-angle batches were treated separately at each step of the data processing.

Matrix Determination and Integration

The reflections were integrated using the program SAINT.⁷² The orientation matrices needed for this procedure were determined with SMART,⁷¹ individually for each run. The matrix of each run is based on reflections with an I/σ threshold of 20 from 100 frames.

The integration was performed in two steps. At first the data were integrated with individual matrices for each run using the matrix and integration box refinement mode of SAINT. This leads to the best estimate of an averaged matrix and integration box for all runs in a batch. With those averaged matrices and integration boxes the second, final integration, was performed using the fixed matrix and integration box mode of SAINT.

To facilitate the integration with the exact α and γ angles, slightly deviating from 90° after the first step of the integration even for higher symmetry than triclinic, all data were integrated with unconstrained symmetry. In several compounds inspection of the integrated high-order data revealed a remarkable decrease of the quality of the very weak intensities at diffraction angles higher than $2\theta = 100^\circ$. In these cases a high resolution limit was applied during the refinement (details are given in the refinements of the affected compounds).

Absorption correction

Although the absorption of all measured compounds was rather low, an empirical correction was applied for the raw data of all compounds using SADABS⁷³ for compound **I** and **II** and SORTAV, implemented in WinGX,⁷⁴ for compound **III-VIII**. Both programs use the excellent algorithm developed by Blessing.⁷⁵

Merging and Batch Number Assignment

The space groups of all compounds were determined with XPREP;⁷⁶ the same program was used for merging the data. Afterwards individual batch numbers were assigned with the program BATCH⁷⁷ for the high- and low-angle batch of each data set.

In a final step the two batches for each data set were combined to one hkl-file.

3.3 Refinements

Before refinement all structures were solved with the program SHELXS⁷⁸, using direct methods. The starting input file for a multipole refinement already contains the parameters of a readily refined IAM structure. Therefore, a structure refinement with the IAM model was performed prior to the multipole refinement.

3.3.1 IAM Refinement

All IAM refinements were carried out with SHELXL.⁷⁹ In contrast to the strategy used for standard structure refinement with this model, the coordinates and anisotropic displacement parameters of the non-hydrogen atoms were solely refined with reflections from high scattering angles $\sin\theta/\lambda \geq 0.80\text{\AA}^{-1}$. The bias introduced from bonding densities is very small beyond this limit.⁸⁰ The hydrogen atoms were treated with special care. H atoms of interesting functional groups were located by Fourier synthesis with reflections $\sin\theta/\lambda \leq 0.50\text{\AA}^{-1}$. All other hydrogen atoms bonded to carbon atoms were assigned geometrical ideal positions. Refinement of the hydrogen atom positions was achieved with the same conditions; the thermal parameters were refined using a

riding model with U_{iso} constrained to the U_{eq} value of the parent bonded atom. After convergence was reached the hydrogen atom positions were shifted along the bonding vector to idealized distances, only available from neutron diffraction data.⁸¹

In all refinements the quantity $\sum_H w_H (|F_{\text{obs}}(\mathbf{H})| - k|F_{\text{calc}}(\mathbf{H})|)^2$ was minimized using the statistical weight $w_H = \frac{1}{\sigma^2}(F_{\text{obs}}(\mathbf{H}))$.

3.3.2 Multipole Refinement

A multipole model was adopted to describe the deformation of $\rho(\mathbf{r})$. The complexity of the IAM model, in which all atoms were treated spherically, was increased in a stepwise manner using the multipole formalism of Hansen and Coppens⁵ implemented in the XD package.⁴⁶ The following conditions were common to the refinements of all compounds. Further details are reported in the discussion of each compound.

The multipole refinements were again carried out on F^2 using statistical weights and only those intensities which met the criterion of $I > 2\sigma(I)$. Default radial functions were chosen for the core and the spherical valence densities. The n_l values of the Slater type radial functions were adjusted to recommended values $n_l = 4, 4, 6, 8$ ($l = 1, 2, 3, 4$) for third row atom atoms.⁵ Recent studies proved that the density functions of third row atoms are fitted better with these n_l values while for all other atoms the conventional sets of n_l remain sufficient.^{82,83}

The multipole refinements started with the adjustment of the scaling factors, this was followed by a refinement of the monopoles P_v together with κ . In the next step the multipoles P_{lm} of the non-hydrogen atoms were refined. The maximum of the multipole expansion in XD is the hexadecapole level ($l = 4$), used only for a few atoms in each refinement. For most of the non-hydrogen atoms multipoles up to the octapole level were adequate to describe the electron density (the maximum assigned to hydrogen atoms was the quadrupole level; for most of the H atoms solely a bond-directed dipole was included in the refinement). Atomic coordinates and anisotropic displacement parameters were processed followed by an adjustment of the hydrogen atoms. Hydrogen atoms were treated with special care. Coordinates and thermal parameters of the H atoms were kept fixed on the values of the starting model until coordinates and U_{ij} of the non-hydrogen atoms were included in the refinement procedure. For all following steps the hydrogen parameters were adjusted after each step of the refinement using reflections with $\sin\theta/\lambda < 0.5\text{\AA}^{-1}$, keeping the C–H distances fixed and restraining the $U_{\text{iso}}(\text{H})$ -values. P_v and P_{lm} of all atoms were then refined together with positional and thermal parameters of the non-hydrogen atoms as well as the scaling factors.

Subsequently, κ' was included in the refinement. The κ' values for the four sets of multipoles were constrained to be equal. To derive meaningful parameters for the contraction of the hydrogen atoms, κ and κ' values for this element suggested by Volkov et. al.⁸⁴ were introduced and kept fixed during the refinement of all compounds. All κ' parameters of the other atoms were refined individually, because the expansion/contraction factor of the deformation densities is the most sensitive parameter of the refinement. In a final step, all mentioned parameters but κ' , x, y, z and U_{iso} of the hydrogen atoms were refined together. Each step was refined to convergence and the scaling factors were adjusted in any step of the refinement but those including hydrogen atoms. The electroneutrality constraint was employed in the refinement of each sample.

To decrease the number of parameters non-crystallographic symmetry was used to constrain chemically equivalent atoms (e. g. in a phenyl ring). It is to be pointed out, that these similarity constraints only refer to the multipoles of the constrained atoms. Changes in thermal motions and atomic positions were refined individually. Furthermore, application of local symmetry to the multipole populations was used to decrease the number of multipoles (e. g. a mirror plane for the carbon atoms in phenyl rings). Therefore, the right choice of the local coordinate system is essential. In addition, a radial scaling factor (κ) for the spherical density was refined for chemically equivalent atoms, together with a scaling factor (κ') of the radial function for the deformation density.

3.3.3 Testing the Results

There are several criteria to test the reliability of the results of structure refinements that guarantee the agreement of the observed and calculated structure factors. Naturally, results of a multipole refinement have to match all these criteria. All important figures of merit to check the quality of a multipole refinement are quoted in the following list.

R-values (Residual value)

The conventional R-values are defined as follows:

$$R1 = \frac{\sum_{\mathbf{H}} (|F_{\text{obs}}| - |F_{\text{calc}}|)}{\sum_{\mathbf{H}} |F_{\text{obs}}|} \quad R2 = \frac{\sum_{\mathbf{H}} (|F_{\text{obs}}|^2 - |F_{\text{calc}}|^2)^2}{\sum_{\mathbf{H}} |F_{\text{obs}}|^4} \quad (3.1)$$

Invokeing a weighting scheme leads to wweighted R-values:

$$wR1 = \frac{\sum_{\mathbf{H}} w_{\mathbf{H}} (|F_{\text{obs}}| - |F_{\text{calc}}|)}{\sum_{\mathbf{H}} w_{\mathbf{H}} |F_{\text{obs}}|} \quad wR2 = \frac{\sum_{\mathbf{H}} w_{\mathbf{H}} (|F_{\text{obs}}|^2 - |F_{\text{calc}}|^2)^2}{\sum_{\mathbf{H}} w_{\mathbf{H}} |F_{\text{obs}}|^4} \quad (3.2)$$

The R-values of a proper multipole refinement should be much smaller than those of the starting conventional IAM model. Due to the description of the bonding densities the agreement between F_{obs} and F_{calc} is assumed to increase. Of course, the improvement is proportional to the ratio of valence density to the total density. In other words, the improvement decreases the more atoms from the third row of the periodic table of elements, or even heavier atoms, are present. Another figure of merit is the

GoF (Goodness of Fit)

$$\text{GoF} = \sqrt{\frac{\sum_{\mathbf{H}} w_{\mathbf{H}} (|F_{\text{obs}}| - |F_{\text{calc}}|)^2}{N - n}}, \quad (3.3)$$

where N is the number of used reflections and n the number of refined parameters, respectively. If the structure is determined properly, and the weighting scheme is correct, the GoF should cluster around unity.

The GoF of the structures presented in this thesis is always approximately 2. This is a very well known feature of multipole refinement and is referred to the weighting scheme, which is not adjusted during the standard refinement procedure⁸⁵ in order to avoid bias.⁸⁶ GoF values around 2 indicate slightly underestimated standard deviations σ for the results from multipole refinement.

The reliability of a multipole refinement is ascertained with additional tools:

DMSDA-test (Difference of the Mean-Square Displacement Amplitude-test)

This is provided by the rigid-bond postulate,⁸⁷ which asserts that the mean-square displacement amplitudes (MSDAs) of every pair of bonded atoms A and B should be nearly equal in the bond direction, especially when the two atoms have a comparable mass:

$$z_{AB}^2 = z_{BA}^2 \quad (3.4)$$

with the radius of the displacement amplitude of atom A and B along the bonding vector **AB** z_{AB}^2 and z_{BA}^2 , respectively. The electron density is deconvoluted properly from

thermal motion if the DMSDA is smaller than 0.001\AA^2 for atoms with equal nuclear masses. This value can be exceeded if the mass difference of the atoms A and B is considerable (e.g. in a Si–C bond). A significant deviation from the values expected from the rigid-bond postulate indicates bias by unresolved or indeterminable valence density asphericities caused by poor data or unrecognized disorder.

In the latest version of the XD program package Koritsanszky implemented a new section that allows to start with ADPs from theoretical calculations, that are not affected from MSDAs, after they are converted from cartesian systems to the crystal frame (not applied to the X-ray data of this thesis).⁸⁸ Moreover, it is possible to fix reliable MSDAs from experimental data during the refinement if they are seriously influenced from correlations. This opens the way for the multipole refinement of experimental data with poor high-angle reflections from which responsible MSDAs are not accessible.

Residual Density

One of the most important tools to check the accuracy of multipole refinements are the residual maps of the electron density. They are expected to be flat and featureless showing only random experimental noise up to a resolution of $\sin\theta/\lambda \leq 1.00\text{\AA}^{-1}$ for classic organic compounds (for samples containing third row atoms the residual map should include reflection up to at least $\sin\theta/\lambda \leq 0.90\text{\AA}^{-1}$). If the electron density exceeds $0.2\text{e}\text{\AA}^{-3}$ at the atomic positions or in the bonding regions the refinement model must be modified. As shown in Figure 3.1 this is a very high aim to reach because the residual densities at the end of a conventional refinement are very high.

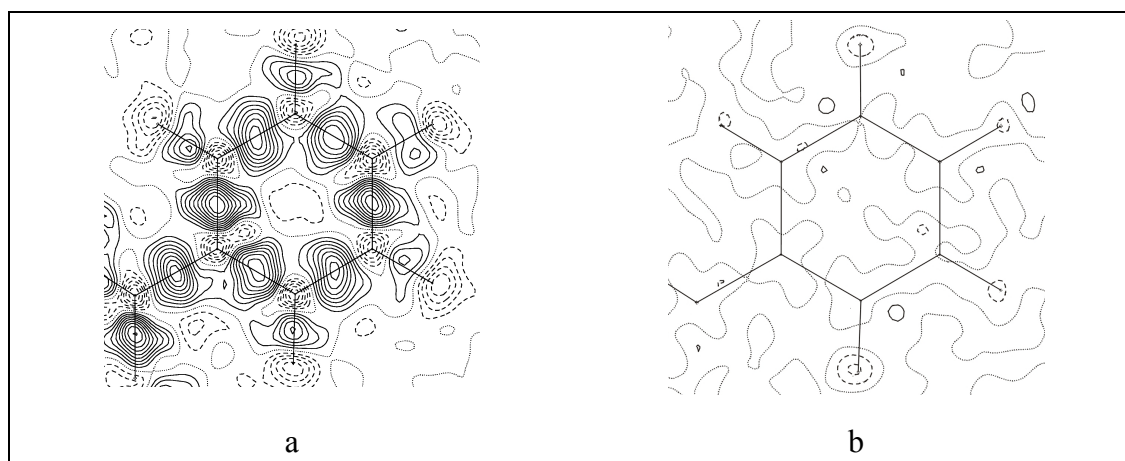


Figure 3.1 Residual map at the end of a conventional refinement (a) and a multipole refinement (b) in the plane of the phenyl ring of **VI** to a resolution of $\sin\theta/\lambda_{\text{max}} = 1.00\text{\AA}^{-1}$; positive countours solid, zero contour dotted, negative contours dashed; stepwidth is $0.1\text{e}\text{\AA}^{-3}$.

4 Methodical Development – Multipole Refinement of a Twinned Sample

Currently, multipole refinement of experimental X-ray data is limited to very good crystals with a high scattering power and molecules almost perfectly arranged in these crystals. Due to the very high number of parameters and correlations the multipole model is currently not applicable to problem structures. Furthermore, refinement of those solid-state structures would never meet all the figures of merit quoted in the previous chapter. The standard procedure at the beginning of an X-ray experiment for a multipole refinement is a detailed inspection of the low-order reflections with $\sin\theta/\lambda_{\max} = 0.625\text{\AA}^{-1}$, from which the electron density is mainly deduced, previous to a standard refinement. With this strategy some figures of merit are accessible within one day, including the data collection at the diffractometer with a detector position of $2\theta = 31^\circ$. After this process it has to be decided of whether the quality of the data in terms of a subsequent multipole refinement would be high enough.

This procedure was also employed with N-phenylpyrrole $\text{H}_4\text{C}_4\text{N}(\text{C}_6\text{H}_5)$ (**I**) (Figure 4.2) which crystallizes in thin plates. The result of the data collection to $\sin\theta/\lambda_{\max} = 0.625\text{\AA}^{-1}$ were very impressive – very small ADPs and residual density exclusively located at the bonds were detected. Hence, data collection was continued and a complete data set to $\sin\theta/\lambda_{\max} = 1.069\text{\AA}^{-1}$ suitable for multipole refinement was collected. To our surprise, the highest residual densities after including the high-order reflections in the refinement were no longer located on the bonds (Figure 4.1).

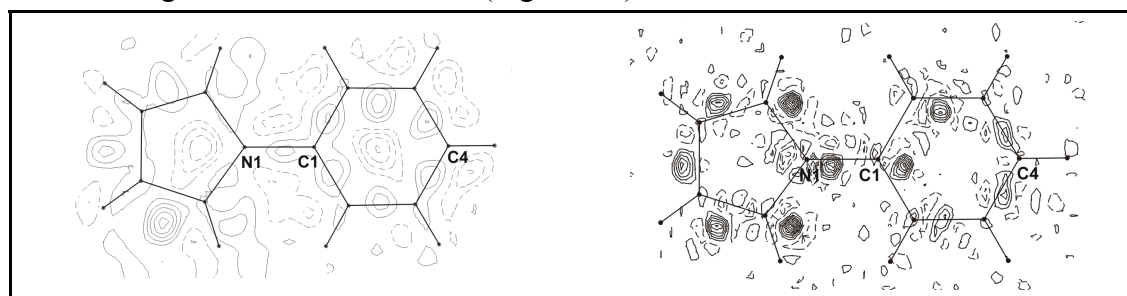


Figure 4.1 Contour plot of the residual densities in **I** after IAM refinement; left: refinement with reflections $\sin\theta/\lambda_{\max} = 0.625\text{\AA}^{-1}$; right: refinement with reflections $\sin\theta/\lambda_{\max} = 1.05\text{\AA}^{-1}$ and atomic positions from a high-order refinement with $\sin\theta/\lambda_{\min} = 0.85\text{\AA}^{-1}$. Stepwidth is $0.1\text{e}\text{\AA}^{-3}$; positive contours solid, negative contours dashed.

Several different multipole models were tested, but none of them accounted for the significant residual densities near the atomic positions of $\text{H}_4\text{C}_4\text{N}(\text{C}_6\text{H}_5)$ (**I**). However, straight connection of the residual electron density maxima from the high-resolution refinement provides the answer to the riddle: the measured crystal was twinned. Due to the merohedral twinning, with identical reciprocal lattices for both domains, the preliminary check in RLATT⁸⁹ did not display any problematic features.⁹⁰ One domain of the twin turned out to be rather small, small enough to be hidden from the low order scattering factors in the IAM which are, as already pointed out, affected from bonding densities.

Nevertheless, further efforts were made to describe all the electron density with a multipole refinement in this compound because dipolar systems like $\text{H}_4\text{C}_4\text{N}(\text{C}_6\text{H}_5)$ (**I**) attracted considerable attention since the discovery of the dual fluorescence.⁹¹ For a further elucidation of the structural changes accompanying and governing the excited state process in such molecules, the knowledge of the charge density distribution in the ground state is important.

The following parts of this chapter contain a detailed description how to refine a twinned structure with the multipole model. To our knowledge, this is the first time a twin was refined with the multipole model. The quality of the refinement was tested with the features listed in chapter 3.3.3. Topological properties were evaluated after the multipole refinement and compared with those from the closely related compound N-(4-fluorophenyl)pyrrole $\text{H}_4\text{C}_4\text{N}(\text{C}_6\text{H}_4\text{-}p\text{F})$ (**II**) depicted in Figure 4.2.

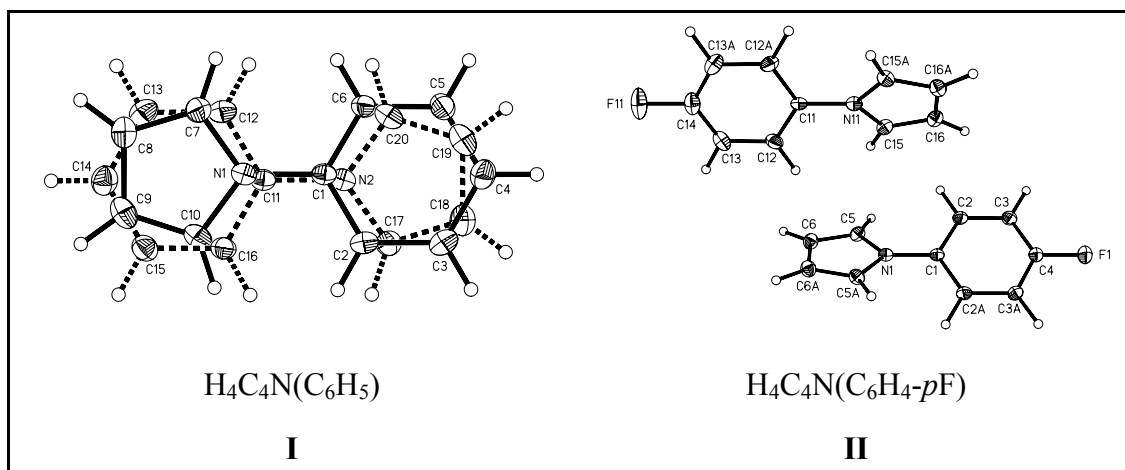


Figure 4.2 Molecular structures of **I** (left) and **II** (right). Anisotropic displacement parameters are depicted at the 50% probability level.

4.1 Refinement Strategy

Unfortunately, the XD program encloses no special facilities for twin refinement like SHELXL. But it is feasible to imply different types of constraints in the multipole refinement by introducing linear equations. They allow to constrain changes in the atomic coordinates, ADPs and multipole populations. Similar constraints are used in SHELXL to refine disorder. Thus, the twin was treated as a completely disordered molecule in SHELXL and XD.

The two domains of the twin were defined as two parts in SHELXL. In a first step, the atoms of the major domain (Part 1) were determined. Including the less biased high order reflections in the IAM refinement, and adjusting the atomic positions in a high-order refinement with $\sin\theta/\lambda_{\min} = 0.85\text{\AA}^{-1}$, revealed a number of high residual peaks identical in the total number of non-hydrogen atoms in phenylpyrrole. These peaks were defined as the non-hydrogen atoms of the much lower occupied domain (Part 2). The two parts were refined to an occupation of 90% for Part 1 and 10% for Part 2, respectively. Within the conventional (IAM) refinement compound **I** was refined using distance and similarity restraints as usual for disordered structures. The chosen estimated standard deviations (esds) for the restraints were much lower than suggested in the SHELXL manual. The ADPs of Part 2 were constrained to be equal to those of the main part, Part 1. All hydrogen atoms of both parts were assigned ideal positions and refined using a riding model. After the high-order refinement has converged, the hydrogen positions were shifted to ideal positions leading to the starting model for the multipole refinement.

Besides the standard procedure described in chapter 3.3.2 some additional commands were implied in the multipole refinement. At the beginning each *part* of the IAM refinement was defined as a *group*. Constraining the ADPs of the two groups seems to be a good approximation for a refinement of independent atoms, but the multipole model needs individual thermal displacement parameters for each molecule as shown by the residual maps. Therefore, the ADPs of group 2 were refined individually. However, due to an occupation of only 10% each ring in group 2 was only allowed to move as rigid body during the refinement.⁹² Furthermore, each multipole parameter of group 2 was constraint to be of 1/9 in population of the corresponding population parameter of group 1. To reduce the number of parameters the populations of positionally equivalent non-hydrogen atoms were constrained to be equal; leading to:

$$\begin{array}{llll} \text{C(3)} & = & \text{C(5)} & = & \text{C(13)} & = & \text{C(15)} \\ \text{C(2)} & = & \text{C(6)} & = & \text{C(12)} & = & \text{C(16)} \end{array}$$

in the phenyl rings and

$$\text{C}(7) = \text{C}(10) = \text{C}(17) = \text{C}(20)$$

$$\text{C}(8) = \text{C}(9) = \text{C}(18) = \text{C}(19)$$

in the pyrrole rings.

The multipole coefficients of all non-hydrogen atoms were constrained to obey local mirror plane symmetry (m); the mirror plane was defined as the plane through the non-hydrogen atom of the ring and two adjacent non-hydrogen atoms. The populations of the hydrogen atoms in each ring were also treated equal. The multipoles were refined to third order (octapolar level) for all non-hydrogen atoms, only a bond-directed dipole was refined for the hydrogen atoms, respectively. Different sets of κ and κ' values for all types of chemically different carbon atoms were introduced as well:

C1 (C11): *ipso* carbon atom bonded to N1 (N11) (κ -set 2)

C2-C6 (C12-C16): carbon atoms of the phenyl ring (κ -set 3)

C7/C10 (C17/C20): 2- and 5-position of the pyrrole ring (κ -set 4)

C8/C9 (C17/C20): 3- and 4-position of the pyrrole ring (κ -set 5)

This resulted in six κ -sets for the refinement. κ' of set 2, 3 and 5 was set to values from multipole refinements of theoretical structure factors⁹³ and kept fixed during the refinement; for the environment of the other atoms no κ' values from these calculations are currently available. Charger transfer between the two groups was not allowed during the refinement, proceeding along the following sequence: first the scaling factor, then κ together with P_v with fixed $\kappa(\text{H})$, P_{lm} of all atoms, P_v , κ , for all non-hydrogen atoms, followed by κ' for all non-hydrogen atoms. Then coordinates and thermal parameters of the non-hydrogen atoms, and finally all positional and thermal parameters were refined together with the multipolar coefficients (except κ') with $I > 2\sigma(I)$ and $\sin\theta/\lambda_{\max} = 1.05 \text{ \AA}^{-1}$ until convergence was reached.

Figure 4.3 shows an absolutely featureless residual density map after the multipole refinement including the twinning (right side). DMSDAs slightly exceeding $1 \cdot 10^{-3} \text{ \AA}^2$ are found for two bonds in the minor occupied group, namely the N2–C11 ($1.7 \cdot 10^{-3} \text{ \AA}^2$) and the C18–C19 bond ($1.5 \cdot 10^{-3} \text{ \AA}^2$). This is a convincing result for the individual description of thermal motion for a site-occupation of only 10%. All other bonds are in line with the rigid-bond criterion of Hirshfeld (3.3.3) indicating a proper deconvolution of the electron density from thermal motion.

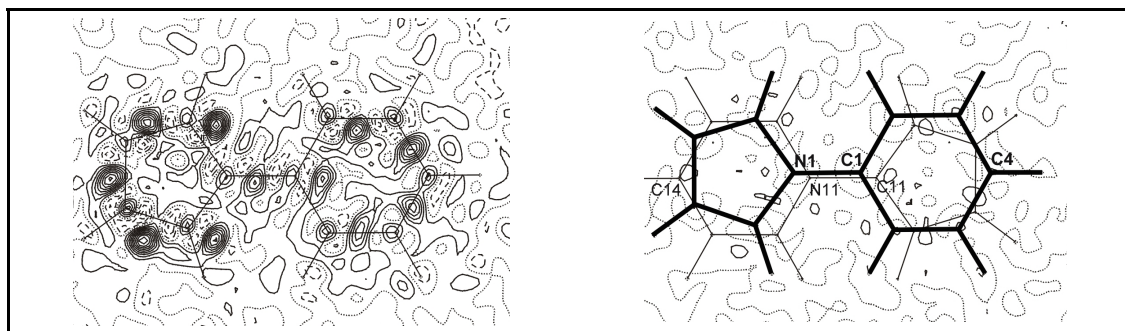


Figure 4.3 Contour plot of the residual densities after multipole refinement in **I**, $\sin\theta/\lambda_{\max} = 1.00\text{\AA}^{-1}$; left: refinement without twinning; right: refinement including twinning; the major site-occupation is highlighted in both.. Positive contours solid, zero contour dotted, negative contours dashed. Stepwidth is $0.1\text{e}\text{\AA}^{-3}$.

The results of the refinement are presented in Table 4.1 together with those of compound **II**, which was determined to elucidate the influence of a fluorine *para*-substitution on the electronic structure of this dipolar system. Moreover, **II** serves as a standard to judge for the quality of the multipole refinement of **I**. Both molecules are expected to have rather similar topological properties, slightly differing only due to the influence of the electronegative fluorine substituent in **II**.

N-(4-fluorophenyl)pyrrole (**II**) was subjected to a standard high-order refinement with $\sin\theta/\lambda_{\min} = 0.90\text{\AA}^{-1}$ and hydrogen atoms on idealized positions. Comparable local symmetry restrictions and similarity constraints for the multipole refinement similar to N-phenylpyrrole (**I**) were applied to **II**. The asymmetric unit of **II** contains two half molecules. In order to stabilize the first circles of the refinement and to reduce the number of parameters the multipole coefficients of each atom of the first molecule were constrained to be the same as those of the second molecule.

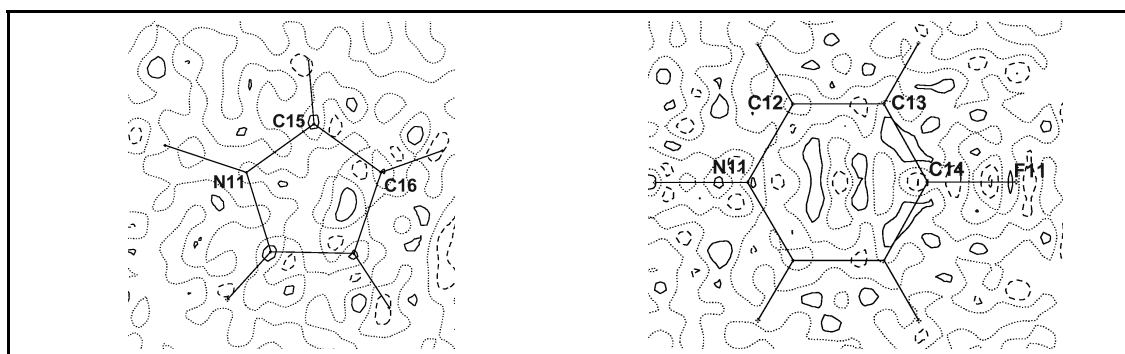


Figure 4.4 Contour plot of the residual densities after multipole refinement in one molecule (N11, F11, C11-C20) of **II**, $\sin\theta/\lambda_{\max} = 1.00\text{\AA}^{-1}$; left: plane of the pyrrole ring; right: plane of the phenyl ring. Positive contours solid, zero contour dotted, negative contours dashed. Stepwidth is $0.1\text{e}\text{\AA}^{-3}$.

The multipole populations of the atoms at general position were constrained to obey local mirror plane symmetry (m); the mirror plane defined as the plane determined by the non-hydrogen atom itself and the two closest neighbouring non-hydrogen atoms. In addition, the multipole populations of the non-hydrogen atoms at special positions were refined with restrictions arising from a 2-fold axis. As in $\text{H}_4\text{C}_4\text{N}(\text{C}_6\text{H}_5)$ (**I**), multipoles were refined to third order (octapole level) for all non-hydrogen atoms. The local symmetry restrictions and similarity constraints concerning the hydrogen atoms are equal to **I**. Moreover, different sets of κ and κ' values for all types of chemically different carbon atoms were also introduced:

C1 (C11):	<i>ipso</i> carbon atom bonded to N1 (N11)	(κ -set 3)
C2/C3/C6 (C12/C13/C16):	carbon atoms bonded to other carbon atoms	(κ -set 4)
C4/C14 (C17/C20)	bonded to F1(F11)	(κ -set 5)
C5/C15 (C17/C20)	bonded to N1(N11)	(κ -set 6)

This gives seven $\tilde{\kappa}$ -sets for the refinement. κ' of set 1, 2 and 5 again were fixed at values from multipole refinements of theoretical structure factors.⁹³ Each molecule was refined as rigid-body and charge transfer between the two molecules was not allowed during the refinement, following the same strategy as with **I**. In the final step, the similarity constraints for positional equivalent atoms of the two molecules were removed and the two molecules were refined independently due to the different torsion angles of the two ring systems of each molecule. The DMSDAs after the refinement are excellent: the highest amplitude is $0.7 \cdot 10^{-3} \text{ \AA}^2$. The featureless residual density maps are depicted in Figure 4.4.

4.2 Structure Discussion

The comparison of the structural parameters of N-phenylpyrrole (**I**) and N-(4-fluorophenyl)pyrrole (**II**) is based on the geometrical output of the multipole refinement, as the multipole approach leads to the best estimate of the bond lengths and angles without bias from undescribed bonding densities.

As shown for 4-Aminobenzonitriles with aliphatic substituents at the amino N atom, a detailed examination of the molecular structure in the ground state is the first step for a further elucidation of the structural changes accompanying excited states in dipolar compounds.⁹⁴ The pyramidal character of the pyrrole N atoms, the twist angles around the phenyl–pyrrole bonds and the changes in bond lengths due to changes in the aromatic character of the phenyl rings in **I** and **II** are of mayor interest.

Table 4.1 Crystallographic data for compounds **I** and **II** after multipole refinement.

compound	I	II
formula	C ₁₀ H ₉ N	C ₁₀ H ₈ F N
crystal system	orthorhombic	monoclinic
space group	P2 ₁ 2 ₁ 2 ₁	P2/c
a [Å]	5.6405(2)	9.2746(2)
b [Å]	7.5996(2)	10.8053(3)
c [Å]	17.6532(2)	9.0264(2)
β [°]	90	118.810(2)
V [Å ³], Z	756.6(13), 4	792.61(3), 4
μ [mm ⁻¹]	0.07	0.10
T _{min} / T _{max} (low-angle batch)	0.93 / 0.98*	0.89 / 0.98*
T _{min} / T _{max} (high-angle batch)	0.91 / 0.98*	0.78 / 0.98*
refl.used in the multipole refinement		
after cut-off**	6529	62860
sinθ / λ _{max, cut} [Å ⁻¹]	1.05	1.00
completeness to sinθ / λ _{max, cut} [%]	99.6	99.9
no. of unique reflections (low-angle batch) / R _{int}	1547 0.0229	1718 0.0270
no. of unique reflections (high-angle batch) / R _{int}	6884 / 0.0436	6065 / 0.0687
limiting indices	-12 ≤ h ≤ 12, 0 ≤ k ≤ 16, 0 ≤ l ≤ 38	-18 ≤ h ≤ 16, -0 ≤ k ≤ 22, 0 ≤ l ≤ 18
Flack X parameter ⁹⁵	-0.10 (11)***	-
max. shift / esd in final cycle	0.12 · 10 ⁻¹	0.37 · 10 ⁻¹
R1 (I>2σ(I)) after IAM refinement to sinθ / λ _{max, cut}	0.0438	0.0632
wR2 (I>2σ(I)) after IAM refinement to sinθ / λ _{max, cut}	0.1109	0.1183
R1 (I>2σ(I)) after multipole refinement to sinθ / λ _{max, cut}	0.0257	0.0581
wR2 (I>2σ(I)) after multipole refinement to sinθ / λ _{max, cut}	0.0340	0.0519
GoF	2.02	2.50
N _{refl.} / N _{param.}	29.68	29.70

* Standard value for the absorption correction program SADABS suggested from the author of the program; exact value not calculated during absorption correction.

** with respect to these cut offs: sinθ / λ_{max} and I>2σ(I)

*** indicates, that the absolute structure could not be determined successfully.

All these features are affected most during a promotion of the molecules to an excited state. Rotation about the N–phenyl bond is one of the models to describe the origin of the dual fluorescence;⁹⁶ a low rotational barrier is obligate for this mechanism. In another mechanism, Zachariasse assumes that inversion at the nitrogen atom is very important for the effect of dual fluorescence.⁹⁷ The nitrogen atom in both discussed systems is part of a five membered ring. The geometrical features at that nitrogen atoms serves as a comparison to N-substituted phenyl rings with non-cyclic substituents. The influence of electronegative substituents on these parameters can be deduced from the *para*-fluorinated derivative **I** (Figure 4.2).

The twist angle θ , defined as the angle between the plane of the pyrrole and the phenyl ring, respectively, is only 5.6° for $\text{H}_4\text{C}_4\text{N}(\text{C}_6\text{H}_5)$ (**I**), while it increases to 21.8° and 27.6° in the two molecules of $\text{H}_4\text{C}_4\text{N}(\text{C}_6\text{H}_4\text{-}p\text{F})$ (**II**), although the steric requirements are the same. The sum of the angles at the nitrogen atom is not in accordance with a noticeable pyramidality caused by a stereochemically active lone-pair. In both compounds this sum is 360° , the ideal value for a planar $\text{N}(\text{sp}^2)$ atom but considerably different to a partially tetrahedral environment often found in dialkyl-aminobenzonitriles.^{94,98} A partial chinoidal structure would be evident from different bond lengths in the phenyl ring; especially the C2–C3 bond in **I** (C2–C3 and C12–C13 in **II**) are expected to be shorter. The differences found cluster around 0.01\AA , indicating no significant contribution of a chinoidal form neither in **I** nor in **II**. The observed N–phenyl bond lengths ($1.4197(6)\text{\AA}$ in **I**; $1.4153(13)\text{\AA}$ (N1–C1) and $1.4198(13)\text{\AA}$ (N11–C11) in **II**) are considerably shorter than standard $\text{N}(\text{sp}^2)\text{--C}(\text{sp}^2)$ single bonds⁹⁹ but rather long for N-substituted phenyl rings.¹⁰⁰

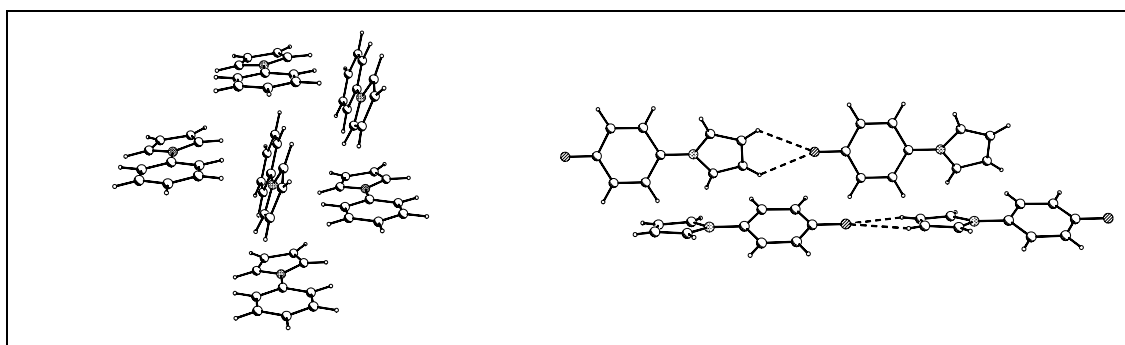


Figure 4.5 Crystal packing in $\text{H}_4\text{C}_4\text{N}(\text{C}_6\text{H}_5)$ (**I**, left) and $\text{H}_4\text{C}_4\text{N}(\text{C}_6\text{H}_4\text{-}p\text{F})$ (**II**, right).

A head-to-tail herring-bone stacking of the molecules is found in the crystal of **I**, with the molecules far from a coplanar arrangement. In the crystal of **II** the molecules form chains via bifurcated $(\text{C}\text{--}\text{H})_2\cdots\text{F}\text{--}\text{C}$ hydrogen bonds. Every second chain runs in the

opposite direction. The angle between the two mean planes of the chains is almost exactly rectangular (90.3°). The distance between fluorine and the hydrogen atoms of neighbouring molecules is 2.717\AA in one orientation and 2.639\AA in the other. Both distances are in the range quoted for weak $\text{C-H}\cdots\text{F-C}$ hydrogen bonds. (Figure 4.5).¹⁰¹

Considering all facts, i. e. the planar environment of the nitrogen atom, a marginally shortened N-phenyl single bond and a relatively low steric demand of the pyrrole system, free rotation about the N-phenyl bond should be possible. Inversion at the $\text{N}(\text{sp}^2)$ atom in an aromatic system is impossible. Referring to the crystal structures, intermolecular charge transfer between the head-to-tail arranged dipolar compounds and even from the T-shaped stacking should be considered¹⁰² in the discussion about the electronic changes in the excited state.

4.3 Discussion of Electronic Properties

A much more precise picture of the ground state is achieved after analysing the results of the multipole refinement. The electronic situation in $\text{H}_4\text{C}_4\text{N}(\text{C}_6\text{H}_5)$ (**I**) and $\text{H}_4\text{C}_4\text{N}(\text{C}_6\text{H}_4\text{-}p\text{F})$ (**II**) is evaluated from different properties: the position of the BCPs, the deformation density, the Laplacian along the bond path, the charges from the integration over the atomic basins and the electrostatic potential (ESP) serve as criteria for the interpretation of the charge density distribution. Many studies on topological properties of compounds containing C–C and C–N bonds have already been published in the last decade.¹⁰³ This is important to judge the results of the twin refinement of **I**. Of course, the charge distribution in each molecule is unique, but e. g. values of the Laplacian at the BCP in the C–C bonds should not differ much from closely related systems. In addition, the inspection of the electron density distribution in **II** is expected to reveal some differences from **I**, mainly caused by the *para*-fluorine substitution at the phenyl ring.

The BCPs of all aromatic C–C bonds in the phenyl ring of **I** are slightly shifted towards the *ipso*-C atom located closer to the electronegative nitrogen atom of the pyrrole ring. Electron density $\rho(\mathbf{r}_{\text{BCP}})$ and the Laplacians $\nabla^2\rho(\mathbf{r}_{\text{BCP}})$ of the aromatic C–C bonds in the phenyl ring show an obvious trend, the value for $\rho(\mathbf{r}_{\text{BCP}})$ increases and the Laplacian gets more negative the closer the bond is located to the nitrogen atom. This is a clear indication for a shift of electron density towards the pyrrole substituent. A chinoidal character of the phenyl ring can not be deduced from the bonding properties. The average values of $\rho(\mathbf{r})$ and $\nabla^2\rho(\mathbf{r})$ at the BCP in the phenyl ring are $\rho(\mathbf{r}_{\text{BCP}}) = 2.154(121)\text{e}\text{\AA}^{-3}$ and $\nabla^2\rho(\mathbf{r}_{\text{BCP}}) = 19.448(2.276)\text{e}\text{\AA}^{-5}$, respectively. This is in excellent agreement with recent charge density studies of compounds including phenyl

rings.¹⁰⁴ Comparison of the pyrrole ring is more difficult because topological analyses of this heterocycle are not published. Nevertheless, all topological parameters of the aromatic bonds are in the normal range anticipated for slightly polarized aromatic bonds. This enables an adequate description of the bonding properties also in this part of the molecule.

Table 4.2 Topological properties of the *ipso*-C–N and C–F bonds in **I** and **II** at the BCP.

A–B	compound	d(A–B)	d(A–BCP)	d(BCP–B)	$\rho(\mathbf{r}_{\text{BCP}})$	$\nabla^2\rho(\mathbf{r}_{\text{BCP}})$
C1–N1	I	1.4197	0.5834	0.8363	1.944(4)	-15.850(35)
C1–N1	II	1.4153	0.5841	0.8313	2.063(8)	-18.664(33)
C11–N11	II	1.4198	0.5708	0.8490	2.023(12)	-17.749(49)
C4–F1	II	1.3560	0.5715	0.7846	2.077(15)	-14.942(57)
C14–F11	II	1.3597	0.5310	0.8287	1.971(20)	-18.196(86)

$d(\text{A–B})$ is the bond path length between the atoms A and B [\AA], $d(\text{A–BCP})$ and $d(\text{B–BCP})$ denote the distances of the atoms A and B from the BCP [\AA], $\rho(\mathbf{r}_{\text{BCP}})$ [$\text{e}\text{\AA}^{-3}$] is the charge density and $\nabla^2\rho(\mathbf{r}_{\text{BCP}})$ [$\text{e}\text{\AA}^{-5}$] the Laplacian at the BCP, respectively.

Compared to $\text{H}_4\text{C}_4\text{N}(\text{C}_6\text{H}_5)$ (**I**), the polarization of the electron cloud of the phenyl ring in $\text{H}_4\text{C}_4\text{N}(\text{C}_6\text{H}_4\text{-}p\text{F})$ (**II**) is established in the opposite direction. The Laplacian at the BCP of the C–C-bonds in the phenyl ring of **II** is more negative and the electron density at this point increases in the bonds closer to the fluorine substituent. Averaged values for the topological properties in the phenyl ring ($\rho(\mathbf{r}_{\text{BCP}}) = 2.232(110)\text{e}\text{\AA}^{-3}$ and $\nabla^2\rho(\mathbf{r}_{\text{BCP}}) = 21.460(3.602)\text{e}\text{\AA}^{-5}$) indicate a higher charge concentration in this residue compared to **I**. The bonding properties of the pyrrole ring are almost equal in **I** and **II**. Only the slightly shifted positions of the BCPs indicate a marginally less pronounced polarization in **I**. This is tentatively assigned to the small long-range influence of the *para* fluorine atom that has a electron withdrawing effect on the σ -bond-skeleton and effects even these bonds (Figure 4.6). The topological properties of the two C–F bonds, with averaged $\rho(\mathbf{r}_{\text{BCP}}) = 2.024(53)\text{e}\text{\AA}^{-3}$ and $\nabla^2\rho(\mathbf{r}_{\text{BCP}}) = 16.569(1.627)\text{e}\text{\AA}^{-5}$ are similar to quantitative results obtained in earlier studies.¹⁰⁴ Moreover, even the weak $(\text{C–H})_2\cdots\text{F–C}$ hydrogen bonding is further substantiated by the existence of a (3, -1) BCP for each hydrogen bond with typical topological properties.¹⁰⁵

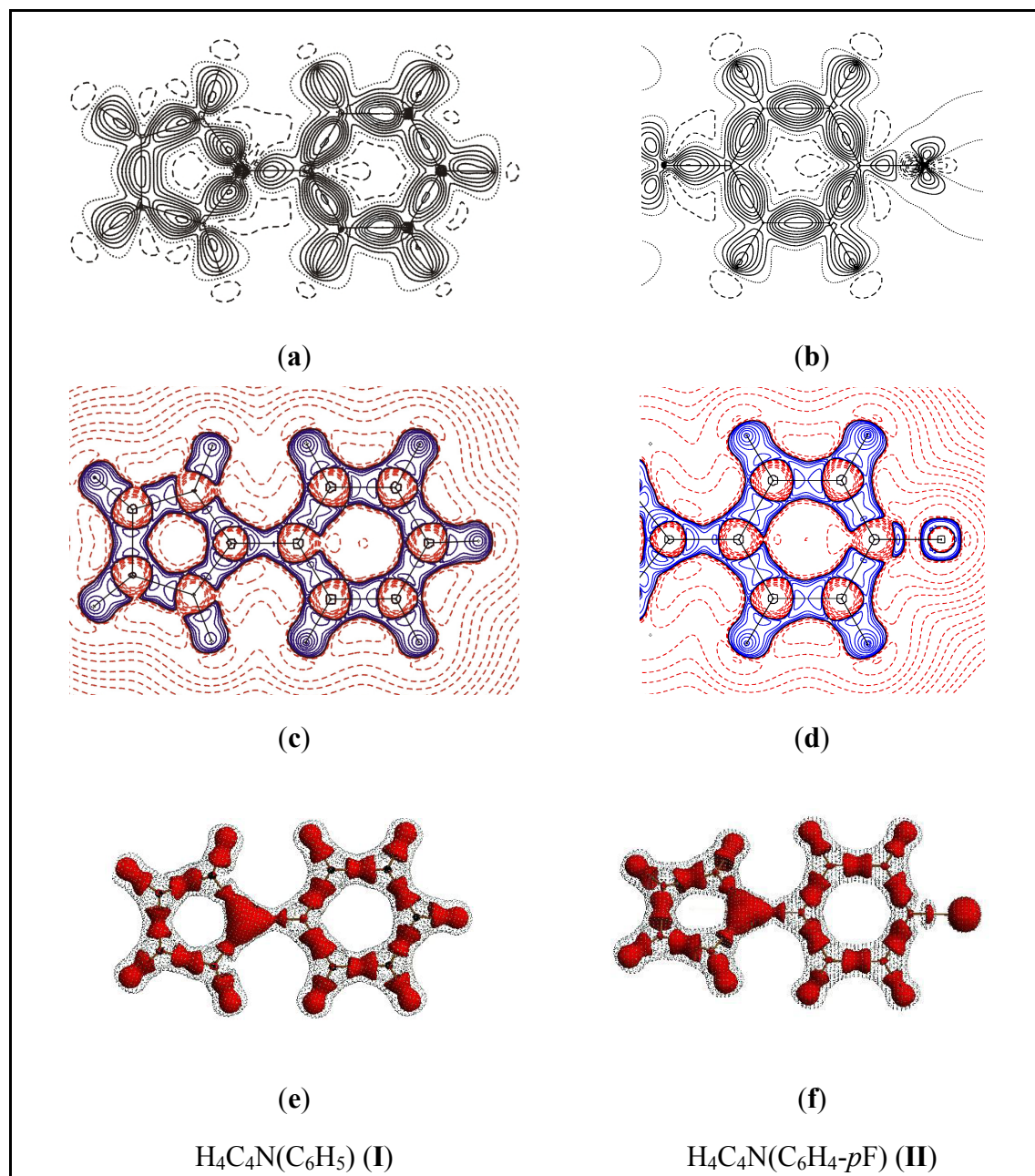


Figure 4.6 Contour and isosurface plots of **I** (left) and **II** (right); orientation of the molecules as in Figure 4.2; due to the high twist angle between the two ring planes the contour plots of **II** display only the phenyl plane: (a)-(b) contour plots of the static deformation density in the N1–C1–C2 (a) and the N1–C4–C3 plane (b); positive contours solid, negative contours dashed; zero contour dotted. Stepwidth is $0.1\text{e}\text{\AA}^{-3}$; (c)-(d) contour map of the Laplacian in the same planes; negative contours in blue, positive contours in red; zero contour dotted in black; contours drawn at $0.000, \pm 2.0 \cdot 10^n, \pm 4.0 \cdot 10^n, \pm 8.0 \cdot 10^n \text{e}\text{\AA}^{-5}$, where $n = 0, -3, \pm 1, \pm 2$. (e)-(f) Isosurface representation of the Laplacian with the dotted isosurface at the $0\text{e}\text{\AA}^{-5}$ level and the red isosurface plotted at the $-10\text{e}\text{\AA}^{-5}$ level.

Equivalent bonds in the two molecules of the asymmetric unit in **II** are assigned slightly different topological values. This effect is the result of the exclusive inspection of the properties at the BCP. The positional changes are very small, but they are sufficient to

lead to appreciable differences of approximately $1.5\text{e}\text{\AA}^{-5}$ in the Laplacian between the two molecules of **II**. Therefore, the Laplacian of the N–C bond in both molecules is monitored along the whole bondpath. The comparison shows an almost equal Laplacian distribution in this bond for **I** and both molecules of **II**. In general, this is another clear indication for a successful multipole refinement of twinned **I**. In detail, the value of $\nabla^2\rho(\mathbf{r}_{\text{BCP}})$ at the BCP is more negative in **II**, indicating a slightly more pronounced charge concentration in the N–C bond of **II**; this trend is maintained throughout the whole bonding region. The differences are only very small, but reveal a higher charge concentration in **II** due to a marginally less polarized N–C bond. Figure 4.7(a) shows the bonding region of the N–C bonds. Figure 4.7(b) visualises the necessity of a Laplacian inspection in the entire bonding region for polar bonds. Despite $\nabla^2\rho(\mathbf{r})$ at the BCP is almost equal for the depicted homo and heteronuclear bonds, the Laplacian distribution along the bonding vector is completely different for C–C, N–C and C–F.

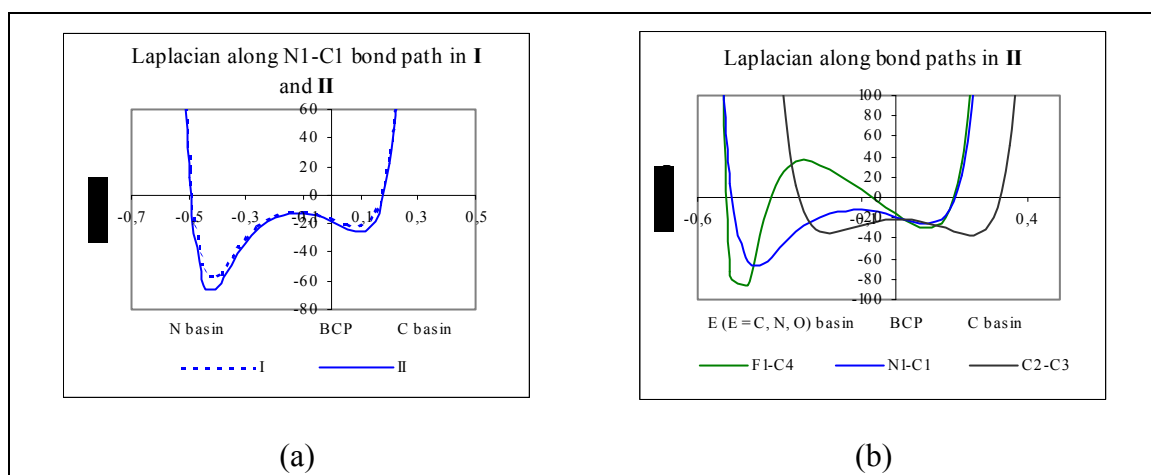


Figure 4.7 Laplacian distribution along the bondpaths in **I** and **II**. (a) compares the N–C(ipso) bonds in **I** and **II**; (b) comparison of three bonds in **II** with different polarity. X-axis gives the distance to the BCP in Å, y-axis the Laplacian in $\text{e}\text{\AA}^{-5}$.

Charges from the integration over the topological basins in the phenyl rings, the nitrogen and the fluorine atoms support the findings from the topological analyses (Table 4.3).

Table 4.3 Charges from the integration over the atomic basins in **I** and **II**, given in electrons (e).

	N1(N11)*	C1(C11)	C2(C12)	C3(C13)	C4(C14)	F1(F11)
I	−1.35	+0.60	−0.10	−0.32	−0.34	–
II	−1.21(−1.18)	+0.40(+0.40)	−0.06(−0.06)	−0.09(−0.09)	+0.47(+0.47)	−0.65(−0.65)

* Brackets for the atoms of the second molecule in the asymmetric unit of **II**.

The charge of the nitrogen atom in $\text{H}_4\text{C}_4\text{N}(\text{C}_6\text{H}_5)$ (**I**) is more negative than the N atom in $\text{H}_4\text{C}_4\text{N}(\text{C}_6\text{H}_4\text{-}p\text{F})$ (**II**). The polarization introduced from the nitrogen atom is mirrored from the charges of the carbon atoms in **I**. The N-bonded C atom has a distinct positive charge, the charges for all other carbon atoms of the phenyl ring are increasingly negative the longer the distance to the nitrogen atom gets. In **II**, charges of the phenyl ring carbon atoms at the 2-, 3-, 5- and 6-positions between the electronegative atoms fluorine and nitrogen are almost neutral while those bonded to the electronegative atoms reveal high positive charges. The two dimensional representation of the atomic basins in both phenylpyrroles is depicted in Figure 4.8.

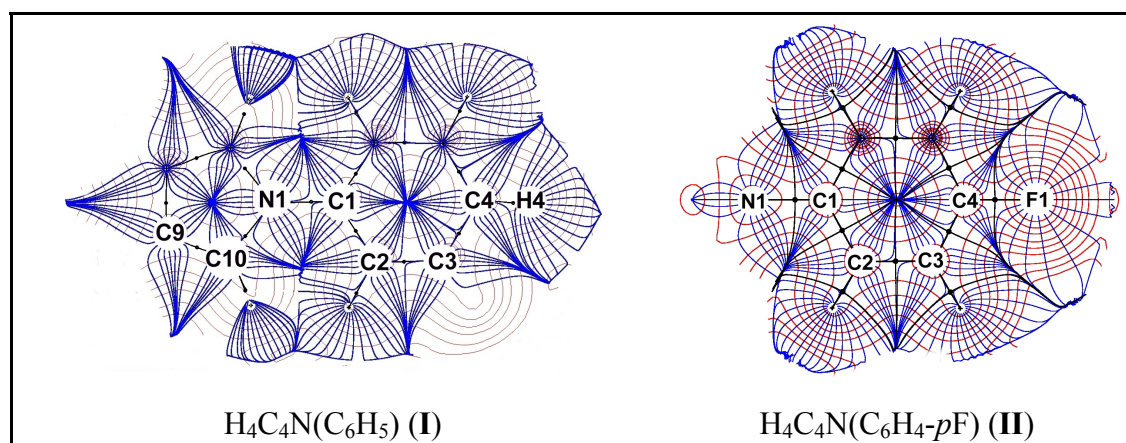


Figure 4.8 Trajectory plot of **I** (left) and **II** (right) in the N1–C1–C2 plane (left) and the N1–C4–C3 plane (right), respectively. Blue lines denote the electron density, red lines trajectories of the electron density; bond path and the BCPs are drawn in black.

It was a priori assumed that the fluorine substitution also causes changes in the dipole moment. For $\text{H}_4\text{C}_4\text{N}(\text{C}_6\text{H}_5)$ (**I**), the dipole of a magnitude of 1.5 [D], calculated from equation 2.15, is oriented exactly along the C–N bond,. The dipole moment in $\text{H}_4\text{C}_4\text{N}(\text{C}_6\text{H}_4\text{-}p\text{F})$ (**II**) is by more than a magnitude smaller (0.1 [D]) and directed opposite to the orientation in **I** (Figure 4.9).

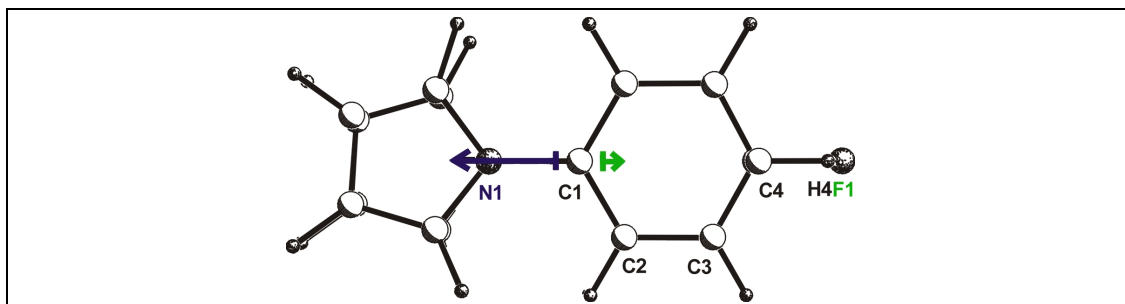


Figure 4.9 Superposition of the molecules **I** and **II** with their dipole moments. Origin of the dipole vector is the centre of mass. The length of the vector is proportional to the magnitude of the dipole.

The electrostatic potential (ESP) underlines the differences found for the two phenylpyrroles. The negative potential in **I** is located mainly above and below the aromatic ring systems, while the negative potential at the phenyl ring vanishes in **II**. It is exclusively located at the fluorine atom. The areas with negative potentials on top and bottom of the pyrrole systems are polarized towards the nitrogen atom in both compounds. Figure 4.10 shows an isosurface representation of the ESP of the two different phenylpyrroles. Due to almost equal potentials in both molecules of **II**, only one is depicted in this plot.

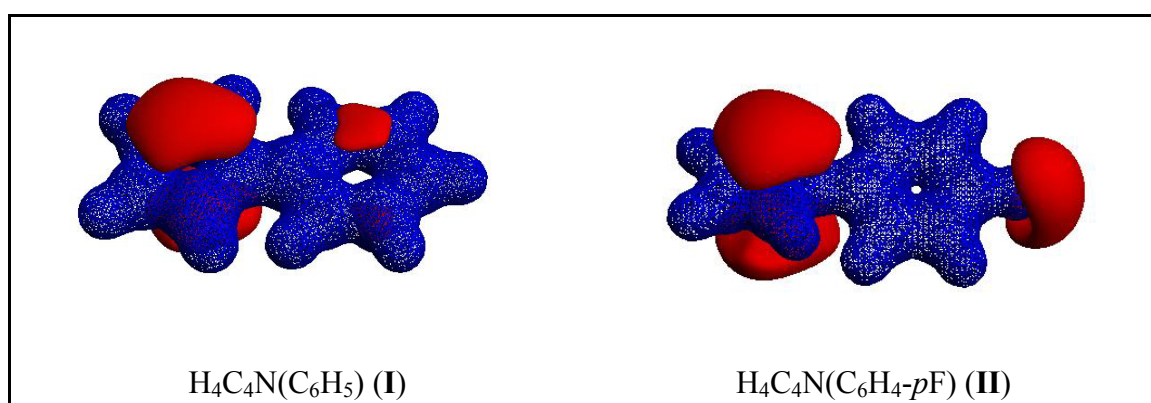


Figure 4.10 Electrostatic potential of **I** (left) and **II** (right); the molecules are drawn in the same orientation as in Figure 4.2. The red isosurface displays the negative potential at the $-0.08\text{e}\text{\AA}^{-1}$ level, the blue isosurface the positive at the $+0.30\text{e}\text{\AA}^{-1}$ level, respectively.

The results of the multipole refinement and the topological analyses affirm that it is possible to derive the exact electron density distribution even from problematic samples like twins or disordered structures, provided that the scattering power is high and numerous constraints are implemented to the multipole refinement. However, special care is needed for the choice of the local coordinate systems for the part of the molecule the constraints refer to. An inadequate constraint description would decrease

the quality of the refinement because the error is reproduced from the constraints a second time.

In general, we regard the discussed results to be very important for recent research in chemistry, as they guide the way to charge density studies even if the quality of the sample is not superior. Most synthetic chemists need to crystallize compounds with coordinated or non-coordinated solvent molecules in the asymmetric unit that suffer from disorder. Even those more realistic crystal structures might be promising candidates for charge density studies in the future. However, further studies on other systems have to be carried out to insure the transferability of these results. Some attempts with disordered, coordinated solvent molecules are presented in the next chapter.

5 Results and Discussion

Almost all inorganic compounds contain highly polar bonds. Lots of them in the centre of the molecule, e. g. hexacoordinated organosilicon compounds, others in the periphery, e. g. metal-phosphorus compounds. Although the properties of the polar bonds are of major importance for the physical characteristics of the compounds in all cases, experimental studies on these bonds are still rare, especially for highly polar bonds containing an element of the third row in the periodic table.¹³

The basis of all studies in this thesis is the charge density distribution derived from a multipole refinement of experimental X-ray data. The results of the refinements were analyzed in detail. An essential tool for the examination is Bader's AIM theory.⁹

In the first part of this chapter interest is focused on highly polar bonds including one third row element. Si–N bonds are studied in silicon compounds with tetra- and hexacoordinated silicon, respectively, P–N and P–C bonds in a lithiated iminophosphorane with a heteroaromatic ligand. In the second part, bond types enclosing lithium, Li–E (E = C, N, O), are investigated. The results of each part are summarized and compared to results derived in other studies.¹⁰⁶

5.1 Multipole Refinement and Topological Analysis of Highly Polar Bonds

The polarity of bonds makes the analysis considerably more difficult than with homonuclear bonds of second-row elements. An electronegative atom tends to expand its valence shell, the electropositive to contract the outer shell. To account for these changes, expansion and contraction factors are implemented in the multipole model. However, the radial screening factor for the valence deformation density, κ' , is the most sensitive parameter in any refinement; detailed studies which describe the influence of this parameter are published.¹⁰⁷ Nevertheless, it is necessary to refine the κ' parameters of atoms included in highly polar bonds to account for the different behaviour of their valence shells.¹⁰⁸ Hence, κ' is included in each refinement, but it is exclusively refined when the refinement of the other parameters has converged. In the final step, the previously adjusted κ' is not refined together with the other parameters.

Another problem is the position of the BCP in highly polar bonds. Different to $\rho(\mathbf{r})$ and $\nabla^2\rho(\mathbf{r})$ in non-polar bonds, the distribution of these properties along the bond path is severely asymmetric. The position of the BCP is located closely to the electropositive atom, where the Laplacian changes dramatically with very small changes in the position.¹⁰⁹ Therefore, the Laplacian of all investigated highly polar bonds is monitored along the entire bonding region.

Furthermore, differences in the topological properties of experimental and theoretical data are always present for polar bonds. The quantitative agreement between the topological properties is, in almost all cases, relatively poor. Many studies have tried to locate the origin for these discrepancies. The most recent paper from Volkov et. al. gives a very detailed description of the problem.¹¹⁰ Moreover, theoretical calculations of the presented compounds would be very time consuming and convergence is always an immanent problem. Consequently, the results of this work are exclusively based on experimental data.

Topological analysis of highly polar bonds in inorganic compounds with more than 20 non-hydrogen atoms is a rather new field of research. One question is of whether these bonds are mainly dominated by covalent or by ionic contributions. For the quantitative elucidation of this controversy several features in addition to the topological properties at the BCP have to be examined. The properties used for the classification in this thesis were introduced in chapter 2.5.5.

5.2 Charge Density Studies on Compounds containing Si–N Bonds

The silazanes studied in this thesis are octamethylcyclotetrasilazane [*c*-{Me₂Si–N(H)}₄] (OMCTS) (**III**) and the metallated derivatives dilithiooctamethylcyclotetrasilazane [(thf)₂Li₂-*c*-{Me₂Si–N(H)–Me₂Si–N}₂]₂ (**IV**, dianion) and alumolithiooctamethylcyclotetrasilazane [(thf)₂LiAl-*c*-{Me₂SiN}₄]₂ (**V**, tetraanion), Figure 5.1 (a)-(c); **III-V** are also depicted on a large sheet at the end of the thesis. They are ideally suited for an investigation of this bond type because each sample contains eight Si–N bonds with differently metallated nitrogen atoms. Thus, the bonding properties in these samples, with tetrahedral environment of the silicon atoms, can be evaluated from averaged data.

Furthermore, the Si–N bond in the hexacoordinated silicon complex difluoro-bis-[N-(dimethylamino)phenylacetimidato-N,O]silicon, {PhC(O)NNMe₂}₂SiF₂ (**VI**, Figure 5.1, (d)) is studied. The properties of this much longer Si–N bond turned out to be noticeable different compared to those in **III-V**.

Other types of highly polar bonds of interest for this thesis are present in compound **IV** and **V**. The Li–E (E = N, O) bonds are discussed in detail later in chapter 5.

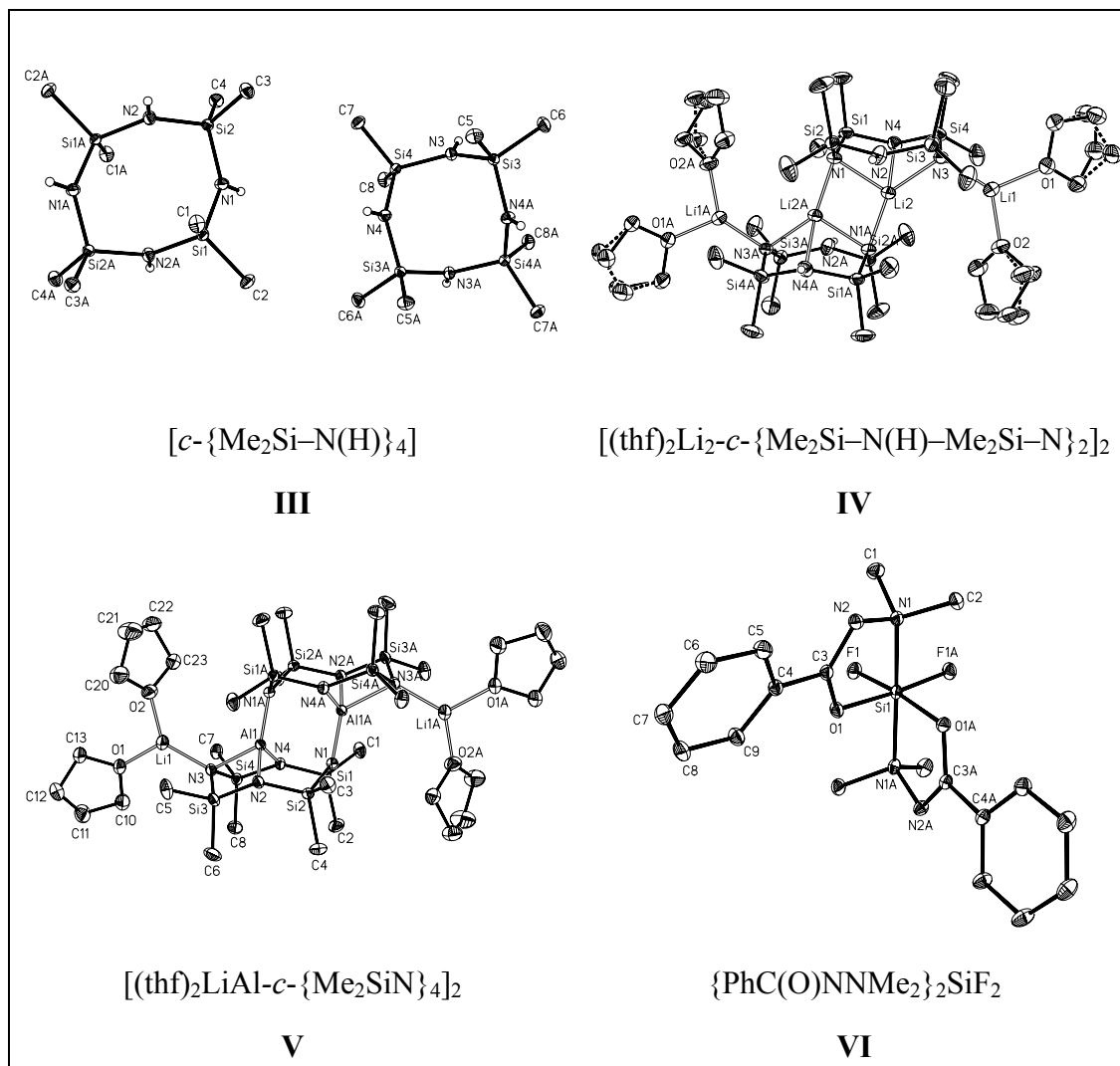


Figure 5.1 Labeled solid-state structures of **III** (a), **IV** (b), **V** (c) and **VI** (d). Anisotropic displacement parameters are depicted at the 50% probability level. Hydrogen atoms but those of the N–H moieties omitted for clarity.

5.2.1 Si–N in Tetracoordinated Silicon Compounds

The characteristics of the Si–N bonds in **III**–**V** are compared. Changes in the environment of the nitrogen atoms, e. g. from OMCTS with a hydrogen atom bonded to each N atom to the tetraanion with no N–H bond are expected to be accompanied by significant modifications of the bonding properties. It was anticipated that the stepwise metalation would even affect the Si centres although they are always bonded to two nitrogen atoms and two methyl groups in **III**–**V**.

The disordered THF molecules in **IV** serve as an additional test for the applicability of the multipole model on problematic samples discussed in the previous chapter. Experiences from the refinement of **I** are helpful for the refinement of the disorder in **IV**, but the main difference between these two samples is the conformational stability of the disordered part. Planar aromatic phenyl and pyrrole systems are rigid, the angles and bond lengths between the sp^2 nitrogen and carbon atoms are almost exactly identical in all samples, while rotations about the single bonds in THF cause a unique conformation for each moiety.

5.2.1.1 Molecular Structures

The crystal structure of the parent OMCTS has been determined at room temperature in the early sixties from Smith et al.¹⁴ The solid-state structure, now based on data collected at 100(2)K, consists of two different conformers (Figure 5.1 (a)), present in a 1:1 ratio. One ring with a chair conformation shows a centre of inversion (1), the second, with a boat conformation contains a two fold axis (2). Each of the residues emulates the higher symmetry: the chair is close to $2/m$ while the boat almost has a 4 axis in the ring centre. Although two conformers are present in the same lattice neither the Si–N–Si ($132(2)^\circ$) nor the N–Si–N ($111(2)^\circ$) angles hardly show any deviations. The same remarkable homogeneity is found for the Si–N bond length. The average distance in the eight independent Si–N bonds is $1.7250(46)\text{\AA}$, slightly below the standard length for a Si–N single bond.^{100,111} The nearly ideal tetrahedral environment of each Si atom is completed from two carbon atoms with an average Si–C distance of $1.8665(25)\text{\AA}$ and a tetrahedral C–Si–C angle of $110(2)^\circ$.

A completely different situation is found in **IV** and **V**. Only the eight Si–C bond lengths and angles keep rather invariant at each Si atom. Compared to OMCTS they are slightly elongated in the dianion, **IV**, ($1.8792(121)\text{\AA}$) and in the tetraanion, **V**, ($1.8775(62)\text{\AA}$). The above mentioned C–Si–C angle is reduced to $104(2)^\circ$ in **IV** and $103(2)^\circ$ in **V**, respectively.

Both, the dianion and the tetraanion, crystallize as dimers with two eight-membered rings which approximate a crown conformation. The two ring centres are shifted by about a radius and arranged with an indentation pointing mutually to the ring centre. Crystallographically, the two Si_4N_4 perimeters are related *via* a centre of inversion in the middle of a four-membered M_2N_2 -heterocycle located between the two silazane rings. The planes of these heterocycles made up from two nitrogen and two lithium atoms in **IV** and two nitrogen and two aluminium atoms in **V**, respectively, are perpendicular to the two Si_4N_4 crowns. The distortion of the crown is only marginal in

the dianion, while it is more emphasized in the tetraanion. The differences in the transannular nitrogen atom distances are approximately 0.8 Å in **IV** and 1.1 Å in **V** (Figure 5.2).

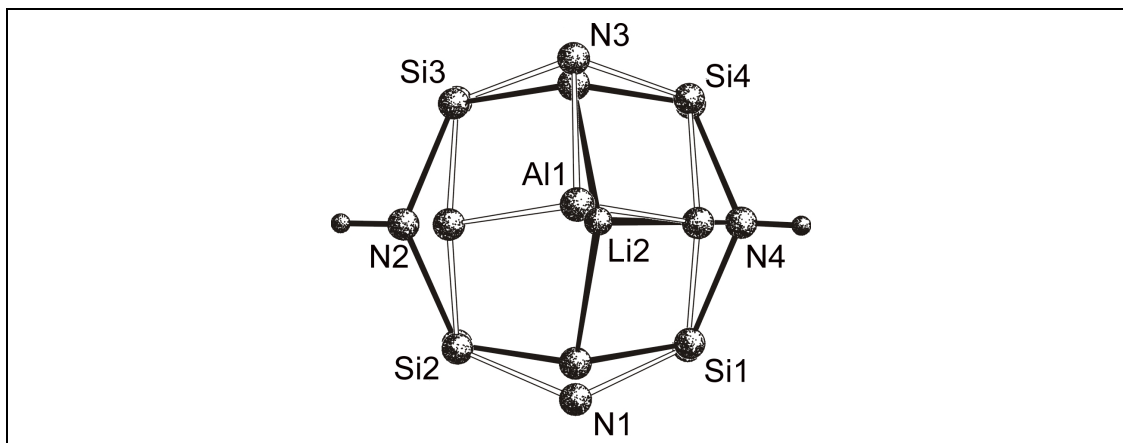


Figure 5.2 Superposition of the Si_4N_4 heterocycles in **IV** and **V** depicting the different ring deformations. The bonds in **IV** are drawn solid, those in **V** with open lines, respectively.

In **IV** and **V** the eight Si–N bonds in each molecule are no longer equivalent. Two different types can be distinguished in the dianion. The first type contains the hydrogen substituted nitrogen atoms, the second the deprotonated nitrogen atoms. The averaged Si–N bond length of the first set of 1.7442(125) Å is about 6.2 pm longer than the latter (1.6826(27) Å). This deviation is in accordance with theoretical ab-initio calculations on model compounds.¹¹² In the tetraanion three Si–N bond types can be distinguished. All nitrogen atoms are deprotonated and the differences are induced by the coordinated metal atoms. In four Si–N bonds the N atoms N2 and N4 are bonded to the aluminium atom Al1 located on top of the eight-membered heterocycle in the same asymmetric unit. They show an average Si–N distance of 1.7056(48) Å. The second group comprises the two Si–N bonds formed by the nitrogen atom N3 which is bonded to two different metal centers (Li and Al). The averaged bond length of this group is 1.7429(18) Å, about 4 pm longer than in the first type. The coordination of the symmetry generated aluminium atom of the dimer results in a third group also comprising two independent Si–N bonds. They are the longest in **V** (1.7680(7) Å). However, the discrepancies between group two and three are quite small. A summary of all Si–N bond lengths in the three tetracoordinated silicon compounds is given in Table 5.1.

All N–Si–N angles in the dianion cluster around 111(2)°. Thus, they are in the range of those in the OMCTS. In contrast, the angles in the tetraanion are different (Table 5.2). They are all approximately 10° smaller (101(3)°). The deformation of the Si_4N_4 skeleton in **IV** effects the Si–N–Si bond angles only marginally. Like in OMCTS they are all in

the same range (132(3)°). Due to the more pronounced deformation of the crown in **V** the Si–N–Si angles of the two transannular nitrogen atoms pulled closely together are approximately 25° larger than those of the nitrogen atoms pushed apart.

Table 5.1 Si–N bond lengths [Å] in **III–V**.

	III	IV	V
Si1–N1	1.7273(3)	1.6844(7)	1.7668(6)
Si1–N2	1.7281(3)	-	-
Si1–N4	-	1.7565(9)	1.7028(5)
Si2–N1	1.7251(3)	1.6835(7)	1.7683(6)
Si2–N2	1.7221(3)	1.7437(9)	1.7015(5)
Si3–N2	-	1.7320(10)	1.7071(5)
Si3–N3	1.7205(3)	1.6821(8)	1.7445(7)
Si3–N4	1.7271(3)	-	-
Si4–N3	1.7286(3)	1.6798(7)	1.7410(6)
Si4–N4	1.7207(3)	1.7443(8)	1.1701(5)

Obviously, the varying nature and position of the metal cation above the silazane perimeter in **IV** and **V** is the key to the geometrical changes. Al^{3+} has a considerable smaller radius than Li^+ .¹¹³ The aluminium cation in **V** is coordinated by both nitrogen atoms, which are involved in the smaller transannular distance while the lithium cation coordinates the two nitrogen atoms with the larger distance. These bonding modes force the Si_4N_4 rings in the observed geometries. The tetrahedral coordination sphere of aluminium in **V** is completed by two additional bonds to nitrogen atoms, one to N3 of the same asymmetric unit, the other to N1 provides the dimeric link to the second heterocycle. The aluminium atom is not in the centre of the heterocycle, but shifted towards N3.

The Li cation (Li2) located above the eight-membered heterocycle in **IV** is not in the centre of gravity of this system either. The shift is perpendicular to the displacement of the metal cation in **V**. This shift of the side towards N4 leads to the formation of a long Li1–N4 bond. Due to the displacement of the Li cation, the Li2–N2 distance to the opposite nitrogen atom (2.89 Å) is too long to be regarded a bond. Together with a bond to N1 of the other moiety in the dimer, this leads to a distorted tetrahedral geometry at Li2 in **IV**, in contrast to Klingebiel et. al., who postulated only three bonds for the central lithium atom from their refinement.¹⁸

Table 5.2 N–Si–N and Si–N–Si angles [°] in **III–V**. The N–Si–N angles are averaged for each compound. The given esds are calculated as upper limits. The symmetry operations to generate the atoms involved in the angles of OMCTS are: -x, +y, 0.5-z and -x, -y, -z.

Si–N–Si	III	IV	V
Si1–N1–Si2	131.59(2)	130.13(4)	117.77(3)
Si1A–N2–Si2	134.32(2)	-	-
Si2–N2–Si3	-	131.32(6)	144.28(2)
Si3–N3–Si4	130.91(2)	135.29(4)	122.32(4)
Si4–N4–Si1	-	129.62(6)	146.86(4)
Si3A–N4–Si4	130.48(2)	-	-
N–Si–N(av.)	111(2)	111(2)	101(3°)

The Li–N bond lengths of the central Li cation in **IV** differ. Beside the longest, Li2–N4, the two Li–N bonds to the deprotonated nitrogen atoms are almost equal in length (2.1531(110)Å). These bond lengths are the result of a compromise – the possibility to form three bonds in an apical position of the Si₄N₄ ring, together with the fourth bond to the symmetry related nitrogen atom (Li2–N1A) of the second Si₄N₄ heterocycle which is with 2.0999(3)Å the shortest. As pointed out above, the Al cation in **V** is not located in the middle of the ring system, either. The shift towards one nitrogen atom causes different bond lengths. As for Li2, the bonds to the transannular nitrogen atoms are similar and the bond to the symmetry generated atom N1A is the shortest. Due to the competition of the additionally coordinated Li1 to N3, the Al–N3 bond is much longer. The smaller ionic radius of Al³⁺ leads in general to shorter Al–N bonds compared to Li–N bond distances. An overview of all metal–non-metal bond lengths is given in Table 5.3.¹¹⁴

An additional Li atom, termed Li1 in both molecules, is bonded to one nitrogen atom of the heterocycle. The peripheral coordination site of Li1 in **IV** and **V** is occupied by two THF ligands. These coordinated solvent molecules are disordered in **IV**. The disorder was refined to a split occupancy of 60:40 for one and 50:50 for the other THF, including bond lengths and similarity restraints in the refinement. The four different Li1–O bonds in **IV** and **V** assign marginally shorter bond lengths than the two Li1–N bonds. Again, this phenomenon can be mainly attributed to the smaller radius of oxygen atom.

Table 5.3 Non-metal–metal bond lengths [Å] in **IV** and **V**. The symmetry operations to generate the atoms involved in the bonds are: -x, -y, -z in **IV** and -x, -y, -z in **V**.

	IV	V
<u>Li–N</u>		
Li1–N3	1.9446(13)	1.9296(10)
Li2–N1	2.1417(12)	-
Li2–N1A	2.0999(11)	-
Li2–N3	2.1629(12)	-
Li2–N4	2.3923(13)	-
<u>Li–O</u>		
Li1–O1	1.9413(11)	1.8906(13)
Li1–O2	1.9137(11)	1.9110(13)
<u>Al–N</u>		
Al1–N1A	-	1.8575(6)
Al–N21	-	1.8842(6)
Al1–N3	-	2.0144(6)
Al1–N4	-	1.8873(5)

A distinct influence of the deprotonation on the highly polar Si–N bonds is observed. The effect on the neighbouring Si–C bonds turns out to be marginal. However, a conclusion based merely on bond lengths is difficult, because it seems impossible to deconvolute the deprotonation effect from the coordination to various metals. Some Si–N bonds including deprotonated nitrogen atoms are shorter than the protonated, others are longer. The longest Si–N bonds in compounds with a Si₄N₄ cycle are reported for compounds with one hydrogen atom replaced by an electropositive group E'–R (E' = P, Si).¹¹⁵ As well as the angles, these distances are also related to the number and type of the coordinated metal cation. The discrepancy between the short formal Si–N[–] and the longer Si–N(H) bonds compared to 1.7250(46) Å in **III** is most pronounced in the structure of the dianion. While small cations preferably form contacts to the centers of highest negative charge, the larger and 'softer' cations are less charge-localizing and hence coordinate to less negatively charged positions of the anionic fragment, as well. As a result, the hard cation Li⁺ forms shorter bonds to the two deprotonated nitrogen atoms in **IV**. Only one of the N(H) functionals is attractive for the Li cation in a donor-bond with a bond length at the long end of the range for Li–E contacts. In **V**, all nitrogen atoms are deprotonated and they all participate in at least one bond to a hard

metal cation. From traditional chemical concepts one would expect bond shortening due to increasing ionicity for all Si–N bonds in **V**. However, the Si–N bonds in this molecule, all including a deprotonated nitrogen atom, are elongated compared to **III**, where all nitrogen atoms are protonated. Besides, the sum of all Si–N bonds in OMCTS is 13.8005 Å, the sum is reduced to 13.7071 Å in the dianion, after deprotonation of two nitrogen atoms. Following this trend, deprotonation of all nitrogen atoms should result in a even lower sum. However, the sum increases to 13.8441 Å in the tetraanion. All these findings give rise to some discussion to which extend deprotonation and metal-lation necessarily leads to higher electrostatic forces and consequently to shorter bond lengths.

Thus, a more comprehensive inspection, provided from topological analyses subsequent to multipole refinements, should lead to a better understanding of the changes in the Si–N bonds caused by deprotonation and metal coordination. The electronic situation in metal–non-metal bonds is studied in detail at the end of the next chapter.

5.2.1.2 Multipole Refinement

Starting models for the multipole refinements of all three compounds enclosing tetracoordinated silicon atoms were derived from an IAM refinement as described in chapter 3.3.1. Disordered parts were refined using bond lengths and similarity constraints. The hydrogen atoms of the N–H moieties were located by difference Fourier syntheses. Details of the multipole refinements, local symmetry restrictions and similarity constraints are listed below:

OMCTS (**III**)

The populations of the silicon atoms were refined to fourth order (hexadecapolar level), the multipoles of all other non-hydrogen atoms to third order (octapolar level). For the hydrogen atoms a bond-directed dipole and quadrupole population was refined. Expansion/contraction factors (κ and κ') were introduced and adjusted for each atom type. For the hydrogen atoms two different sets were introduced – one set for the hydrogen atoms of the methyl groups, the second for hydrogen atoms bonded to a nitrogen atom. Charge transfer between the two moieties of the asymmetric unit was not allowed. Reflections to $\sin\theta/\lambda_{\max} = 1.10\text{Å}^{-1}$ with $I > 2(\sigma)I$ were included in the refinement following the standard procedure already described in chapter 3.3.2.

local symmetry:

- mirror planes, defined as the plane through the Si atom and two adjacent N atoms, for each silicon atom
- three-fold axis along C–Si bonds for all methyl groups

similarity constraints:

- carbon atoms at each silicon atom
- hydrogen atoms in the methyl groups of each molecule

Dianion (IV)

The populations of the silicon and the oxygen atoms were refined to the hexadecapolar level, the multipoles of all other non-hydrogen atoms to the octapolar level. For the N–H hydrogen atoms a bond-directed dipole and quadrupole population, for all others solely a bond-directed dipole population was refined. The lithium atom was treated spherically.¹¹⁶ Radial screening factors (κ and κ') were introduced and adjusted for each atom type. Two different sets were introduced for chemically different carbon atoms (C atoms bonded to Si and C atoms in THF, respectively) and hydrogen atoms (N–H and C–H), respectively. Due to the disorder the radial screening factors of the atoms in the THF moiety were kept fixed at recommended values.⁸⁴ Reflections to $\sin\theta/\lambda_{\max} = 1.05\text{\AA}^{-1}$ with $I > 2(\sigma)I$ were included in the refinement. Again, the refinement proceeded along the line described in chapter 3.3.2.

The disordered THF donor-bases were treated with special care. Several models have been tested. In the finally applied model, only two of the five non-hydrogen atoms in each disordered THF were refined at different positions. However, to match the individual orientation of the multipoles in each atom, it is necessary to introduce an atom with identical position for each atom of the other three non-hydrogen atoms in the disordered THF molecules (Figure 5.3). This procedure results in ten non-hydrogen atoms building two five-membered rings including three atoms with identical and two atoms with different positions with the oxygen atom as the pivot-atom to mimic the twist in the disordered THF molecules.

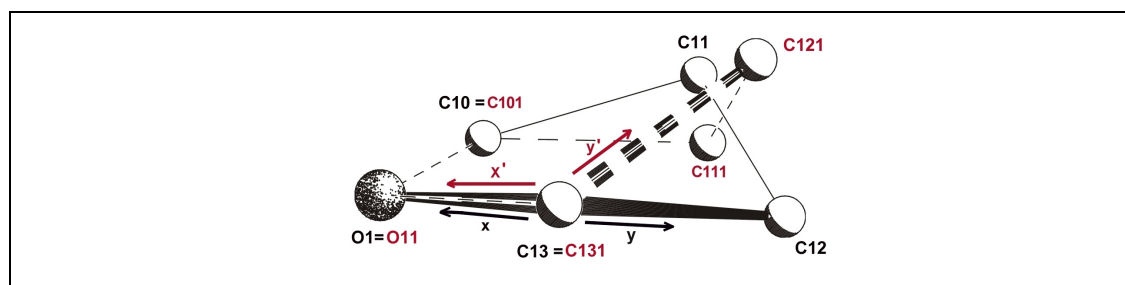


Figure 5.3 The position of atom C13 is not disordered in this THF moiety of the dianion, **IV**. However, the different orientation of the multipoles, described *via* a local coordinate system, to the disordered neighbouring positions C12 and C121 has to be defined.. Therefore, atom C131 is introduced on exactly the same position as C13, but with another orientation of the local coordinate system (x, y for C13 and x', y' for C131). This procedure fixes the orientation of the multipoles of C13 towards C12 and those of C131 towards C121, respectively.

The same procedure was applied to the hydrogen atoms in the THF molecule. Any of the THF moieties was defined as a group. The atomic coordinates of atoms belonging to the donor-base were kept fixed at x, y, z values from the high-order refinement with the IAM model in a lack of sufficient constraints in the XD least-squares procedure. In addition, each THF molecule was restricted to librate as rigid body. U_{ij} of atoms with identical positions were constrained to be equal. With respect to the split occupancies processed in SHELXL the multipole populations of the disordered THF molecules were constraint in the following manner: the refined multipoles of O11, C101, C111, C121 and C131 were constraint to have 0.66 times the populations of O1, C10, C11, C12 and C13, those of O21, C201, C211, C221 and C231 to be equal to O2, C20, C21, C22 and C23, respectively. The same restrictions were applied to the hydrogen atoms of the THF donor-bases.

The following symmetry and similarity constraints were applied in the refinement of **IV**:

- local symmetry:*
- mirror planes for each silicon atom, defined as the plane through the silicon atom and two adjacent nitrogen atoms,
 - three-fold axis along the C–Si bonds for all carbon atoms,
 - mirror planes for each carbon atom of the THF moieties, defined as the plane through the carbon atom and the two adjacent non-hydrogen atoms.
- similarity constraints:*
- silicon atoms with similar environment ($Si2 = Si1$ and $Si3 = Si4$),
 - methyl carbon atoms located above the Si_4N_4 heterocycle towards the metals,
 - methyl carbon atoms located below the Si_4N_4 heterocycle pointing to the outside of the molecule,
 - hydrogen atoms in all methyl groups,
 - hydrogen atoms of each THF moiety.

Tetraanion (V)

The populations of the silicon, aluminium and oxygen atoms were refined to the hexadecapolar level, the multipoles of the nitrogen and carbon atoms to the octapolar level. For all hydrogen atoms a bond-directed dipole population was included in the

refinement. The lithium atom was treated spherically. Expansion/contraction factors (κ and κ') were introduced and adjusted for each atom type. Two different sets were refined for chemically different carbon atoms (silicon bonded and carbon atoms in the THF donor-bases). The refinement of an anharmonic model for all third-row atoms lead to a significant improvement of the multipole model. Therefore an anharmonic motion approach by a Graham-Charlier expansion⁴¹ was employed in the refinement, although the complexity of the model increases drastically (125 additional parameters). The whole molecule apart from the two THF molecules and the lithium atom was defined as rigid body. Reflections to $\sin\theta/\lambda_{\max} = 1.05\text{\AA}^{-1}$ with $I > 2(\sigma)I$ were included in the refinement.

The residual densities close to one THF molecule reveal a slight disorder of at least one carbon atom (C13). Nevertheless, the multipole refinement does not account for this disorder because refinement of models which resolve the disorder lead to a flat residual map but did neither result in reliable bonding properties in the disordered area nor affect the topological properties of the bonds in the other parts of the molecule.

- local symmetry:*
- mirror planes for each silicon atom, defined as the plane through the silicon atom and two adjacent nitrogen atoms,
 - three-fold axis along the C–Si bonds for all carbon atoms,
 - mirror planes for each carbon atom of the THF moieties, defined as the plane through the carbon atom and the two adjacent non-hydrogen atoms.
- similarity constraints:*
- silicon atoms with similar environment (Si2 = Si1 and Si3 = Si4),
 - nitrogen atoms with similar equivalent environment (N4 = N2),
 - methyl carbon atoms located above the Si₄N₄ heterocycle towards the metals,
 - methyl carbon atoms located below the Si₄N₄ heterocycle pointing to the outside of the molecule,
 - hydrogen atoms in all methyl groups,
 - hydrogen atoms of THF moieties.

The residual maps after the multipole refinement are featureless (Figure 5.4 and Figure 5.5) with the exception of the one around C13 in one THF molecule of **V** (Figure 5.5 (f)). The disorder causing this significant density was already mentioned. The Hirshfeld DMSDA test for **III** shows, that the differences in the mean-square displacement amplitudes do not exceed $0.4 \cdot 10^{-3} \text{Å}^2$ in the Si_4N_4 heterocycle. The DMSDAs of the Si–C bonds are between $1.3 \cdot 10^{-3} \text{Å}^2$ and $1.5 \cdot 10^{-3} \text{Å}^2$ because of the mass differences and the Si atoms being relatively fixed in the heterocycle while the carbon atoms are bonded as terminal groups.

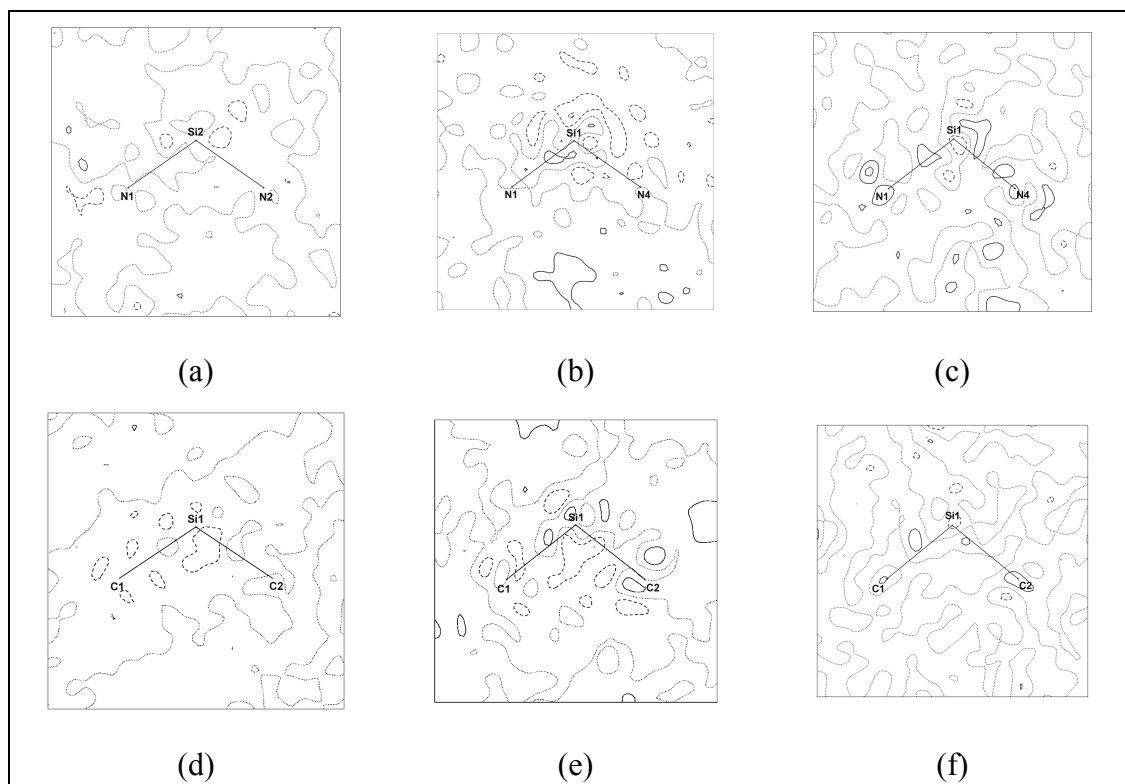


Figure 5.4 Contour plots of the residual densities after multipole refinement in N–Si–N and C–Si–C planes of **III–V**, $\sin\theta/\lambda_{\max} = 1.00 \text{Å}^{-1}$. (a) N1–N2–Si2 plane in **III**, (b) N1–Si1–N4 plane in **IV**, (c) N1–Si1–N4 plane in **V**; (d)–(f) C1–Si1–C2 plane in **III** (d), **IV** (e) and **V** (f). Positive densities depicted as solid contours, zero-level as dotted, negative density as dashed contour line; tepwidth is 0.1eÅ^{-3} .

The DMSDAs in **IV** show the same trend. The maximum value for the eight-membered heterocycle is $1.0 \cdot 10^{-3} \text{Å}^2$. The Si–C bonds again exceed this value ($1.2 \cdot 10^{-3} \text{Å}^2$ - $2.5 \cdot 10^{-3} \text{Å}^2$). The influence of the mass differences and the (more or less fixed) position in the molecule is evident from the DMSDAs for the Li–E (E = N, O) bonds. They cluster around $1.0 \cdot 10^{-3} \text{Å}^2$ ($0.3 \cdot 10^{-3} \text{Å}^2$ - $1.5 \cdot 10^{-3} \text{Å}^2$) for Li2, which is rather fixed in the centre of the molecule, and $2.0 \cdot 10^{-3} \text{Å}^2$ ($0.9 \cdot 10^{-3} \text{Å}^2$ - $4.2 \cdot 10^{-3} \text{Å}^2$) for Li1, located in the periphery and bonded to two coordinated solvent molecules. Several DMSDAs for the

two disordered THF molecules can not stand the DMSDA test. The differences of the amplitudes are between $0.1 \cdot 10^{-3} \text{Å}^2$ and $3.7 \cdot 10^{-3} \text{Å}^2$ indicating bias caused by indeterminable valence densities or an inappropriate description of the disorder.

The rigid-bond test of **V** reveals very small DMSDAs. It is adequate for almost all bonds of the compound but those containing lithium. Due to mass differences the DMSDAs for the latter bonds are in the range of $2.5 \cdot 10^{-3} \text{Å}^2$ - $5.6 \cdot 10^{-3} \text{Å}^2$. The maximum amplitude for all other bonds is $1.1 \cdot 10^{-3} \text{Å}^2$ with only one exception for a bond (C10–C11) in a THF moiety ($2.0 \cdot 10^{-3} \text{Å}^2$).

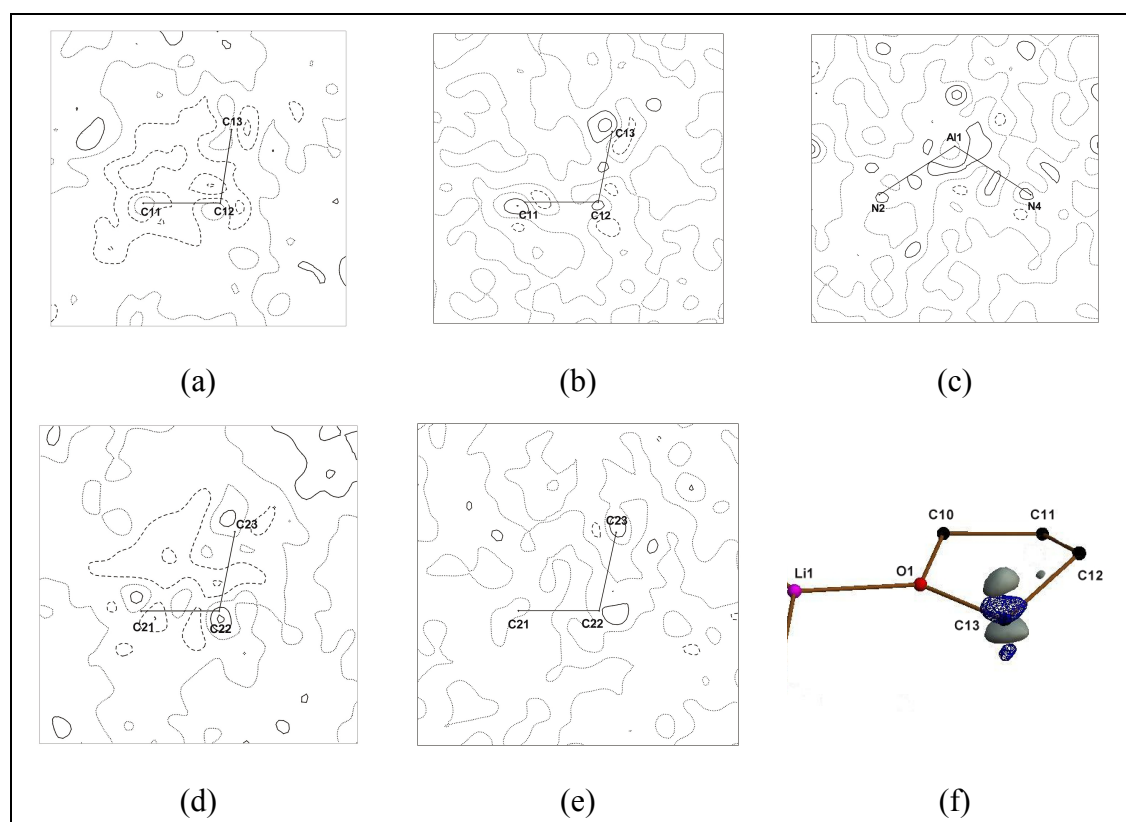


Figure 5.5 (a)–(e) Contour plots of the residual densities after multipole refinement in the planes of the THF moieties in **IV**, **V** and in a plane containing the aluminium atom in **V**, $\sin\theta/\lambda_{\max}=1.00 \text{Å}^{-1}$. (a), (b) C11–C12–C13 plane in **IV** (a) and **V** (b), (c) N2–Al1–N4 plane in **V**; (d), (e) C21–C22–C23 plane in **IV** (d) and **V** (e). Positive densities depicted as solid contours, zero-level as dotted, negative density as dashed contour line; stepwidth is 0.1eÅ^{-3} . (f) Isosurface representation of the residual density around C13 in **V**; isosurface is drawn at the $+0.20 \text{eÅ}^{-3}$ (gray) and the -0.20eÅ^{-3} (blue) level, respectively.

Meaningful improvements in the R-values underline the quality of the multipole refinements; the aspherical densities around the third-row atoms are properly described with the applied models. Values clustering around two for the Gof are again merely caused from the statistical weighting scheme. The results of the multipole refinements revealed, that it is absolutely vital to have different tests to ascertain the improvement in

the reliability of a refinement. The DMSDA test may show significant bias like in **IV**, but the residual maps are ‘flat’. In **V** the residuals around C13 are not neglectable, while the DMSDA test shows no signs for disorder. More crystallographic details are listed in Table 5.5.

The conclusion from the refinement of the disordered THF molecules is less optimistic for future work. It seems to be possible to refine the densities to a featureless residual map, but taking all tests for an accurate refinement into account one gets the impression, that it is adequate to exclude the periphery (e. g. coordinated disordered solvent molecules) during future multipole refinements since the minor effect on central bonds. Within a refinement using the IAM for the THF moieties, the amount of electron density $\rho(\mathbf{r}_{\text{BCP}})$ of the bonds in the Si₄N₄ heterocycle is not affected at all, the consequences for the Laplacian, a rapidly changing function, are denoted in Table 5.4. However, a variation of about 1.5eÅ⁻⁵ for $\nabla^2\rho(\mathbf{r}_{\text{BCP}})$ is not regarded a drastic change.¹¹⁷ The variation in $\nabla^2\rho(\mathbf{r}_{\text{BCP}})$ due to the change of the model is rather small compared to the high esds; the effect on the R-value may be even higher. Most likely, the origin of the problems is the rotation around single bonds, that causes a conformational variance.

Table 5.4 Averaged topological properties of the Si–N and Si–C bonds in **IV** at the BCP including a refinement of the disordered area (**incl**) or excluding this area during the refinement (**excl**). $\rho(\mathbf{r}_{\text{BCP}})$ is given in eÅ⁻³, $\nabla^2\rho(\mathbf{r}_{\text{BCP}})$ in eÅ⁻⁵, respectively.

	Si–N		Si–C	
	$\rho(\mathbf{r}_{\text{BCP}})$	$\nabla^2\rho(\mathbf{r}_{\text{BCP}})$	$\rho(\mathbf{r}_{\text{BCP}})$	$\nabla^2\rho(\mathbf{r}_{\text{BCP}})$
incl	1.033(119)	8.305(842)	0.796(24)	4.037(199)
excl	1.055(108)	6.450(1.122)	0.804(21)	3.473(153)

Therefore, the constraints, determining the multipole populations of the second group, are not ideally suited for the description of a second moiety with an at least slightly different conformation. Nevertheless, the IAM refinement clearly reveals the disorder and the test described above shows no bias to be introduced. Hence, the results of the multipole refinement including the disordered area are used for the analysis of the electronic properties of this sample.

Table 5.5 Crystallographic data from the multipole refinement of **III-V**.

compound	III	IV	V
formula	C ₂₈ H ₂₈ N ₄ Si ₄	C ₁₆ H ₄₂ Li ₂ N ₄ O ₂ Si ₄	C ₁₆ H ₄₀ AlLiN ₄ O ₂ Si ₄
crystal system	monoclinic	triclinic	monoclinic
space group	P2/c	P $\bar{1}$	P2 ₁ /c
a [Å]	11.5216(3)	10.8335(4)	11.3016(4)
b [Å]	6.3499(2)	11.1146(4)	14.0556(5)
c [Å]	22.6282(7)	12.3563(4)	16.6748(6)
α [°]	90	79.0270(1)	90
β [°]	90.474(1)	64.1950(1)	107.354(1)
γ [°]	90	81.7730(1)	90
V [Å ³], Z	1655.45(8), 4	1311.91(8), 2	2528.23(16), 4
μ [mm ⁻¹]	0.35	0.24	0.29
T _{min} / T _{max} (low-angle batch)	0.89 / 0.97	0.85 / 0.98	0.87 / 0.98
T _{min} / T _{max} (high-angle batch)	0.92 / 0.96	0.87 / 0.96	0.92 / 0.99
refl. used in the multipole refinement after cut-off *	15988	18712	18351
sin θ / $\lambda_{\text{max, cut}}$ [Å ⁻¹]	1.10	1.05	1.05
completeness to sin θ / $\lambda_{\text{max, cut}}$ [%]	98.4	98.2	98.9
no. of unique reflections (low-angle batch) / R _{int}	3707 0.0340	5368 0.0427	5182 0.0393
no. of unique reflections (high-angle batch) / R _{int}	17713 0.0292	26352 0.0476	26259 0.0544
limiting indices	-26 ≤ h ≤ 26, 0 ≤ k ≤ 14, 0 ≤ l ≤ 51	-21 ≤ h ≤ 24, -24 ≤ k ≤ 24, 0 ≤ l ≤ 27	-25 ≤ h ≤ 24, 0 ≤ k ≤ 32, 0 ≤ l ≤ 38
max. shift / esd in final cycle	0.66 · 10 ⁻⁷	0.39 · 10 ⁻²	0.51 · 10 ⁻²
R1 (I > 2σ(I)) after IAM refinement to sin θ / $\lambda_{\text{max, cut}}$	0.0235	0.0477	0.0404
wR2 (I > 2σ(I)) after IAM refinement to sin θ / $\lambda_{\text{max, cut}}$	0.0777	0.1403	0.0973
R1 (I > 2σ(I)) after multipole refinement to sin θ / $\lambda_{\text{max, cut}}$	0.0188	0.0470	0.0320
wR2 (I > 2σ(I)) after multipole refinement to sin θ / $\lambda_{\text{max, cut}}$	0.0279	0.0551	0.0341
GoF	2.16	5.03**	2.70
N _{refl.} / N _{param.}	51.08	39.15	34.56

* with respect to these cut off criteria: sin θ / λ_{max} and I > 2σ(I)** indicates that the 1/σ² weight is less appropriate than in the other samples; however, the weighting scheme was not adjusted for comparison purposes with compounds **III** and **V**.

5.2.1.3 Topological Analysis

The topology of the Si–N bonds is in the centre of interest in this chapter. The topological analysis after the multipole refinement illuminates the differences in this bond type far beyond merely bond lengths and angles comparison. To the best of our knowledge, neither theoretical, nor experimental studies of this bond type on tetracoordinated organosilicon compounds in terms of Bader's AIM theory are present in literature; charge density studies on tetracoordinated silicon compounds are mainly focused on silicates.¹¹⁸

The Si–C bonds are less affected by the changes at the nitrogen atom. The function of the Laplacian has a low positive value at all Si–C bonds. The topological properties are in good agreement with results of combined theoretical and experimental charge density studies on Si–C bonds published by Scherer et. al.³⁵

Table 5.6 gives a compilation of the topological properties of all Si–N bonds in **III-V** and reveals significant differences at the BCP. Unfortunately, the picture drawn from these values is rather heterogeneous. All BCPs are shifted closer to the electropositive silicon atom. However, it seems impossible to deduce the degree of polarity.

Table 5.6 Topological properties of the Si–N and Si–C bonds in **III-V** at the BCP. Values for the latter are averaged. The given esds are calculated as upper limits.

A–B	compound	d(A–B)	d(A–BCP)	d(BCP–B)	$\rho(\mathbf{r}_{\text{BCP}})$	$\nabla^2\rho(\mathbf{r}_{\text{BCP}})$
<u>Si–N</u>	III					
Si1–N1		1.7274	0.7278	0.9996	0.974(9)	8.681(21)
Si1–N2A		1.7284	0.7272	1.0012	0.978(13)	8.871(22)
Si2–N1		1.7252	0.7319	0.9933	1.002(9)	7.645(22)
Si2–N2		1.7222	0.7266	0.9956	1.004(10)	8.216(22)
Si3–N3		1.7205	0.7192	1.0013	0.940(9)	11.143(22)
Si3–N4A		1.7272	0.7283	0.9989	0.969(13)	8.716(22)
Si4–N3		1.7286	0.7282	1.0004	0.985(9)	8.364(22)
		1.7210	0.7279	0.9931	1.018(9)	7.774(22)
<u>Si–C (av.)</u>		1.8665(25)	1.0923(54)	0.7736(29)	0.864(17)	2.114(729)

<u>Si-N</u>	IV				
Si1-N1	1.6845	0.7439	0.9407	1.121(13)	7.953(25)
Si1-N4	1.7567	0.7546	1.0022	0.914(12)	8.422(27)
Si2-N1	1.6837	0.7385	0.9452	1.147(8)	8.256(7)
Si2-N2	1.7438	0.7535	0.9903	0.920(9)	8.456(7)
Si3-N2	1.7320	0.7540	0.9780	0.967(9)	7.841(8)
Si3-N3	1.6821	0.7319	0.9502	1.140(8)	9.146(7)
Si4-N3	1.6799	0.7379	0.9420	1.110(13)	8.609(26)
Si4-N4	1.7444	0.7565	0.9879	0.954(12)	7.744(27)
<u>Si-C (av.)</u>	1.8792(121)	1.0864(71)	0.7928(49)	0.797(15)	4.037(200)

<u>Si-N</u>	V				
Si1-N1	1.7672	0.7409	1.0264	0.961(8)	5.909(17)
Si1-N4	1.7030	0.7185	0.9845	0.938(10)	11.446(18)
Si2-N1	1.7687	0.7470	1.0217	0.939(6)	5.339(3)
Si2-N2	1.7016	0.7184	0.9832	0.936(5)	11.439(3)
Si3-N2	1.7074	0.7201	0.9873	0.914(6)	11.817(4)
Si3-N3	1.7447	0.7349	1.0097	0.992(6)	6.959(4)
Si4-N3	1.7411	0.7387	1.0024	0.979(9)	6.444(17)
Si4-N4	1.7104	0.7209	0.9895	0.907(11)	11.733(19)
<u>Si-C (av.)</u>	1.8775(62)	1.1005(42)	0.7770(46)	0.0.866(22)	1.853(206)

$d(A-B)$ is the bond path length between the atoms A and B [\AA], $d(A-BCP)$ and $d(B-BCP)$ denote the distances of the atoms A and B from the BCP [\AA], $\rho(\mathbf{r}_{BCP})$ [$\text{e}\text{\AA}^{-3}$] is the charge density and $\nabla^2\rho(\mathbf{r}_{BCP})$ [$\text{e}\text{\AA}^{-3}$] the Laplacian at the BCP, respectively.

The ratio of the eigenvalues $|\lambda_1|/\lambda_3$ at the BCP is significantly below 1 for highly polar bonds. For the Si-N bonds the ratio is between 0.23 and 0.31, indicating dominant ionic contribution. These ratios for the Si-C bonds in **III-V** cluster around 0.38. Changes in λ_1 , the maximum charge concentration perpendicular to the bonding vector, are only very small ($\lambda_1 \approx 4(1)\text{e}\text{\AA}^{-5}$) with regard to all Si-N bonds. In contrast, λ_3 , the indicator for charge concentration along the bond, undergoes distinct changes ($\lambda_3 \approx 18(4)\text{e}\text{\AA}^{-5}$). The Si-N bonds of **IV** and **V** are all in the same range with the lowest ratio calculated for bonds in **V**.

The average electron density at the BCP for the Si-N bonds in OMCTS is $0.984(43)\text{e}\text{\AA}^{-3}$. For Si-N bonds containing a deprotonated nitrogen atom, one would expect a lower density because of the increased polarization, following the argumentation of the structure discussion in the previous chapter. This is true for the

tetraanion. All bonds of this type exhibit a lower electron density at the BCP. Surprisingly, in the dianion, the bonds of the deprotonated nitrogen atoms show on average a $0.18\text{e}\text{\AA}^{-3}$ higher density at the BCP compared to the Si–N(H) bonds.

Inspection of the Laplacian of $\rho(\mathbf{r})$ at the BCP contributes not much to clarify the situation. The Si–N bonds of **III** have an average value of $8.324(679)\text{e}\text{\AA}^{-5}$. In **IV**, the averaged Laplacian at this point is $8.066(356)\text{e}\text{\AA}^{-5}$ for the Si–N(H) and only slightly more positive ($8.491(655)\text{e}\text{\AA}^{-5}$) for the Si–N bonds, respectively. The highest variation of the Laplacian at the BCP is found in **V**, but without an obvious trend. While some of the Si–N bonds reveal a higher value of $\nabla^2\rho(\mathbf{r})$, others are below the average value of **III**. The three chemically different types cover the range from $5.624(285)\text{e}\text{\AA}^{-5}$ to $11.609(208)\text{e}\text{\AA}^{-5}$ (averaged values for each type).

As shown in the diagrams of Figure 5.6 the Laplacian and the total electron density at the BCP of the Si–N bonds are related closer to changes in the bond length than to changes in the topology.

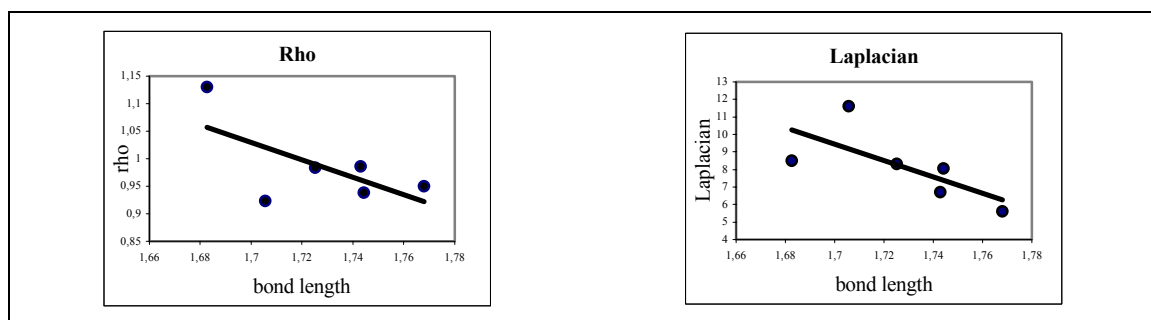


Figure 5.6 Diagrams of the total electron density $\rho(\mathbf{r})$ [$\text{e}\text{\AA}^{-3}$] and the Laplacian $\nabla^2\rho(\mathbf{r})$ [$\text{e}\text{\AA}^{-5}$] at the BCP of the Si–N bonds as a function of the bond length [Å].

However, as already pointed out at various occasions, monitoring the entire bonding region is necessary to get a reliable rather than a punctual impression and to manifest variations of the electronic situation in highly polar bonds.⁶⁶ The most sensitive tool to elucidate differences is the Laplacian. First of all, all Si–N bonds in **III-V** show the typical distribution for polar bonds. Charge is depleted in the whole basin of the electropositive atom, i. e. the silicon atom, the Laplacian is positive at the BCP and the charge is concentrated in the basin of the electronegative atom, i. e. the nitrogen atom. After a closer inspection some differences between the Si–N bonds can be extracted from the distribution along the bond paths (Figure 5.7).

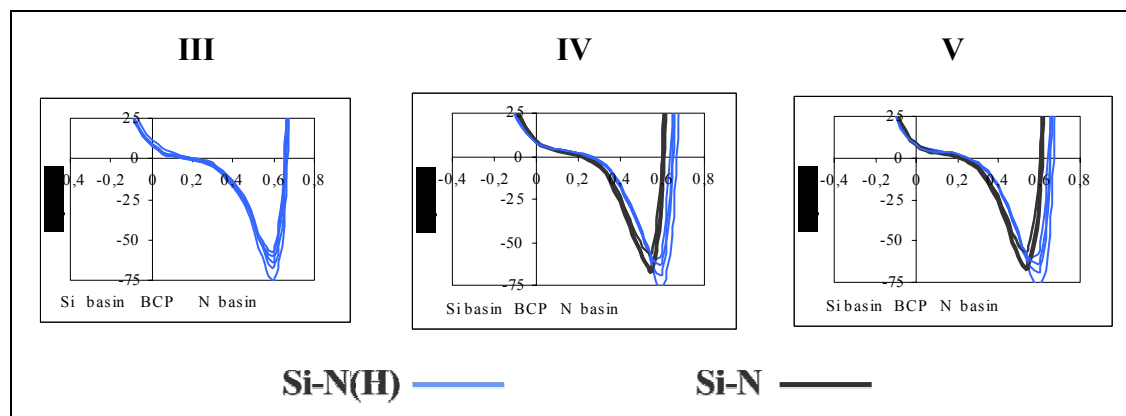


Figure 5.7 Laplacian [$\text{e}\text{\AA}^{-5}$] along the Si-N bond paths [\AA] of **III-V**. The zero value of the x-axis indicates the position of the BCP

The charge depletion in the bonding region of the Si-N bond paths in all Si basins is almost identical. Only for two bonds of **V** the depletion is slightly more pronounced. In OMCTS (**III**), with four Si-N(H) moieties, all Si-N bonds reveal an almost identical distribution of the Laplacian of $\rho(\mathbf{r})$ along the bond path and in the nitrogen basin. The averaged maximum charge concentration along the Si-N path in this basin is $-63.7\text{e}\text{\AA}^{-5}$ with a distance of 0.60\AA to the BCP. In the dianion (**IV**), the Laplacian elucidates two different types of Si-N bonds. The first type includes all Si-N(H) bonds. The averaged maximum charge concentration for these bonds is $-67.5\text{e}\text{\AA}^{-5}$, while the distance to the BCP in the nitrogen basin is now 0.58\AA . It seems, that the weak interaction of N4 and Li2, with $\rho(\mathbf{r}) = 0.086\text{e}\text{\AA}^{-3}$ at the BCP, does not significantly influence the Si-N bond because the topological properties do not differ from those of N2, not coordinated to a lithium cation. All bonds enclosing a deprotonated nitrogen atom belong to the second type of Si-N bonds in **IV**. Their averaged maximum charge concentration in the basin of the nitrogen atom is shifted closer to the BCP ($d = 0.55\text{\AA}$) and the quantity has decreased to $-61\text{e}\text{\AA}^{-5}$. Thus, the protonated nitrogen atoms exhibit a higher charge concentration in the bonding region of the nitrogen basin than the deprotonated atoms. Compared to **III**, the maximum concentration increased in the Si-N(H) of **IV**, while it decreased in the bonds to deprotonated nitrogen atoms.

In the third sample, **V**, the Laplacian distribution along all Si-N bond paths is similar again. All nitrogen atoms are deprotonated and, following the trend of **IV**, the averaged maximum charge concentration along the bond paths is below the value of **III**. Obviously, it is not straight forward to reveal the three different types distinguished from bond lengths considerations. But two slightly different types can still be identified. Again, the two transannular nitrogen atoms bonded to Al1 (N2, N4) form one type, with maximum charge concentrations approximately $2.5\text{e}\text{\AA}^{-5}$ higher compared to the others. The distances of these maxima of 0.58\AA to the BCP are about 2pm closer to the BCP

than the maxima of the second group which consists of two chemically different nitrogen atoms. In addition to the Si–N1 bonds this nitrogen atom is bonded to one aluminium cation, while N3 is bonded to one aluminium and one lithium cation. Despite this different environment, the Laplacian along these Si–N bonds does not display a distinct difference. In any case, the differences between the groups in **V** are much less pronounced than in **IV**.

In summary, the Laplacian along the bond paths reveals deviations between the Si–N(H) and the Si–N(Li; Al) bonds. Almost equal charge depletion in the Si basin and more distinct maxima in the bonding region of the protonated nitrogen basins are observed. This result is not in line with the formulation of a negatively charged N[−] and an increasing ionicity after the deprotonation as mentioned in the structure discussion to explain the changes in the bond lengths. It is more likely that the deprotonation of the Si–N(H) bonds is accompanied from other electronic effects.

Figure 5.8 shows the Laplacian distribution in N–Si–N and C–Si–C planes of **III**, **IV** and **V**. Obviously, charge is depleted in the entire Si basins. The charge concentrations can be exclusively assigned to the nitrogen and carbon basins. The deformations of the charge concentrations in the basins of the electronegative atoms are typical for highly polar bonds. The main difference between the Laplacian distribution in the Si–C and Si–N bonds is the more distinct deformed shape of the charge concentrations in the Si–C bond. The charge concentrations at the nitrogen atoms are also slightly deformed, but their shape is more atomic-like indicating higher ionicity of the Si–N bond compared to Si–C. The deviating electronic situations of the Li–N and Al–N bonds are visible in Figure 5.8 (b) and (c).

Obviously, the two-dimensional Laplacian distribution along the bond bath displays details in the entire bonding region, but close to the atomic position the charge concentrations and depletions are too extreme to be visualised with this tool. Two-dimensional representations with the spatial distribution of $\nabla^2\rho(\mathbf{r})$ are ideally suited for an inspection of the whole shape of the charge concentrations along a bonding vector, but they can not help either to analyze the details close to an atom. Hence, a third dimension is added to the Laplacian distribution and requires the inspection of the valence shell charge concentrations (VSCCs). This tool allows to localize and quantify bonded and non-bonded charge concentrations in a sphere with a radius of 0.2 – 0.5 Å around the position of the atomic core. Higher charge concentrations in the valence shell result in more prominent values for the Laplacian.

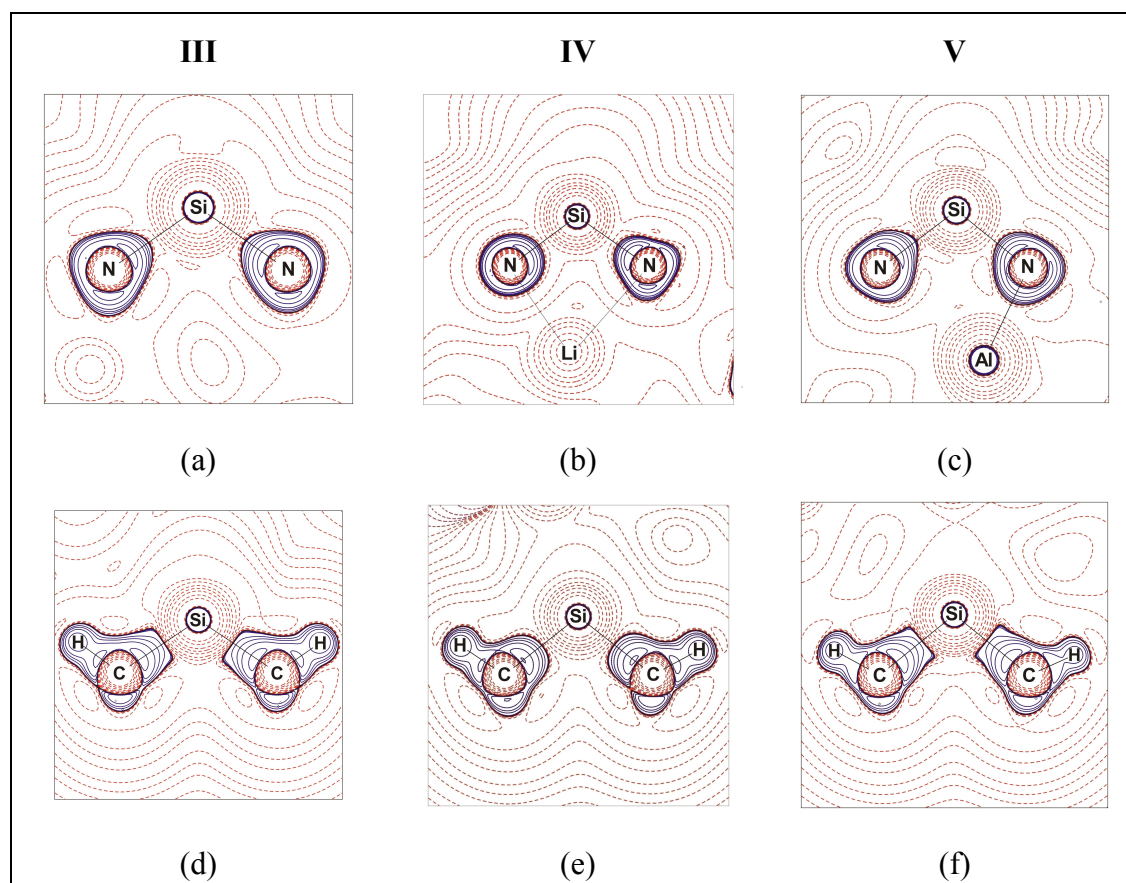


Figure 5.8 Contour plots of the Laplacian distribution in N-Si-N and C-Si-C planes of **III-V**. (a) N1-Si2-N2 plane in **III**, (b) N1-Si1-N4 plane in **IV** and (c) in **V**; (d)-(f) C1-Si1-C2 plane in **III** (d), **IV** (e) and **V** (f). Blue lines indicate charge concentration, red lines charge depletion. Contours drawn at $0.000, \pm 2.0 \cdot 10^n, \pm 4.0 \cdot 10^n, \pm 8.0 \cdot 10^n \text{ e}\text{\AA}^{-5}$, where $n = 0, -3, \pm 1, \pm 2$.

The magnitude of the VSCCs confirms the hints provided by the bond paths inspection. Slightly more prominent values were determined for the VSCCs around the protonated nitrogen atoms. The extensive searches in the spatial distributions of the Laplacian around the nitrogen atoms did not verify any maximum for a non-bonded lone-pair localized at any nitrogen atom. Neither non-bonding lone-pair VSCCs for the protonated nor for the deprotonated nitrogen atoms could be determined.

Three VSCCs, all exactly on the bonding vectors, were found at each nitrogen atom of OMCTS (**III**). The searches around the protonated nitrogen atoms in the dianion (**IV**) also resulted in three maxima at each nitrogen atom. However, not all the maxima were located exactly at the bonds, the maxima towards the lithium atoms are displaced from the direct line between the lithium and the nitrogen atom. In the tetraanion (**V**) three VSCCs around the nitrogen atoms bonded to one metal cation were verified and four at N3, bonded to two cations. Hence, a sp^3 hybridization state is only proved unambiguously for the latter nitrogen atom.

The angles between the VSCCs around the N atoms in **III** are almost ideal for a planar environment with slightly enlarged $\text{VSCC}_{\text{Si}}\text{--N--VSCC}_{\text{Si}}$ angles in any case. The sum of the angles always equals 360° . These facts strongly recommend sp^2 hybridization for the nitrogen atoms in OMCTS. But the Si–N bond lengths in this sample are close to those for an ideal single bond, and in addition, all bonds are equal in length. Additional properties listed below have to clarify this discrepancy. In the dianion (IV) the sum of the angles between the three VSCCs is always marginally less than 360° ($359.24 - 356.09^\circ$). The sum of the VSCC--N--VSCC angles around each N atom in **V** is different, much below the 360° of a planar environment. They cover a range from 345.08° to 354.31° , with less than 348° for three atoms (N2–N4). Although this indicates tetrahedral environment no non-bonded lone-pair VSCCs could be determined.

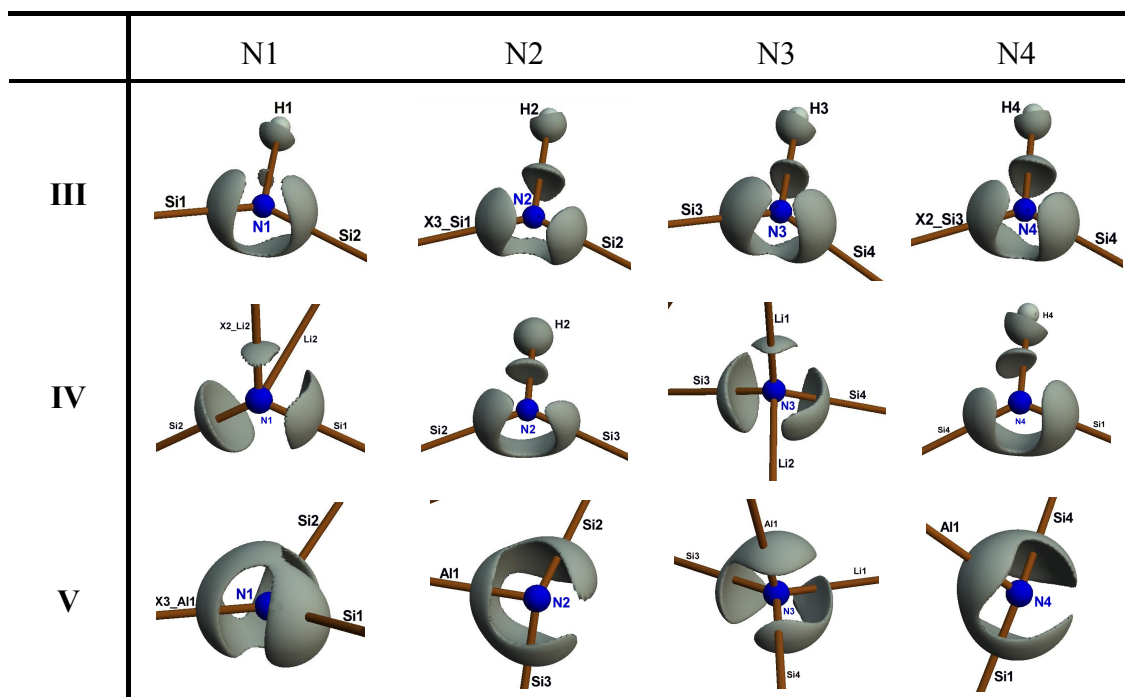


Figure 5.9 Isosurface representation at constant values of the Laplacian $\nabla^2\rho(\mathbf{r})$ around the nitrogen atoms of **III–V**, indicating bonding and non-bonding VSCCs. The isosurfaces are plotted at the following levels [$\text{e}\text{\AA}^{-5}$]; in **III**: N1: -42, N2: -40, N3: -38, N4: -38; in **IV**: N1: -43, N2: -47, N3: -43, N4: -41; in **V**: N1: -37, N2: -38, N3: -41, N4: -38.

A reason for the lack of an (3; -3)CP in $\nabla^2\rho(\mathbf{r})$ might be a diffuse distribution of the Laplacian with a flat maximum, which is hard to detect with numerical methods. In this case graphical inspection by isosurface plots is superior. From isosurface representations in Figure 5.9 for all nitrogen atoms in **III–V** it is clearly visible that no

distinct charge concentration is present in the expected lone-pair regions. Spectroscopic studies in the late 60s on $\text{N}(\text{SiMe}_3)_3$ already dealt with the properties of the nitrogen lone-pair in the SiN bond.¹¹⁹ In addition, it is evident, that the charge concentrations are rather distorted for most of the atoms. These findings fuel the idea of diffuse lone-pair densities which are to a large extent redistributed into the Si–N bonds. This kind of charge distribution was also observed by Scherer et al. in Si–C bonds after deprotonation of the carbon atom.³⁵ Within this study similar trends were found for the changes in the magnitudes of the VSCCs. After deprotonation of the carbon atom and a subsequent lithiation the values for the VSCCs at the carbon atom of the Si–C bond decreased. The same is valid for the Si–N bonds in the present samples. All deprotonated nitrogen atoms reveal lower maximum charge concentrations in the valence shell than the N(H) moieties. Furthermore this electronic situation is supported from the diffuse shapes of the Laplacian, especially in areas oriented towards the metal cations; even some VSCCs appear to merge (see Figure 5.9).

Obviously, shifts of lone-pair density into the Si–N bonding region result in relatively high values of the total electron density $\rho(\mathbf{r})$ at the bonding vector for highly polar bonds like Si–N bonds. The question arises whether this is applicable to the present situation. The clear answer is: yes, it is. The ration of $|\lambda_1|/\lambda_3$ in the Si–N bond is smaller, the Laplacian at the BCP is more positive, and the spatial distribution of the Laplacian around the nitrogen atoms is more atomic-like comparing the Si–N and Si–C bonds of the three samples. The total electron density $\rho(\mathbf{r})$, however, is on average more than 13% higher at the BCP of the Si–N bond, although diagnostic tools underline the higher ionicity of this bond type. This is caused from additional charge of the nitrogen lone-pairs.

Pioneering studies from Bader et. al.¹²⁰ related conjugative interactions to increasing ellipticity ε in a bond, thus establishing a direct link to the molecular charge density. The described transfer of lone-pair density should therefore lead to significant elliptisities in the nitrogen basins. For this purpose the bond ellipticity ε is introduced as a measure of electron transfer to the Si–N bond. When ε is traced along the full bond bath, it serves as a very sensitive criterion of distortion of the electron density from cylindrical σ symmetry. According to the mathematical definition (2.5.5) ε values grater than zero indicate partial π character in a bond or electronic distortion from σ symmetry along the bond path. The results of these inspections are presented in Figure 5.10.

While ε is close to zero in the silicon basins, it increases drastically towards the nitrogen basins of **III-V**. In **III**, the shape of ε along all Si–N bond paths is rather similar, with maxima in the range from 0.2 - 0.4 at equal distances from the BCP. Furthermore, the

curvature of ϵ in **III** shows a small but significant shoulder near the BCP. This shape is reproduced by inspection of the Si–N(H) bonds in **IV**, with a less distinct shoulder and a more narrow region of significant ellipticities. At this stage it is pertinent to point out that the very weak Li2–N4 contact shows the necessary conditions for a chemical bond in terms of Bader's AIM theory, but does not lead to different topological properties of N4 with respect to the other N(H) atoms. Therefore it is included in the argumentation of the other N(H) moieties. The deprotonated nitrogen atoms with contacts to lithium atoms display completely different distributions. The ellipticities of these bonds do not exceed 0.1, indicating much less distortion. In **V**, with N–Al contacts, all bonds show significant ellipticities again, but on average at a lower level than in **III**. The maxima cluster around 0.15. Line shape analysis for the curvatures of **V** can distinguish the different shapes of ϵ . Four distributions of ϵ in **V** depict a shoulder at the BCP. These curvatures belong to the Si–N bonds of the transannular nitrogen atoms N2 and N4 exclusively coordinated to the aluminium cation. This shoulder is not present in the other four Si–N bonds. The bond lengths of the former group are about 4 to 6 pm shorter than those of the latter.

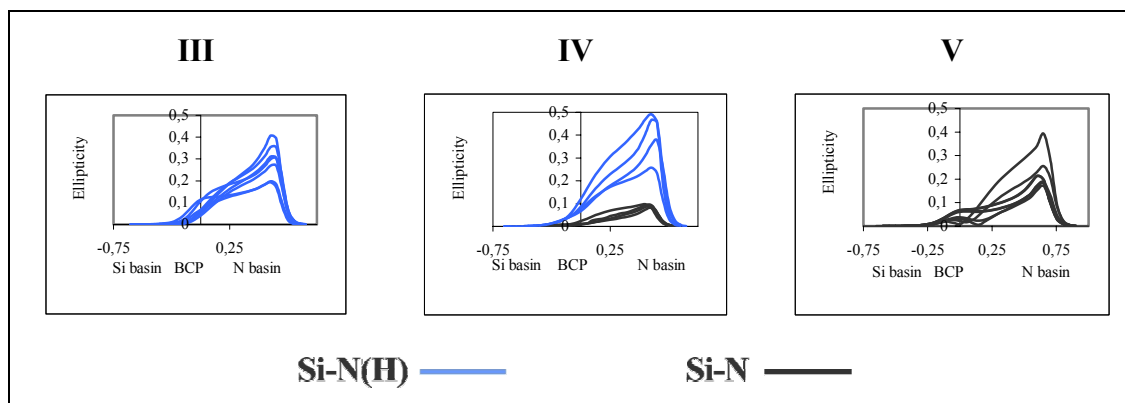


Figure 5.10 Ellipticities along the Si–N bond paths [Å] in **III–V**. The zero value of the x-axis indicates the position of the BCP

These findings make an important contribution to categorize the Si–N bonds in the studied compounds. A shoulder in the profile of ϵ indicates a certain degree of double bonding. In other words, they elucidate a small contribution of lone-pair back bonding in almost all Si–N bonds. Of course, this leads to shorter bonds. In OMCTS (**III**) the Si–N bond lengths are almost identical. Their average length, about 1.72 Å, is the result of remarkable charge transfer. In the dianion, the charge transfer contributes less to the Si–N(H) bonds, leading to a Si–N bond elongation of 3 pm. The Si–N bonds in this compound with deprotonated nitrogen atoms show no significant ellipticities. They are shortened to about 1.69 Å due to increased electrostatic interaction after the

deprotonation. The situation in the tetraanion is different. The Si–N bonds show significant ellipticities, again indicating redistribution of charge in all bonds, but more pronounced in bonds with a shoulder in the ellipticity profile. They display bond lengths shortened by 4 to 6 pm compared to those without such a characteristic feature.

Another important value that shows changes of the nitrogen atoms on metallation is the integrated charge (Table 5.7). A nitrogen atom bound to electropositive atoms is expected to adopt a negative charge even in OMCTS. After deprotonation and formation of bonds to one or more strongly polarizing metal cations, this charge should at least slightly increase to more negative values.

Table 5.7 Integrated charges [e] of the nitrogen atoms in **III**–**V**.

	III	IV	V
N1	-1.73	-1.88	-1.71
N2	-1.68	-1.60	-1.64
N3	-1.66	-1.84	-1.91
N4	-1.74	-1.62	-1.75

The integrated charges for the nitrogen atoms in OMCTS are almost equal. In the two other molecules the covered range of negative charge is, not surprisingly, larger. The different chemical environment of the nitrogen atoms is represented in different atomic charges. One trend is obvious for **IV** and **V**: nitrogen atoms with bonds to two metal cations adopt the highest negative charges of all N atoms, while the integration of the atomic basin of the two protonated nitrogen atoms in **IV** leads to charges similar to those obtained in **III**. It seems that the exchange of one hydrogen atom by a metal cation does not necessarily influence the charge of the nitrogen basin. Charge is shifted in both cases from the substituent towards the nitrogen atom; electron density from an additional (distorted) lone-pair is present in both situations. The higher negative charges for the deprotonated nitrogen atoms in **IV** support the shorter bond lengths as a result of intensified electrostatic attraction. In **V**, the more negative charge of N3 is accompanied by a 2pm shorter Si–N bond lengths compared to N1, although the ellipticity profiles are rather similar in the Si–N bond of both atoms.

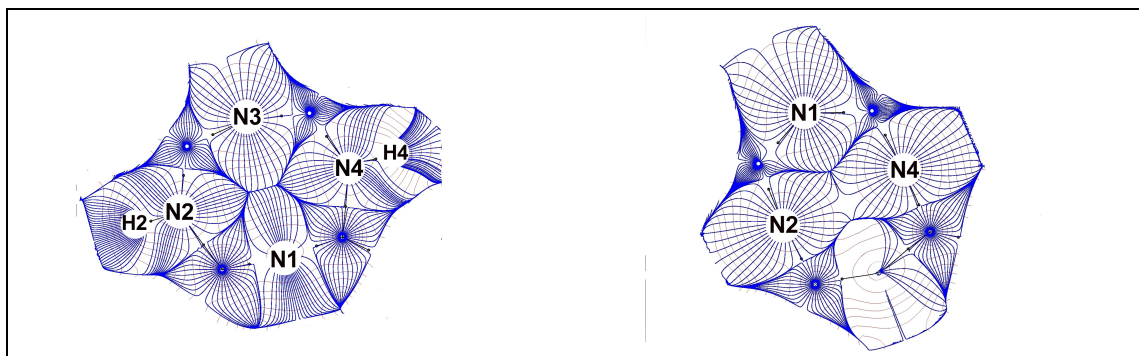


Figure 5.11 Trajectory plots of the N2–N4–N3 plane in **IV** (left) and **V** (right), respectively. The smaller basins on the edges belong to the silicon atoms of the eight-membered heterocycles. Blue lines denote the electron density, $\rho(\mathbf{r})$, red lines trajectories of the electron density, $\nabla\rho(\mathbf{r})$; bond path and the BCPs are drawn in black

Figure 5.11 shows the basins of the Si_4N_4 skeleton in the plane of the nitrogen atoms in **IV** and **V**. From these plots an important difference is obvious. Although the negatively charged nitrogen basins contact each other in both samples, the deformations of the eight-membered rings lead to different transannular nitrogen-nitrogen contacts. In **IV**, the basins of the deprotonated nitrogen atoms, which hold higher charges, share one boundary, whereas in **V**, with an increased deformation, this contact is no longer present. Now, the basins of the two other nitrogen atoms share one boundary of their basins. However, due to the cyclic structure in both samples the repulsion of negatively charged atoms must be taken into consideration. This is an important fact to understand the relatively long Si–N bonds, although slight double bond character is induced by the delocalized lone-pair density. Moreover, it is necessary to point out, that the Si–N bond lengths parallel to the described contacts are slightly elongated in **IV** and **V**. The increased repulsion of the two basins with deprotonated nitrogen in **IV** leads to a small elongation in the four Si–N bonds with protonated nitrogen atoms, while in **V**, the four other Si–N bonds, again parallel to the more pronounced contact, increase in lengths.

Exploiting the AIM theory, the simple argumentation based on the different Si–N bond lengths is no longer valid. The findings underline, that decreasing bond lengths are not necessarily linked to a more ionic character, and *vice versa*. Many more facts have to be considered to judge for the classification.

From Figure 5.8 (b) and (c) it is obvious, that the charge density distribution at a metal–non-metal bonding vector is completely different from the electronic situation in a Si–N bond. More details of these bonds are highlighted from the following topological properties: total electron density, Laplacian along the bond path and deformation of the spatial distribution in $\nabla^2\rho(\mathbf{r})$, the ration of $|\lambda_1|/\lambda_3$, integrated atomic charges and finally

the electronic energy density H_i . The latter is included in the analysis as an additional test if the metal–non-metal interaction is purely ionic.

Along the necessary conditions for an almost pure ionic interaction described in 2.5.5 the topological properties allow a classification of the Li–N, Li–O and Al–N bonds in **IV** and **V**, respectively, as rather pure ionic. The electron density at the BCP is extremely low. It clusters around $0.2\text{e}\text{\AA}^{-3}$ in the Li–E (E = N, O) bonds and $0.6\text{e}\text{\AA}^{-3}$ for the Al–N bonds. In the longest Li–N contact, the electron density is below $0.1\text{e}\text{\AA}^{-3}$ at the BCP. The Laplacian is positive at the BCP and the entire bonding region. Figure 5.12 shows neither high charge depletion nor charge concentration in the bonding region of the Li–N and Al–N contacts, resulting in a Laplacian close to zero in a wide range of the bonding vector. Charge concentration is limited to the nitrogen and oxygen basins near the atomic positions with rather similar distributions in the Al–N and Li–N bonds and a more prominent concentration near the oxygen atoms.

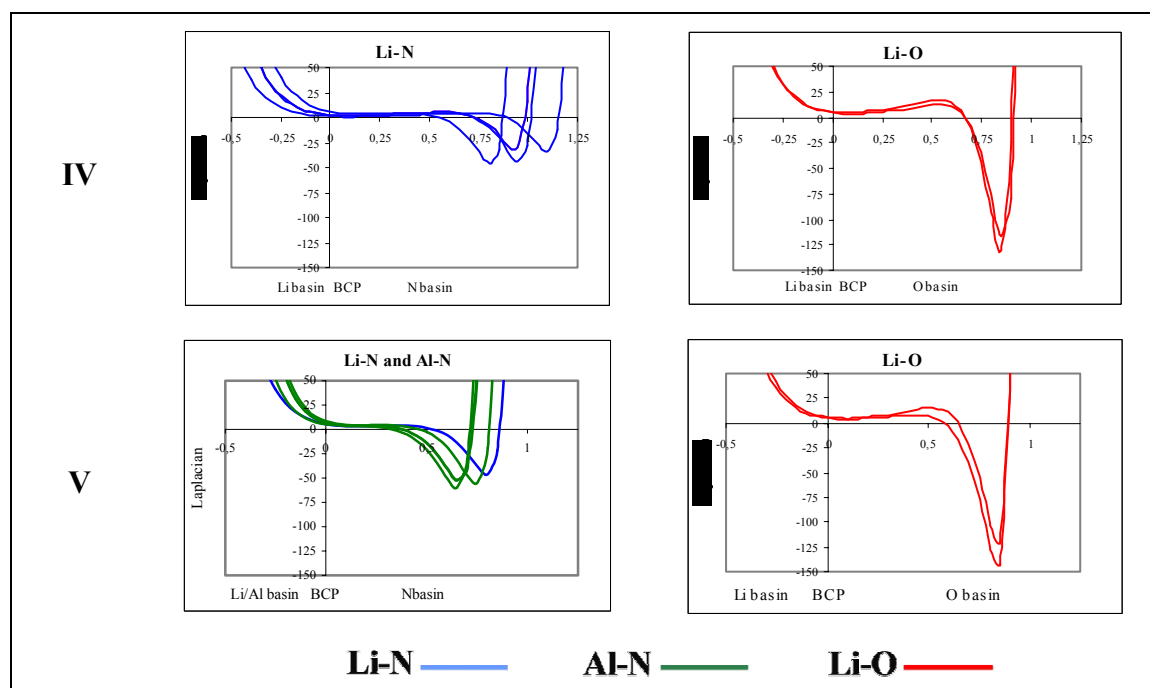


Figure 5.12 Laplacian [$\text{e}\text{\AA}^{-5}$] along the metal–non-metal bond paths [\AA] in **IV** and **V**. The zero value of the x-axis indicates the position of the BCP.

All curvatures in Figure 5.12 indicate a bond with dominate ionic contribution. Compared to the trace of the Laplacian along the highly polar Si–N bond paths the charge concentrations in the bonding regions are lower and the range with the Laplacian close to zero wider. Furthermore, the spatial distributions of $\nabla^2\rho(\mathbf{r})$ in the depicted planes in Figure 5.8 (b) and (c) show almost no deformations towards the metal cation.

The ratio of $|\lambda_1|/\lambda_3$ is much below unity for all metal–non-metal interactions. The average for Al–N bonds is 0.23, while the mean value for both, Li–N and Li–O, is even lower with 0.15.

However, calculations of the electronic energy density at the BCP of the Al–N, Li–N and Li–O bonds based on multipole populations in **V** underline this argumentation only for the Li–E (E = N, O) bonds. All Li–E bonds adopt slightly positive H_1 values (+0.008 – +0.011 au), strongly indicating almost ideal ionic interaction.^{60,121} In contrast, the evaluation of H_1 for the Al–N bonds resulted in very small negative values (–0.018 – –0.039 au) suggesting marginal covalent contributions. A detailed listing of all electronic energy densities calculated for the metal–non-metal bonds discussed in this thesis is presented in chapter 5.4 for Al–N and chapter 5.6 for Li–E, respectively. Unfortunately, the electronic energy densities in **IV** can not be extracted from the multipole parameters due to the limits of the program used for the determination (the number of atoms in the asymmetric unit of **IV** is too large).¹²²

The atomic charges obtained from the integrations over the atomic basins also support dominant or rather pure ionic bonding (Li1 (**IV**) = +0.80e and +0.75e (**V**), Li2 (**IV**) = +0.76e, Al1 = +1.89e). Therefore, a straightforward interpretation of the results in terms of ionicity of the studied metal–non-metal bonds in **IV** and **V** can be given: At this stage, all investigations indicate rather pure ionic (electrostatic) interaction, the covalent contributions, if any, are negligible for the Li–E (E = N, O) bonds. The relatively high total electron density and the electronic energy density at the BCP of the Al–N bonds suggest small covalent augmentation. A detailed discussion of all investigated metal–non-metal contacts, including those of the compounds presented the following chapters, is given in a subsequent chapter.

5.2.1.4 Molecular Properties from the Charge Density Distribution

The static deformation density is derived from the fitted electron density and should be taken into account if transfer of charge is included in the interpretation of the electronic properties. The redistribution of charge into the Si–N bond should be clearly visible from a deformation density plots in terms of a significant deformation of the electronic clouds towards the Si–N bonding regions. The static deformation density distributions of the Si₄N₄ skeletons in **III-V** are presented in Figure 5.13. The absence of a sharp lone-pair at the nitrogen atoms is evident from these plots. All isosurface representations of the static deformation density are in excellent agreement with the conclusions drawn in the previous chapter.

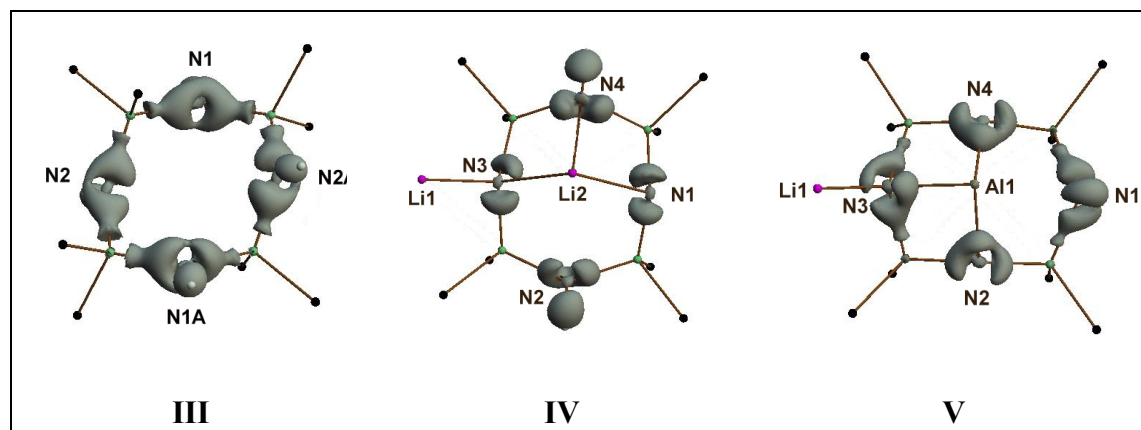


Figure 5.13 Isosurface representation of the static deformation density in **III-V**. For reasons of clarity, only the isosurfaces around the nitrogen, hydrogen and metal atoms are displayed. The isosurfaces are plotted at the $0.25\text{e}\text{\AA}^{-3}$ level.

Subsequent to the classification of bonds in **III-V** on the basis of a multipole refinement and the following analysis of the resulting charge density distributions we turn to another question.

Can this type of analysis really predict the reactivity of a given molecule or locate small areas that are preferred by a given reactant, e.g. by a nucleophile or an electrophile? Within studies on potentially reactive areas a surface with vanishing Laplacian ($\nabla^2\rho(\mathbf{r}) = 0\text{e}\text{\AA}^{-5}$), termed reactive surface, was used to locate regions of charge depletion showing preferred areas for a nucleophilic attack.^{10,123} For the present study it is important to know why the deprotonation of two N(H) moieties in **III** is much easier to achieve than deprotonating all N(H) functions or even only one N(H) group. If double deprotonation occurs why does it always take place region-selectively at two transannular groups regardless to the deprotonation reagent and reaction conditions? The answer is provided by the electrostatic potential (ESP)¹²⁴ of OMCTS (**III**). From Figure 5.14 it is obvious, that the ESP around two N(H) groups is negative, while there are no negative areas around the other two N(H) functions. Consequently, the two latter are the preferred sites for a nucleophilic attack, e. g. of *n*BuLi. This effect is visible in both conformations of the eight-membered heterocycle but more pronounced in the conformer that adopts the boat-conformation depicted in Figure 5.14. Two transannular sites in **III** are deprotonated first to give the dianion (**IV**), as predicted from the ESP. Deprotonation of the third and fourth group needs harsher reaction conditions.

This is a convincing example that the physical properties accessible from charge density studies are a reliable diagnostic tool to predict reactivities from the structure of a molecule.

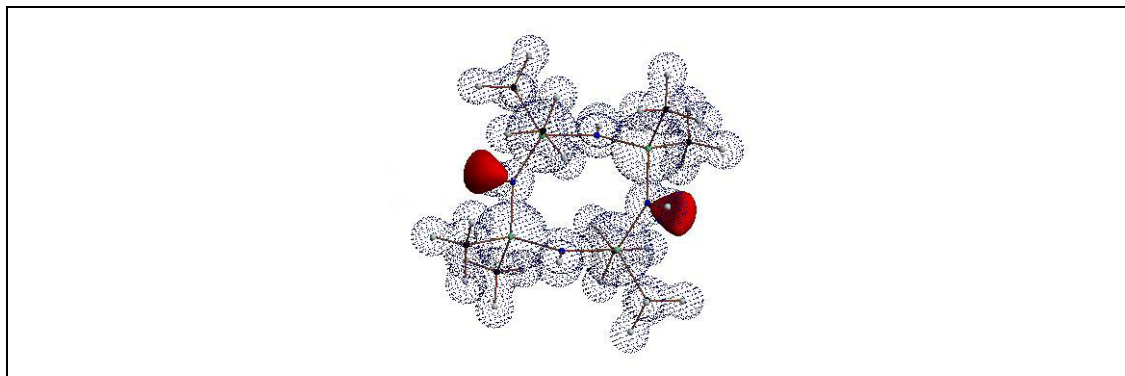


Figure 5.14 Isosurface representation of the electrostatic potential of one molecule in the solid-state structure of **III**; the isosurfaces are plotted at the $+0.35\text{e}\text{\AA}^{-1}$ (blue, dotted) and the $-0.13\text{e}\text{\AA}^{-1}$ (red, filled) level, respectively.

The results obtained from the charge density distribution of the highly polar bonds in tetracoordinated organosilicon compounds are somewhat surprising. Listing of the topology at the BCP is not sufficient at all, even misleading for this bond type. A careful examination of topological properties along the bond path, or inspection of density related properties in 2- or 3-dimensional representations is much more helpful.

All described topological properties above manifest a charge density distribution for highly polar Si–N bonds with remarkable ionic contribution. Nevertheless, redistribution of charge leads to relatively high electron density in the bonding regions. Taking all electronic properties into account, it is obvious that the Si–N bonds in **III-V** are mainly influenced from two features: on one hand this is the degree of transfer of lone-pair density from the nitrogen atoms towards the Si–N bond and consequently a shortening of the bond length, on the other these are the increasing electrostatic interactions after deprotonation which result in a shortening of the bonds, too. Therefore we need two density-based criteria to discriminate between these effects. These tools are the ellipticity investigated along the whole bond path (together with the three dimensional representation of the Laplacian distribution), accounting for electron transfer, and the atomic charge, illustrating the degree of polarization. A third structure determining feature is the electronic repulsion of negative charges, which leads in contrast to the other criteria to an elongation of the bonds. Using these criteria, the Si–N bonds in **III**, **IV** and **V** are classified as follows:

Two main groups can chemically be separated: the Si–N(H) and the Si–N bonds. The two main types can clearly be distinguished in **IV**, which is the only sample where both types are present. The electronic situation of the Si–N bonds in **V** show more similarities with the distribution in the deprotonated moieties of **IV**.

The topological analyses of the charge density distributions reveal distorted lone-pair density at the Si–N(H) moieties in **III** and **IV** that contribute remarkable to the total electron density on the bonding vectors. These findings are supported by high ellipticities and deformation densities smeared towards the Si–N bonds. Furthermore, this group exhibits higher VSCCs at the nitrogen atoms and the charges of the nitrogen atoms are comparable.

In contrast, the group with Si–N bonds enclosing deprotonated nitrogen atoms split in three categories. One, namely the first, can easily be separated, while the differences between the two others with all nitrogen atoms of the tetraanion (**V**), are limited to only a few electronic properties. The first category contains the Si–N(Li) bonds formed from the two deprotonated nitrogen atoms in the dianion (**IV**). These nitrogen atoms, bonded to two lithium cations each, adopt higher negative charges than the protonated, their bonded lone-pair density is less distorted. Thus, the ionicity of these Si–N bonds is enlarged, resulting in the shortest bonds of all investigated Si–N distances. The second category contains the bonds enclosing the two nitrogen atoms (N1 and N3) in the tetraanion identified by the lack of a shoulder in the ellipticity profile of the Si–N bonds. The lone-pair densities of these two atoms are distorted. Therefore the bonds are not as short as in the first category. Within this group, the integrated charge of N3 is increased because of two Al–N contacts. In contrast to the latter, the third category of Si–N bonds related to deprotonated nitrogen atoms is made up from the two N atoms (N2 and N4) in **V** possessing a shoulder in the profile of the ellipticity. The charges of the nitrogen atoms are not increased compared to the protonated N atoms. The Laplacian distribution is rather diffuse. As in the second category, the shortening of the Si–N bond arises from small contributions transferred lone-pair density from the nitrogen atom towards the Si–N bond.

Despite the shortening due to transfer of lone-pair density, the bond lengths in several groups are even longer than those of tabulated standard Si–N single bonds. This fact can be explained by the electrostatic repulsion of the negative charges in the heterocycle. The volumes of the negatively charged nitrogen basins fill most of the space inside the Si₄N₄ skeleton. This is emphasised by the sum of the eight Si–N bonds in the tetraanion (**V**), which is slightly higher than in OMCTS (**III**), although all Si–N bonds in these two compounds are classified as highly ionic with delocalized lone-pair densities. The sum of the bond lengths in the dianion is, not astonishing, the smallest owing to four Si–N bonds being part of the group ‘highly polar and delocalized lone-pair’ and four shortened bonds due to increased electrostatic interactions after deprotonation of the nitrogen atoms. .

Concerning the Si–N bonds in these compounds, the topological analysis proves that contra-intuitively deprotonation and subsequent metallation does not necessarily result in a higher polarity of the bond. Especially for highly negative charged systems, the opposite effect, the repulsion of charge, also plays an important role for the electron distribution. In addition, the lithium–non-metal bonds in these samples are classified as almost pure ionic bonds, the aluminium–non-metal bonds are strongly dominated from ionic contributions, but most likely an additional, not negligible small amount of covalent contribution is present in the latter bond type. An effect of the different metal cations in the structures of **IV** and **V**, with respect to the Si–N bonding, can not be extracted from the analysis. It seems that the different electron density distributions in the bonds with deprotonated nitrogen atoms are mainly caused from the increased charge in **V** and not from the different metal cations.

5.2.2 Si–N in a Hexacoordinated Organosilicon Compound

Hundreds of structures of hexacoordinated organosilicon complexes were published in the last decades.¹²⁵ None of those publications contains a quantitative analysis of the electron distribution in a Si–N bond although this bond type is present in many of the published molecules. The inspection of this bonding type shows whether the different coordination sphere leads to changes in the charge density distribution of the Si–N bond apart from changes in the bond length. The studied organosilicon compound, Difluoro-bis-[N-(dimethylamino)phenylacetimidato-N,O]silicon²¹ (**VI**) contains a ‘dative’ N→Si bond. Furthermore, two other sets of highly polar silicon bonds, Si–E (E = O, F) are present. Their bonding properties as well as the electronic situation in the five-membered heterocycle SiOCN₂ is also discussed in detail. Hexacoordinated silicon compounds are widely termed ‘hypervalent’,¹²⁶ indicating a valence expansion of the silicon atom. The topological analysis elucidates whether this expression is valid.

5.2.2.1 Molecular Structure

The asymmetric unit of [F₂Si{OC(Ph)=NNMe₂}₂], **VI**, contains half the molecule with the silicon atom on a special position. The complete molecule is generated from a two-fold axis through Si and the bisection of the two oxygen atoms (Figure 5.1 (d)).¹²⁷ Silicon complexes with the chelating ligand, the dimethylamino-acylimidato(N,O) moiety [OC(R)=NNMe₂], have been reported previously.¹²⁸

The octahedral environment of the central silicon atom is only slightly distorted. The mean deviation of the oxygen and fluorine atoms from the equatorial plane is only

0.0785 Å. The angle N1–Si1–N1A, including the two axial ligands, is 171.0°. The fact, that the fluorine substituents in **VI** are oriented *cis* to each other has generally been observed in other dihalo-dimethylamino chelates.¹²⁹ The dative N→Si bond (1.9966(3) Å) is much longer than the Si–N bonds of the tetrahedral coordinated silicon atoms discussed in the previous chapter. Besides, the N→Si contacts from the present ligand are elongated compared to the N→Si bonds in the closely related chelating isopropylideneimino-acylimidato(N,O) moiety, also prepared from Kalikhman et. al.²¹ In addition, it is interesting to compare the Si–F distances of the complex series with these two ligands. While the N→Si distances are shorter in the isopropylideneimino series relative to the dimethylamino analogons, the opposite is found for the Si–F bonds: they are consistently longer in the isopropylidene compounds. These divergent trends may be regarded as different points along a hypothetical S_N2 reaction coordinate, in which the presumed stronger donor, the isopropylideneimino moiety, is associated with a more advanced reaction: the nucleophile–silicon bond is shorter, while the silicon-leaving group distance gets longer.²¹

The five-membered SiOCN₂ heterocycle of the asymmetric unit is almost planar with a mean deviation of 0.0529 Å from the best plane through the five atoms. The R-group of the organic ligand in the studied compound is a phenyl group. Although the steric requirements of this substituent are rather high, it is almost in plane with the central heterocycle. The angle between the two planes is 12.6°. This orientation coincides with a shortened C3–C4 and C3–O1 bond, suggesting a coupling of the negatively charged ligand to the phenyl ring.

The distribution and orientation of the lone-pairs at the donating nitrogen atom and at the fluorine ligand are deducible only from charge density studies. The same is valid to confirm the delocalization of charge from the heterocycle to the phenyl group.

5.2.2.2 Multipole Refinement

The populations of the central silicon atom were refined to the hexadecapolar level, those of other non-hydrogen atoms to the octapolar level. For the hydrogen atoms solely a bond-directed dipole was included in the refinement. Radial screening factors (κ and κ') were introduced and refined for each atom type. For the two types of chemically different carbon atoms (C_{methyl} and C_{phenyl}) and the two different nitrogen atoms different sets of κ and κ' values were refined. Reflections to $\sin\theta/\lambda_{\text{max}} = 1.10 \text{ \AA}^{-1}$ with $I > 2(\sigma)I$ were included in the refinement following the standard procedure. Due to the special position (crystallographic 2-fold axis) several restriction were applied for the silicon atom:

- only those multipoles that obey the symmetry picking rules for the 2-fold axis were employed
- x and z coordinates were fixed
- u₁₂ and u₂₃ were not refined ($u_{12} = u_{23} = 0$)

The following list contains additional constraints imposed to reduce the number of parameters:

- local symmetry:*
- three-fold axis along the C–N bond for the carbon atoms of the methyl groups,
 - mirror planes for each atom of the phenyl ring.
- similarity constraints:*
- methyl carbon atoms C2 equals C1,
 - carbon atoms in the phenyl ring with the same chemical environment ($C8 = C6$, $C5 = C9$),
 - hydrogen atoms of all methyl groups,
 - hydrogen atoms of the phenyl ring.

The DMSDA test after multipole refinement reveals an excellent deconvolution of the electron density from thermal motion. All DMSDAs are between $0.0 \cdot 10^{-3} \text{Å}^2$ – $0.8 \cdot 10^{-3} \text{Å}^2$. The residual maps of the main molecular planes show no significant densities (Figure 5.15).

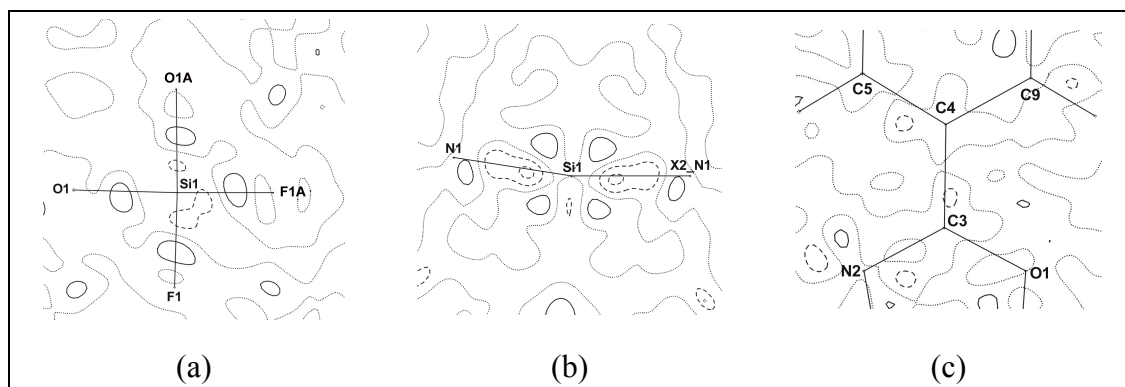


Figure 5.15 Contour plots of the residual densities after multipole refinement of **VI**, $\sin\theta/\lambda_{\max} = 0.90 \text{Å}^{-1}$. (a) Si1–F1–O1 plane; (b) N1–Si1–N1A plane; (c) N2–O1–C4 plane. Positive contours solid, zero-level contour dotted, negative contours dashed. Stepwidth is 0.1eÅ^{-3}

5.2.2.3 Topological Analysis

Quantitative studies of dative $\text{N} \rightarrow \text{Si}$ bonds in organosilicon compounds, based on experimental data, are not yet available. There is only one example of a theoretical

study on Si–N bonds in a small model compound.¹³⁰ Results of an experimental charge density study on K₂[SiF₆] were published from Herster et al.¹³¹ However, quantitative results of a topological analysis are not reported.

Table 5.8 Crystallographic data after multipole refinement of VI.

compound	V
formula	C ₁₈ H ₂₂ F ₂ N ₄ O ₂ Si
crystal system	monoclinic
space group	C2/c
a [Å]	19.8444(7)
b [Å]	8.5365(3)
c [Å]	12.0682(4)
β [°]	113.7310(1)
V [Å ³], Z	1871.51(11), 4
μ [mm ⁻¹]	0.17
T _{min} / T _{max} (low-angle batch)	0.79 / 0.98
T _{min} / T _{max} (high-angle batch)	0.77 / 0.98
refl. used in the multipole refinement	8717
after cut-off *	
sinθ/λ _{max, cut} [Å ⁻¹]	1.10
completeness to sinθ / λ _{max, cut} [%]	98.9
no. of unique reflections (low-angle batch) / R _{int}	1919/ 0.0537
no. of unique reflections (high-angle batch) / R _{int}	9529/ 0.0738
limiting indices	-45 ≤ h ≤ 41, -0 ≤ k ≤ 19, 0 ≤ l ≤ 27
max. shift / esd in final cycle	0.29 · 10 ⁻¹
R1 (I > 2σ(I)) after IAM refinement to sinθ/λ _{max, cut}	0.0355
wR2 (I > 2σ(I)) after IAM refinement to sinθ/λ _{max, cut}	0.0982
R1 (I > 2σ(I)) after multipole refinement to sinθ/λ _{max, cut}	0.0273
wR2 (I > 2σ(I)) after multipole refinement to sinθ/λ _{max, cut}	0.0449
GoF	2.54
N _{refl.} / N _{param.}	31.93

* with respect to these cut off criteria: I > 2σ(I); sinθ/λ_{max, cut}

The classification of the Si–E (E = N, O, F) bonds is based on various criteria deduced from the results of the multipole refinement: electron density, the Laplacian along the bond path and its spatial distribution around the electronegative atoms. Furthermore, the calculated electronic energy density at the bond critical point and experimental charges obtained from the integration over the atomic basins. All anticipated BCPs in the bonding regions are found. Concerning the Si–E bonds, they are located closely to the electropositive silicon atom (Table 5.9). The values of total density $\rho(\mathbf{r}_{\text{BCP}})$ and the Laplacian at the BCP in the phenyl ring of **VI** match those of other compounds, further supporting the credibility of the used model.¹⁰⁷ A ring critical point could be determined in the centre of the phenyl ring as well as in the SiOCN₂ five-membered heterocycle, respectively.

The Si–O as well as the Si–F bond lengths are in the range normally observed for hexacoordinated silicon compounds.¹²⁵ The electron density at the BCP of the Si–E bonds is remarkably low compared to those bonds classified as polar covalent bonds including third row elements like S and P.^{11,13} The density of $0.5 \text{ e}\text{\AA}^{-3}$ at the BCP of the dative Si–N bond ($1.9966(3)\text{\AA}$) is only half the amount found for the shorter Si–N bonds in $[c\text{-Me}_2\text{SiN(H)}]_4$, **III**, $d_{\text{av.}} = 1.7251(46)\text{\AA}$. Apart from the bond lengths this suggests different bonding situation along the N→Si vector in **VI**.

Table 5.9 Topological properties at the BCP of the Si–E (E = N, O, F) bonds and the bonds of the five-membered heterocycle in **VI**.

A–B	d(A–B)	d(A–BCP)	d(BCP–B)	$\rho(\mathbf{r}_{\text{BCP}})$	$\nabla^2\rho(\mathbf{r}_{\text{BCP}})$	H_{I}	Charge B*
Si–N1	1.9703	0.7627	1.2076	0.501(16)	7.755(29)	-0.010	-0.78
Si–F1	1.6397	0.7040	0.9357	1.015 (13)	13.472(33)	-0.076	-0.80
Si–O1	1.7789	0.7476	1.0313	0.776(13)	7.737(22)	-0.052	-1.21
N1–N2	1.4598	0.7477	0.7120	1.998(18)	-2.149(41)	**	**
O1–C3	1.3101	0.8042	0.5058	2.393(29)	-26.884(138)	**	**
N2–C3	1.2983	0.7670	0.5313	2.844(27)	-35.251(123)	**	**
C3–C4	1.4792	0.7926	0.6866	1.942(17)	-15.408(50)	**	**

$d(\text{A–B})$ is the bond path length between the atoms A and B [\AA], $d(\text{A–BCP})$ and $d(\text{B–BCP})$ denote the distances of the atoms A and B from the BCP [\AA], $\rho(\mathbf{r}_{\text{BCP}})$ [$\text{e}\text{\AA}^{-3}$] is the charge density and $\nabla^2\rho(\mathbf{r}_{\text{BCP}})$ [$\text{e}\text{\AA}^{-5}$] the Laplacian at the BCP, respectively. H_{I} is the electronic energy density [au] at the BCP. The charges [e] are derived from the integration over the atomic basins.* Charge of the silicon atom (atom A in the first three lines): +2.78. ** Not calculated.

The Laplacian distribution of the atoms bonded to silicon (Figure 5.16) shows an almost spherical distribution around O and F. The polarization of the lone-pair charge concentration around the donating nitrogen atom indicates charge transfer towards the silicon atom. In a detailed study of dative bonds, based on theoretical data, Jonas et al.

demonstrated that all $N \rightarrow E'$ ($E' = B, Al$) bonds with characteristic deformations of the charge concentrations towards the acceptor atom revealed significant covalent contribution.¹³² As the positions of the BCPs are vital and the values differ drastically with slight variations of the position, the Laplacian of the Si–E bonds is monitored along the whole bond path for the highly polar bonds in this molecule.⁶⁶ The Laplacians at the BCPs for the three different Si–E bonds are all positive with the maximum at the Si–F bond of $\nabla^2\rho(\mathbf{r}_{\text{BCP}}) = 13.472\text{e}\text{\AA}^{-5}$ followed by the Si–N and Si–O bond with $7.755\text{e}\text{\AA}^{-5}$ and $7.373\text{e}\text{\AA}^{-5}$, respectively.

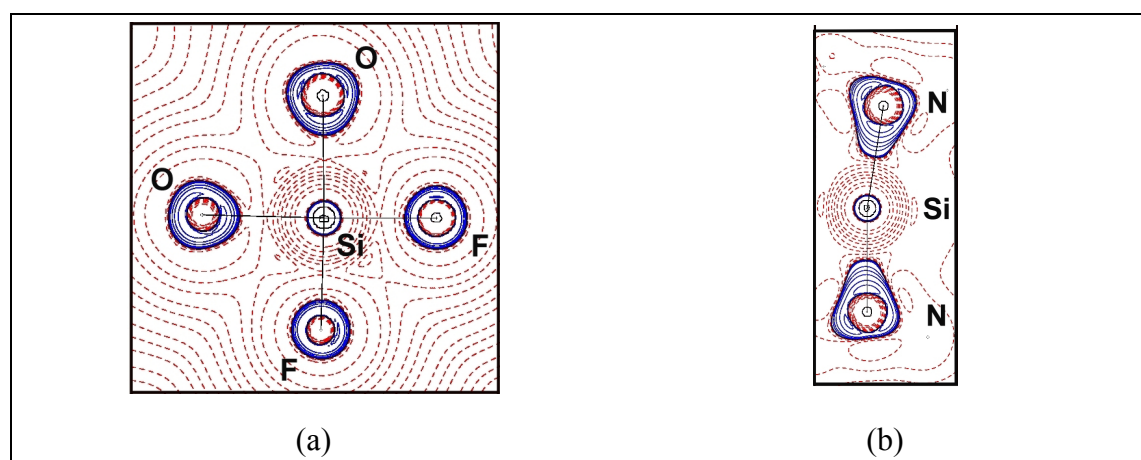


Figure 5.16 Laplacian in the O_2SiF_2 (a) and the SiN_2 plane (b) of **VI**; positive values of $\nabla^2\rho(\mathbf{r})$ are depicted by red, negative by blue lines. Contours drawn at $0.000, \pm 2.0 \cdot 10^n, \pm 4.0 \cdot 10^n, \pm 8.0 \cdot 10^n \text{e}\text{\AA}^{-5}$, where $n = 0, \pm 1, \pm 2, \pm 3$.

From Figure 5.17 it is obvious that the Laplacian along the three bond paths is positive at any point in the silicon basin indicating charge depletion in a sphere with a radius considerably larger than the distance Si–BCP. The situation along the Si–F and Si–O bond path is similar: positive values at the BCP and in the entire bonding region with a more positive Laplacian for the Si–F bond at each point. Close to the more electronegative atom the Laplacian changes rapidly due to charge concentrations. Despite the almost identical values at the BCPs for the Si–N and Si–O bonds, the Si–N bond shows a different Laplacian distribution in the basin of the nitrogen atom. The Laplacian is close to zero in a wide range of the bonding region. The Si–N bonds in **III** and **VI** adopt almost identical values at the BCP, too. The distribution in the silicon basin is also comparable. Nevertheless, the curvature of the Laplacian in a nitrogen basin of **III** differs remarkable from that in **VI**; the area on the bonding vector with small charge concentrations in **VI** is 0.25\AA longer than in **III**. This clearly demonstrates the advantage of the inspection of the whole bond path.

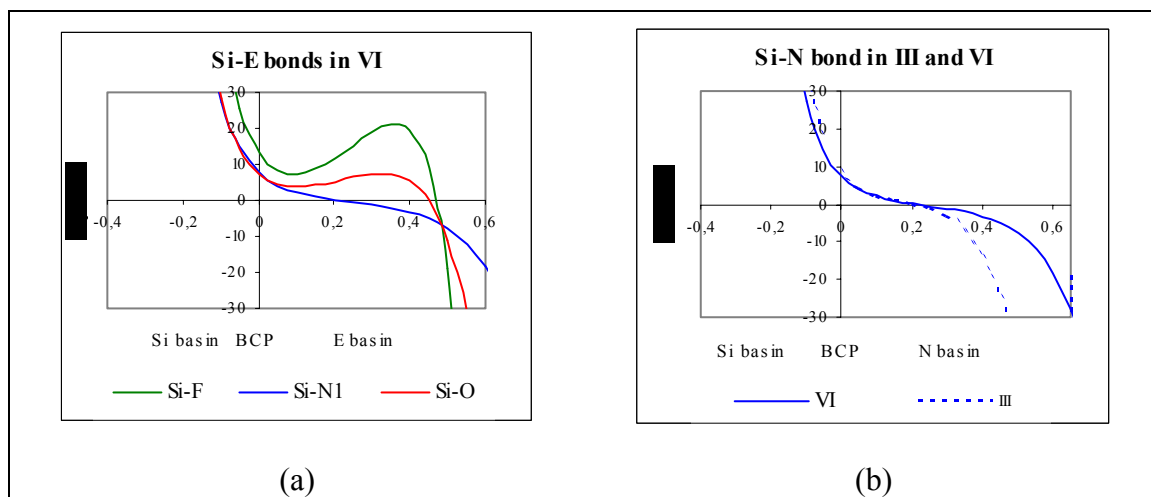


Figure 5.17 Laplacian along the bond paths in (a) Si–E (E = N, O, F) of **VI**; (b) comparison of Si–N bonds in **III** and **VI**. The zero value of the x-axis indicates the position of the BCP.

Moreover, intensive searches for (3;-3) critical points in the spatial distribution of $\nabla^2\rho(\mathbf{r})$ were carried out to localize and quantify maximum charge concentrations in the bonding and non-bonding regions of the valence shell (VSCCs). With this procedure we gain information about the Laplacian distribution apart from the bonding regions. Inspection of the VSCCs around the electronegative atoms in the coordination sphere of the Si atom led to interesting results (Figure 5.18). Around the donating nitrogen atom a sharp maximum is located on the bonding vector directed towards the silicon atom. The four VSCCs around this nitrogen atom are obviously less distorted than the maxima around the nitrogen atoms in **III-V** (Figure 5.9).

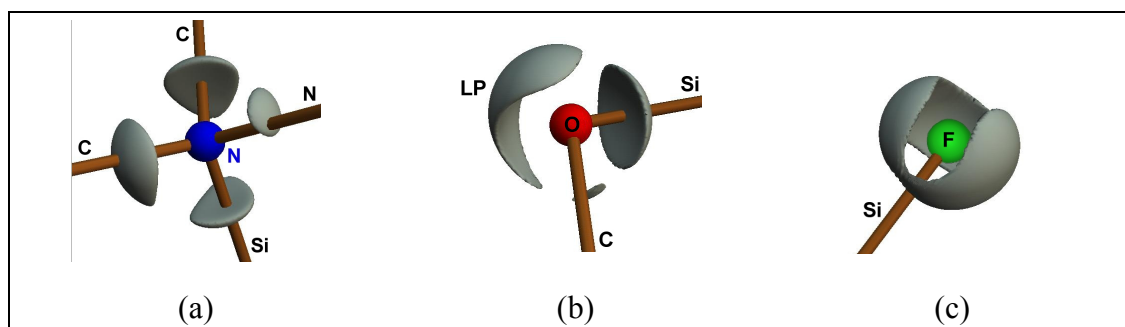


Figure 5.18 Isosurface maps at constant $\nabla^2\rho(\mathbf{r})$ values for the atoms coordinated to the silicon atom indicating bonded and non-bonded charge concentrations around the displayed atoms; (a) N1, $\nabla^2\rho(\mathbf{r}) = -48\text{e}\text{\AA}^{-5}$; (b) O1, $\nabla^2\rho(\mathbf{r}) = -92\text{e}\text{\AA}^{-5}$; (c) F1, $\nabla^2\rho(\mathbf{r}) = -180\text{e}\text{\AA}^{-5}$.

Three lone-pairs at the fluorine atom, identified by three non-bonding maxima in the valence shell could be determined. They tend to couple from two sides towards the silicon bonding vector (Figure 5.18 (c)) indicating redistribution of charge in the Si–F bond and thus explaining the rather high value of $\rho(\mathbf{r})$ at the BCP for this bond.¹³³ The

banana-shaped non-bonding VSCC at the oxygen atom encloses the maxima of the lone-pair region; due to the rather diffuse shape of this VSCC the exact maxima of the expected two lone-pairs could not be located.

Local concentrations and depletions of the electron density in the internuclear region are connected with the features of the electronic energy density *via* the local form of the virial theorem.⁵⁸ It describes an exact relationship between the second derivative of the electron density, $\nabla^2\rho(\mathbf{r})$, the electronic kinetic energy density $G(\mathbf{r})$ (calculated by using the Kirzhnits approximation) and the electronic potential energy density $V(\mathbf{r})$. The electronic energy density (see 2.5.3) provides a straight criterion for the classification of the atomic interaction: $H(\mathbf{r}_{\text{BCP}}) < 0$ is observed in shared-type (covalent) atomic interactions, while $H(\mathbf{r}_{\text{BCP}}) \geq 0$ is observed in purely closed-shell (ionic) interactions.^{60,134} Typical values of $H(\mathbf{r}_{\text{BCP}})$ for covalent single bonds cluster around -0.35.⁶⁰ The electronic energy density of the N→Si bond equals zero, those for Si–O and Si–F are slightly negative (Table 5.9). Although the deformation of the charge concentration at the donating nitrogen atom towards the silicon atom suggests at first sight high negative value for $H(\mathbf{r}_{\text{BCP}})$ as reported from Jonas et. al.,¹³² the electronic energy density is practically zero at the BCP of the N→Si bond. For the Si–F and the Si–O bond the energy $H(\mathbf{r}_{\text{BCP}})$ is slightly negative, *in toto* indicating absolute ionic domination in the N→Si bond and ionic interactions with small covalent contributions to the Si–F and Si–O bonds.

The ratio of $|\lambda_1|/\lambda_3$ at the BCP is also used for the classification of the highly polar Si–E bonds in **VI**. As pointed out earlier, for ionic bonds (closed-shell interaction), this quotient should be below unity because of the large value of λ_3 ; in addition the values for λ_1 and λ_2 are small compared to those in bonds with shared interaction. Values of 0.26, 0.29 and 0.20 for the Si–F, Si–O and Si–N bond, respectively, affirm the findings in the Laplacian. Especially the ratio for the dative Si–N bond underlines the domination of λ_3 at the BCP and thus an interatomic charge depletion.

Reliable atomic charges, tabulated above, can be derived from the integration of the electron density over the atomic basins. These basins are the result of a partitioning of a molecule into atomic regions with boundaries according to Bader's AIM theory. The integration over the atomic basins proved a highly positive charged silicon atom and negative charges for fluorine, oxygen and nitrogen atoms, respectively. The atomic basins of the SiOCN₂ heterocycle are displayed in Figure 5.19 together with the Laplacian distribution in this plane.

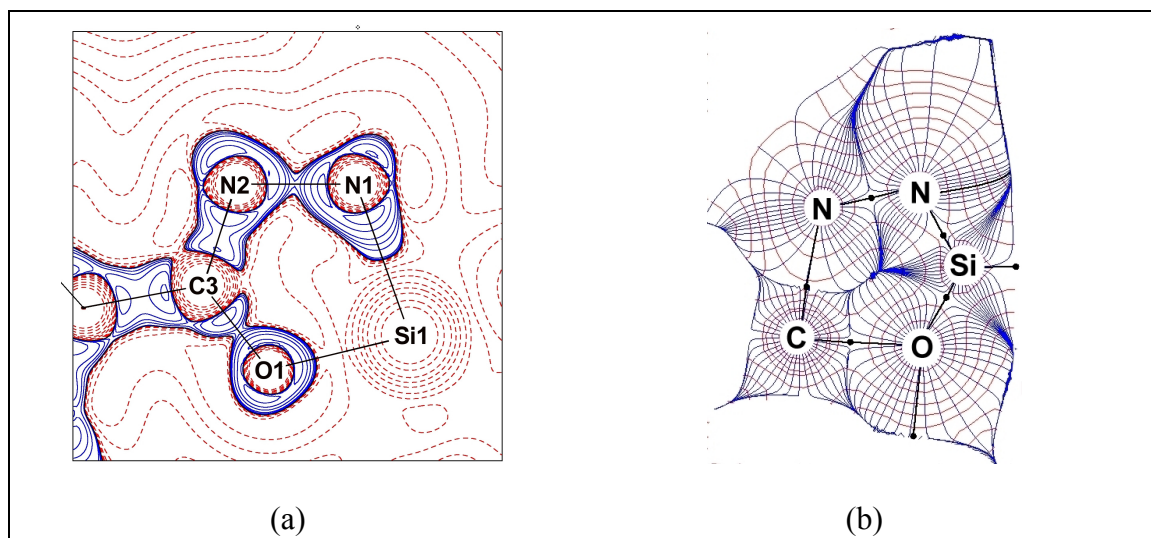


Figure 5.19 Laplacian (a) and a two dimensional trajectory plot in the plane of the SiOCN₂ heterocycle (b) of **VI**; positive values of $\nabla^2\rho(\mathbf{r})$ in (a) are depicted by red, negative by blue lines; contours drawn at 0.000 , $\pm 2.0 \cdot 10^n$, $\pm 4.0 \cdot 10^n$, $\pm 8.0 \cdot 10^n$ eÅ⁻⁵, where $n = 0, \pm 1, \pm 2, \pm 3$; (b) visualizes the different shape and size of the atomic basins; red lines denote electron density, blue lines are trajectories of the electron density; bond paths and BCPs are black

The situation around the oxygen atom is special because the bond lengths in addition to the electron density and the Laplacian distributions indicate a slight delocalization of charge towards the neighbouring carbon atom. Indeed, the topological properties of the other bonds in the five-membered heterocycle, listed in Table 5.9, are not all signing features of pure single or double bonds. The N–N bond assigns a bond length and electronic properties of a normal single bond¹³⁵ whereas the N2–C3 bond shows typical values for a slightly polar double bond.¹³⁶ The topological properties of the O1–C3 and the C3–C4 bond, the latter joining the heterocycle and the phenyl moiety, are between those of double and single bonds. The total electron densities on the bonding vectors are too high, the Laplacian too negative and the bond lengths are too short for a standard single bond.¹³⁷ Obviously, negative charge is delocalized from the O1C3C4-backbone towards the phenyl ring. This explains the almost coplanar arrangement of the heterocycle and the phenyl substituent.

An inspection of the ellipticities along the bond paths (Figure 5.20(a)) in the heterocycle displays a bonding situation deviating from pure σ -interactions, too. The asymmetric, bell-shaped curvature of N2–C3 is typical for a heteroatomic double bond. The ellipticity of the N1–N2 bond, classified as single bond, shows rather low values around the bond critical point. In contrast, the two other bonds depicted in this figure show lower ellipticities than the double bond but enlarged ϵ values and a different shape compared to the N2–C3 σ -bond.

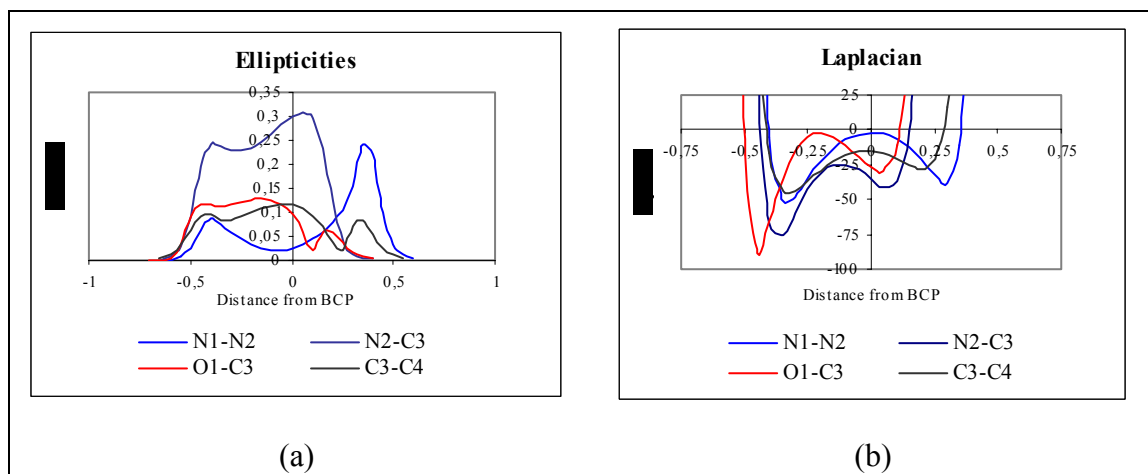


Figure 5.20 Ellipticities ϵ (a) and Laplacian $\nabla^2\rho(\mathbf{r})$ [$\text{a}\text{\AA}^{-5}$] (b) along the bond paths [\AA] in the heterocycle of **VI** (bonds to Si excluded). The zero value of the x-axis indicates the position of the BCP.

The topological analysis from experimental data reveals predominantly ionic bonding and much less covalent contribution than commonly anticipated for all Si–E (E = N, O, F) bonds. Even the large amount of electron density at the silicon–fluorine vector can be explained with this method. Moreover, the negative charge in the five-membered heterocycle, gained from the integration over the atomic basins, seems to be partially delocalized – slightly including the phenyl fragment in the delocalization.

5.2.2.4 Molecular Properties from the Charge Density Distribution

As demonstrated for the tetrahedral silicon compounds, a transfer and redistribution of charge is visible in the static deformation density. Figure 5.21 proofs this fact for **VI**. The lone-pair density is shifted towards the Si–F bonding vector, while the lone-pair density of the oxygen atom is oriented perpendicular to the heterocycle and towards the neighbouring carbon atom, respectively. The static deformation density of O1 on the Si–O bond is also moderately distorted, whereas the shape of the aspherical density around the dative nitrogen atom manifests more pronounced orientation to all four bonding vectors.

The dispute whether this silicon is hypervalent or high-coordinated is elucidated by this experimental charge density determination and subsequent topological analysis of three different highly polar Si–E (E = F, O, N) bonds in the hexacoordinated organosilicon compound **VI**. Considering all electronic features determined experimentally one can conclude that the silicon atom in **VI** should definitely not be classified as hypervalent.

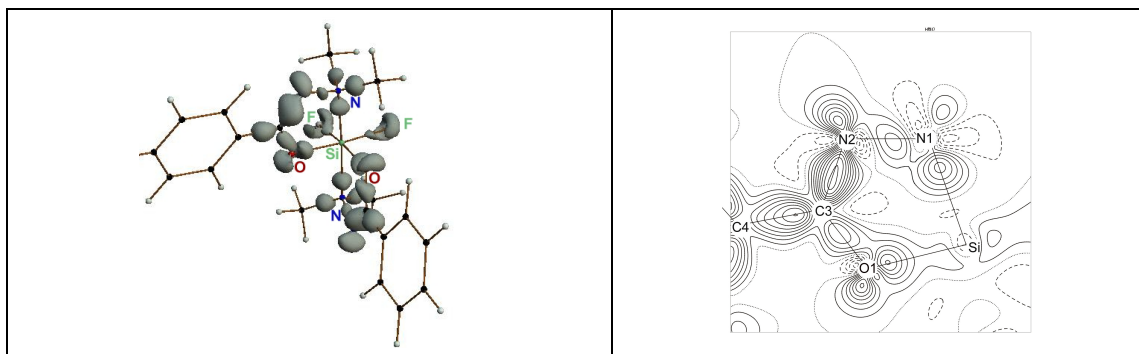
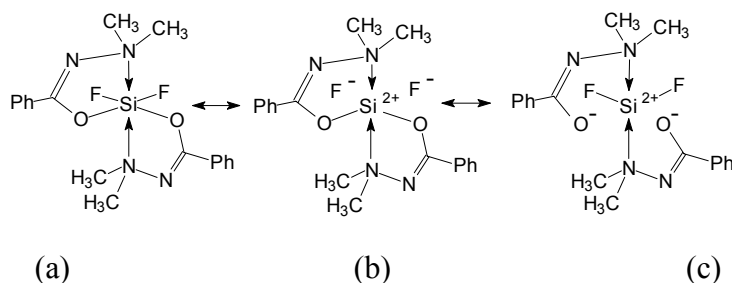


Figure 5.21 Isosurface representation (a) and contour plot (b) of the static deformation density in **VI**. For clarity reasons, in (a) only the isosurfaces of Si–E (E = N, O, F) and the heterocycle are drawn, respectively. The isosurface is plotted at the $0.25\text{e}\text{\AA}^{-3}$ level. In (b), only the contours in the plane of the heterocycle are drawn. Positive contours solid, zero contour dotted, negative contours dashed; stepwidth is $0.1\text{e}\text{\AA}^{-3}$.

Two different kinds of bonds around the hexacoordinated centre are present. The Si–N bonds in **VI** clearly are dative bonds with completely different electronic properties than the shorter non-dative Si–N bonds in **III–V**. The question of whether dative bonds are to be classified as covalent or ionic remains controversial. However, almost all bonding properties in **VI** suggest absolute ionic domination and it is just the deformation of the lone-pair charge concentration that might introduce a notable covalent contribution. The four remaining Si–E (E = O, F) bonds indicate predominantly ionic contributions and small covalent augmentation. The slightly negative electronic energy density and the amount of total electron density at the BCP support covalent contributions, while the positive Laplacian in the whole bonding region, an atomic-like Laplacian distribution, the $|\lambda_1|/\lambda_3$ ratio smaller than 0.3 suggest ionic domination. Together with the experimental atomic charge higher than +2 of the silicon atom all electronic properties suggest that the Lewis structures (b) and (c) in Scheme 5.1 contribute most to the appropriate bond description and the covalent contribution obviously is much lower than commonly anticipated.



Scheme 5.1 Resonance forms of $[\text{F}_2\text{Si}\{\text{OC}(\text{Ph})=\text{NNMe}_2\}_2]$, **VI**: (a) suggest predominant covalent bonding for all ligand atoms; (b) and (c) show canonical forms with ionic contribution.

5.3 Charge Density Study on a Lithiated Picolylphosphane

The lithiated iminophosphorane, $[(\text{Et}_2\text{O})\text{Li}\{\text{Ph}_2\text{P}(\text{CHPy})(\text{NSiMe}_3)\}]$, **VII**, contains several highly polar bonds. In the centre of the molecule, the phosphorus atom is bonded to carbon and nitrogen atoms, while in the periphery, nitrogen and oxygen atoms coordinate one lithium cation. Although phosphorus containing ligand systems with donating atoms in the periphery have shown increasing importance in catalysis and the design of self assembling ligands,³⁰ detailed studies of the highly polar bonds in these systems are missing. Lithium–non-metal contacts have already been investigated in the metallated Si_4N_4 heterocycles of **IV** and **V**. An additional analysis of this structure leads to more general conclusions for the Li–N and Li–O bonding type.

5.3.1 Molecular Structure

The lithiated iminophosphorane, **VII**, crystallizes as yellow blocks from diethyl ether after several days at room temperature. The solid-state structure of **VII** is shown in Figure 5.22.

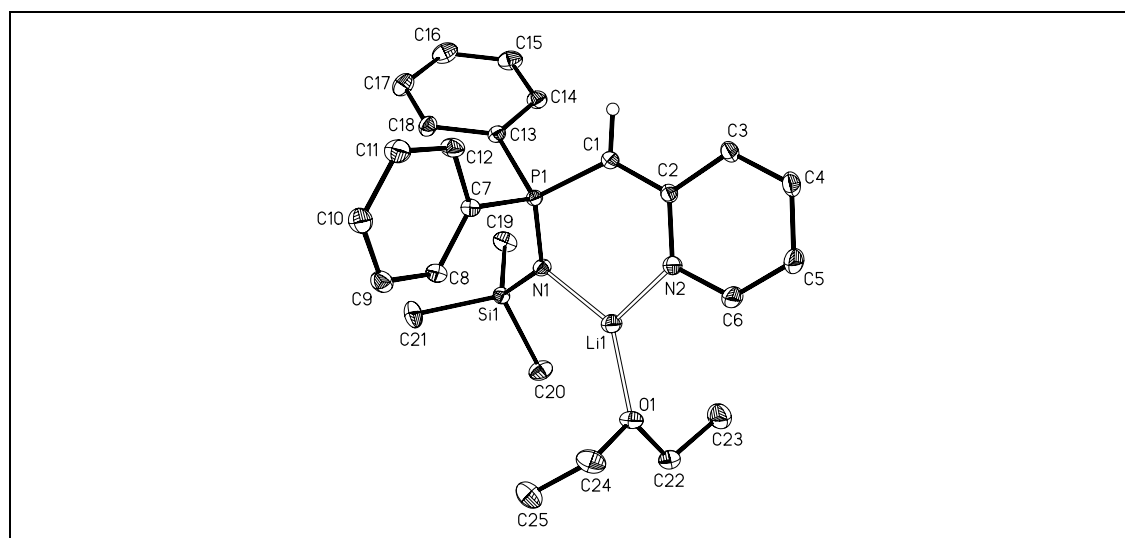


Figure 5.22 Solid-state structure of **VII**. Hydrogen atoms, but H1 are omitted for clarity. The anisotropic displacement parameters are depicted at the 50% probability level.

The trigonal planar coordination sphere of the lithium cation is made up of the imino nitrogen atom N1, the pyridyl nitrogen atom N2 and the oxygen atom of the donating diethyl ether molecule. The metal cation is displaced only 22.6pm from the best plane determined by these three atoms. As anticipated from the coordination behaviour,¹³⁸ a six-membered twisted metallacycle is formed. Different to the chemically related iminophosphoranates $[(\text{THF})\text{Li}\{\text{HC}(\text{Ph}_2\text{PNSiMe}_3)_2\}]$ ¹³⁹ and $[(\text{Et}_2\text{O})\text{Li}\{\text{HC}(\text{Cy}_2\text{PN}-$

$\text{SiMe}_3)_2\}}],^{140}$ the lithium cation in **VII** shows no interaction with the deprotonated carbon atom C1 ($\text{Li1}\cdots\text{C1}$ 3.2250 Å). The angles at C1 are close to 120° , indicating sp^2 -hybridization. Different to the parent iminophosphorane starting material presented in the introduction the metal coordination causes a N1/N2 *cisoid* conformation. The Li1–N1 distance in **VII** (1.9448(5) Å) is slightly shorter than the Li1–N2 contact of 1.9625(5) Å. Both are comparable to Li–N distances found in lithium amides,¹⁴¹ lithium iminophosphoranes¹⁴² and lithium aminidates.¹⁴³ The Li1–O1 bond (1.9209(7) Å) as well as the Li–N contacts in **VII** are in the range of the Li–E (E = N, O) interactions in **IV** and **V**. In contrast to the P–C_{Ph} bond lengths (av. 1.8219 Å), which do not differ significantly from those found in the starting material, the P1–C1 bond (1.7252(2) Å) length is shortened by 10 pm, which would be consistent with a partial double bond character as suggested by the resonance structure (b) in Scheme 1.3. The C1–C2 distance of 1.5039(2) Å in the neutral phosphane also decreases by approximately 10 pm to 1.4022(3) Å in **VII**, indicating a partial C=C double bond character as depicted in (c) of Scheme 1.3. Simultaneously, the C2–N2 bond length in the pyridyl ring of the parent iminophosphorane (1.3707(3) Å) is elongated by 4 pm. In contrast to the P1–C1 bond in **VII**, the P1–N1 bond in **VII** is approximately 5 pm longer than in the starting material, but with 1.5900(2) Å still in the range generally quoted for a formal P=N double bond.¹⁴⁴ These geometrical features suggest canonical formulae as depicted in Scheme 1.3. However, all of them require valence expansion at the phosphorus atom, not obeying the eight electron rule, but chemical reactivity neither supports P=N nor P=C double bonds because both are easily cleaved in various reactions.

From the results of a topological analysis, subsequent to a multipole refinement, the charge density distribution of the formal double bonds and the bonds enclosing lithium can be deduced and therefore these bonds can be classified in terms of single or double bond character. The dominating force of these bonds, covalent or ionic, can also be concluded from this analysis. Moreover, the location of the negative charge, resulting from the deprotonation of C1, is determined.

5.3.2 Multipole Refinement

The multipole populations centred at the phosphorus atom as well as those at silicon, oxygen and the two nitrogen atoms were refined to the hexadecapolar level. For the multipoles of all carbon atoms and the lithium atom refinement to third order remained sufficient to describe the bonding densities. For the hydrogen atoms only a bond-directed dipole population was included. Extraction/contraction factors (κ and κ') were introduced and adjusted for each atom type. To account for the different environment,

four different κ -sets for the carbon atoms were introduced – one each for C_{sp^2} atoms, the C_{sp^3} atoms of the rather long C–Si bond and two different for the C atoms in the coordinated solvent molecule. (One for secondary carbon atoms, the other for the terminal C atoms of THF). In order to stabilize the refinement, κ' for the two latter was set to values from theoretical calculations by Volkov et al.⁶¹. κ and κ' of the lithium atom was fixed to 1.20, accounting to the contraction of the valence shell in this electropositive atom.³⁵

- local symmetry:*
- 3-fold axis along the C–Si bonds for all carbon atoms,
 - 3-fold axis along the Si–N bond for the Si atom,
 - mirror planes for each carbon atom of the phenyl and the pyridyl ring,
 - 3-fold axis along the C–C bond for terminal carbon atoms in the diethyl ether molecule,
 - mirror plane for secondary carbon atoms in the diethyl ether molecule.
- similarity constraints:*
- C atoms with equivalent environment in the pyridyl ring (C5 = C3),
 - carbon atoms of the SiMe₃ group,
 - carbon atoms with the same chemical environment in the phenyl ring made up from C7-C12 (C11 = C9, C12 = C8),
 - all atoms of the phenyl ring C13-C18 to the equivalent atom of the phenyl ring C7-C12,
 - secondary carbon atoms of the diethyl ether molecule (C24 = C22),
 - terminal carbon atom of the diethyl ether molecule (C25 = C23),
 - all hydrogen atoms of the phenyl and pyridyl rings,
 - hydrogen atoms of the SiMe₃ moiety.

Using the standard procedure for the multipole refinement, several problems concerning the diethyl ether molecule and the Li atom were detected. Thus, a different strategy, consisting of three main parts, was applied:

- Part I: multipole refinement of the central part (= asymmetric unit without the coordinated diethyl ether molecule), IAM for the coordinated solvent molecule
- Part II: multipole refinement of the coordinated solvent molecule; parameters of the central part are fixed
- Part III: application of the multipole model for the whole compound

Details of Part I:

The refinement proceeded along the following sequence: first the scaling factor, then κ -refinement with fixed $\kappa(\text{H})$, P_{lm} of all atoms, P_{lm} , P_{v} , κ , for all non hydrogen atoms, κ' for all non-hydrogen atoms, coordinates and thermal parameters of the non-hydrogen atoms, all parameters together except κ' , and finally all positional and thermal parameters were refined together with the multipolar parameters (except κ') with $I > 3\sigma(I)$ and $\sin\theta/\lambda_{\text{max}} = 1.14\text{\AA}^{-1}$. In this part of the refinement P_{v} and the P_{lm} of the Li atom were always refined individually.

Details of Part II:

κ -refinement with fixed $\kappa(\text{H})$, P_{lm} of all atoms of the coordinated solvent molecule, P_{lm} , P_{v} , κ , then coordinates and thermal parameters of the non-hydrogen atoms, all parameters together except κ' , and finally all positional and thermal parameters were refined together with the multipolar parameters (except κ') with $I > 3\sigma(I)$ and $\sin\theta/\lambda_{\text{max}} = 1.14\text{\AA}^{-1}$.

Details of Part III:

All parameters together except κ' , and finally all positional and thermal parameters were refined together with the multipole parameters (except κ') with $I > 0\sigma(I)$ and $\sin\theta/\lambda_{\text{max}} = 1.14\text{\AA}^{-1}$. In this part all parameters of the Li atom are included and refined together with all the other parameters of all atoms.

Each step in all parts was refined to convergence. The scaling factor was also adjusted in each step.

The results from this refinement are excellent. Almost all DMSDAs are in the range $0.0 \cdot 10^{-3}\text{\AA}^2 - 0.9 \cdot 10^{-3}\text{\AA}^2$. Only the differences in the Si–C bonds ($1.2 \cdot 10^{-3}\text{\AA}^2 - 1.4 \cdot 10^{-3}\text{\AA}^2$) and again those in the Li–E (E = N, O) with $1.1 \cdot 10^{-3}\text{\AA}^2 - 3.1 \cdot 10^{-3}\text{\AA}^2$ exceed this range primarily due to the mass differences of the bonding partners. More crystallographic details are listed in Table 5.10; residual maps in the main molecular planes, underlining the excellent results, are depicted in Figure 5.23.

Table 5.10 Crystallographic data after multipole refinement of **VII**.

compound	V
formula	C ₂₅ H ₃₄ Li N ₂ O P Si
crystal system	triclinic
space group	P $\bar{1}$
a [Å]	10.3840(2)
b [Å]	10.4783(2)
c [Å]	12.8527(2)
α [°]	73.07(1)
β [°]	81.05(1)
γ [°]	67.66(1)
V [Å ³], Z	1235.86(4), 2
μ [mm ⁻¹]	0.18
T _{min} / T _{max} (low-batch)	0.95 / 0.99
T _{min} / T _{max} (high-batch)	0.96 / 0.99
refl. used in the multipole refinement	28161
after cut-off *	
$\sin\theta/\lambda_{\max, \text{cut}}$ [Å ⁻¹]	1.14
completeness to $\sin\theta/\lambda_{\max, \text{cut}}$ [%]	96.4
no. of unique reflections (low-angle batch) / R _{int}	5045/ 0.0246
no. of unique reflections (high-angle batch) / R _{int}	25005/ 0.0269
limiting indices	-23 ≤ h ≤ 23, -22 ≤ k ≤ 23, 0 ≤ l ≤ 29
max. shift / esd in final cycle	0.27·10 ⁻¹
R1 (I>2σ(I)) after IAM refinement to $\sin\theta/\lambda_{\max, \text{cut}}$	0.0288
wR2 (I>2σ(I)) after IAM refinement to $\sin\theta/\lambda_{\max, \text{cut}}$	0.0894
R1 (I>2σ(I)) after multipole refinement to $\sin\theta/\lambda_{\max, \text{cut}}$	0.0261
wR2 (I>2σ(I)) after multipole refinement to $\sin\theta/\lambda_{\max, \text{cut}}$	0.0298
GoF	2.31
N _{refl.} / N _{param.}	51.51

* with respect to the cut off criterion: I>0σ(I)

The multipole refinement of **VII** proofs the possibility to refine coordinated solvent molecules. In this case, it was necessary to apply a special refinement strategy, but the

results are excellent. Although the single bonds in the coordinated ether molecule allow a free rotation, all criteria for a reliable refinement are matched. Of course, the solvent molecule was not disordered in this sample, but disorder is a gradual feature without a sharp borderline. Inspection of the ADPs is the normal procedure in a structure refinement. In donating solvent molecules in the periphery of a inorganic complex they are known to be notoriously high and might indicate disorder in addition to sever libration.

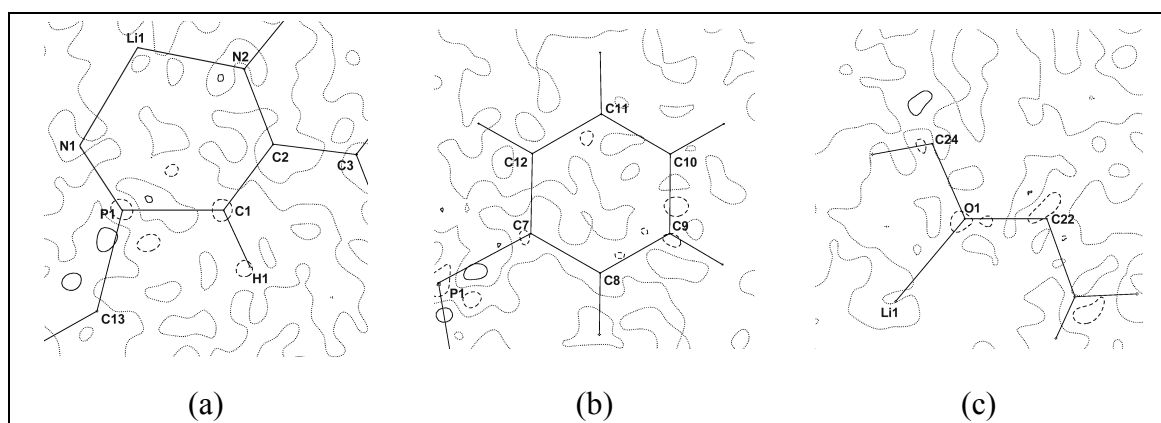


Figure 5.23 Contour plot of the residual densities after multipole refinement of **VII**, $\sin\theta/\lambda_{\max} = 1.00\text{\AA}^{-1}$. (a) P1–C1–C2 plane, (b) C7–C9–C11 plane, (c) O1–C22–C24 plane. Positive contours solid, zero-level contour dotted, negative contours dashed. Stepwidth is $0.1\text{e}\text{\AA}^{-3}$.

5.3.3 Topological Analysis

The results of the topological analysis of **VII** are presented in terms of the charge density $\rho(\mathbf{r})$, the Laplacian $\nabla^2\rho(\mathbf{r})$, the ratio of the eigenvalues $|\lambda_1|/\lambda_3$ and the charges obtained from the integration over the atomic basins along Baders theory of ‘Atoms in Molecules’.⁹ Following the examination of the Li–E bonds in **IV** and **V**, the electronic energy density H_1 is also included in the argumentation for these bonding types.

All BCPs at the P–E (E = C, N) bonds are displaced closer to the electropositive phosphorus atom. A comparison of the densities $\rho(\mathbf{r}_{\text{BCP}})$, the algebraic sum of the eigenvalues (λ_i) of the Hessian matrix, $\nabla^2\rho(\mathbf{r}_{\text{BCP}})$, of these bonds and the integrated charges are presented in Table 5.11.

Table 5.11 Topological properties at the BCP of the P–E (E = C, N), the Li–E (E = N, O) and the bonds of the C1–C2–N2 moiety in **VII**, respectively.

A–B	d(A–B)	d(A–BCP)	d(BCP–B)	$\rho(\mathbf{r}_{\text{BCP}})$	$\nabla^2\rho(\mathbf{r}_{\text{BCP}})$	$ \lambda_1 /\lambda_3$	Charge B*
P1–N1	1.5903	0.6566	0.9337	1.508(10)	5.874(28)	0.37	–1.98
P1–C1	1.7252	0.7753	0.9499	1.336(8)	–8.325(22)	1.56	–0.54
P1–C7	1.8294	0.8047	1.0248	1.134(6)	–6.402(15)	1.39	–0.31
P1–C13	1.8147	0.7784	1.0364	1.151(8)	–6.145(16)	1.25	–0.34
C1–C2	1.4023	0.6619	0.7404	2.144(14)	–17.624(54)	1.33	**
N2–C2	1.3710	0.8177	0.5533	2.296(17)	–24.656(69)	1.65	**
Li1–N1	1.9454	1.2245	0.7209	0.271(9)	4.762(17)	0.23	–1.98
Li1–N2	1.9628	1.2486	0.7142	0.203(9)	5.867(16)	0.19	–1.17
Li1–O1	1.9216	1.1913	0.7303	0.175(9)	5.239(16)	0.19	–1.36

d(A–B) is the bond path length between the atoms A and B [Å], d(A–BCP) and d(B–BCP) denote the distances of the atoms A and B from the BCP [Å], $\rho(\mathbf{r}_{\text{BCP}})$ [$\text{e}\text{\AA}^{-3}$] is the charge density and $\nabla^2\rho(\mathbf{r}_{\text{BCP}})$ [$\text{e}\text{\AA}^{-5}$] the Laplacian at the BCP, respectively. $|\lambda_1|/\lambda_3$ denotes the ratio between the highest charge concentration perpendicular and the charge depletion along this vector at the BCP, respectively. The charges [e] are from the integration over the atomic basins.* Charge of the phosphorus atom (atom A in the first four lines): +2.20; * Charge of the lithium atom (atom A in the last three lines): +0.87.** Not calculated.

The properties at the BCPs of the aromatic carbon bonds in the phenyl rings as well as those of the SiMe₃ group are in the expected range.^{8,107} The two topologically analyzed P–C_{phenyl} bonds in **VII** are comparable to those in the triphenylphosphane donor molecule of a transition metal complex.¹⁴⁵ Different to the P–C_{phenyl} bonds in triphenylphosphonium benzylide Ph₃P=C(H)Ph, no variance in the topology between the two P–C_{phenyl} in **VII** could be observed.¹³ Compared to the latter the P–C1 bond displays higher charge density and a more negative Laplacian at the BCP. An inspection of the Laplacian along the P–C bond paths (Figure 5.24 (a)) in **VII** reveals an almost equal charge distribution in the phosphorus basin, while the main difference of the Laplacian in the basin of the carbon atoms is related to the shorter distance between C1 and the BCP_{P–C1}. This rather short P–C bond results from distinct electrostatic interactions between the negatively polarized deprotonated C1 and the electropositive phosphorus atom reflected by the charge of –0.52e for C1 and +2.20e for P after integration over the atomic basins.

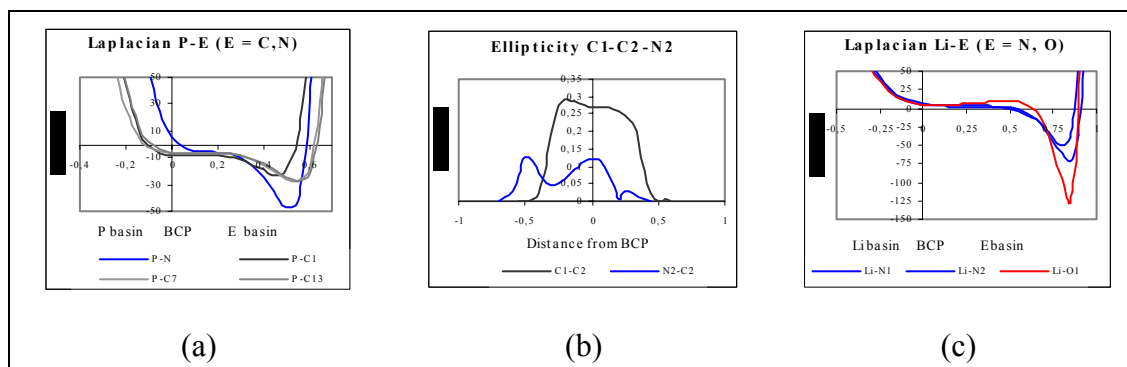


Figure 5.24 (a) and (c) denote the Laplacian $\nabla^2\rho(\mathbf{r})$ [$\text{e}\text{\AA}^{-5}$] along the bond paths [\AA] of the P–E (E = C, N) and the Li–E (E = N, O) bonds, respectively; (b) shows the ellipticities ϵ along the bond paths of the C1–C2–N2 residue. The zero value of the x-axis indicates the position of the BCP.

The Laplacian distribution $\nabla^2\rho(\mathbf{r})$ along the P–N1 bond is completely different to the P– C_{ipso} bonds. The Laplacian at the BCP is positive and charge density is exclusively concentrated in the nitrogen basin (Figure 5.24(a)). The ratio of the eigenvalues λ_1 and λ_3 underline the different charge distributions. Both properties indicate a severe contribution of electrostatic interaction to the P1–N1 bonding. This is further substantiated by the integration over the atomic basins. The two basins related to the nitrogen atoms give distinct negative values. The imino nitrogen atom N1 is bonded to three electropositive neighbours and therefore the charge of -1.91e is higher than -1.11e for the ring nitrogen atom N2. The charge of the deprotonated carbon atom C1 is about 0.2e higher than those of the two phosphorus bonded phenyl *ipso* carbon atoms (C7: -0.30e , C13: -0.34e). All these findings give rise to a ylide $\text{P}^+\text{--C}^-$ bond simultaneously to a $\text{P}^+\text{--N}^-$ bond not yet presented in the resonance forms of Scheme 1.3, depicted in the introduction.

The topological properties of the exocyclic C1–C2 bond (Table 5.11), which are almost the same as an aromatic C–C bond⁸ as well as the aromatic character of the C2–N2 bond of the pyridine ring fuels the idea of a delocalization of the negative charge over the C1–C2–N2 residue. This exocyclic delocalization slightly perturbs the aromaticity of the heteroaromatic ring. The bond lengths and electron densities in the pyridyl substituent differ from those in undisturbed rings.¹¹⁶ Together with the ellipticity along the bond paths of these two bonds, C1–C2 and N2–C2, which show significant ellipticities in the bonding regions for both bonds (Figure 5.24(b)), one has to draw the conclusion that the negative charge from the deprotonation of C1 is obviously coupled into the ring over the C1–C2–N2 residue rather than to the phosphorus atom. The Laplacian distribution and the shape of the basins in the plane of the metallacycle are given in Figure 5.25. From this figure it is clearly visible, that each atom in the

heterocycle assigns a individual charge distribution and a unique silhouette, respectively.

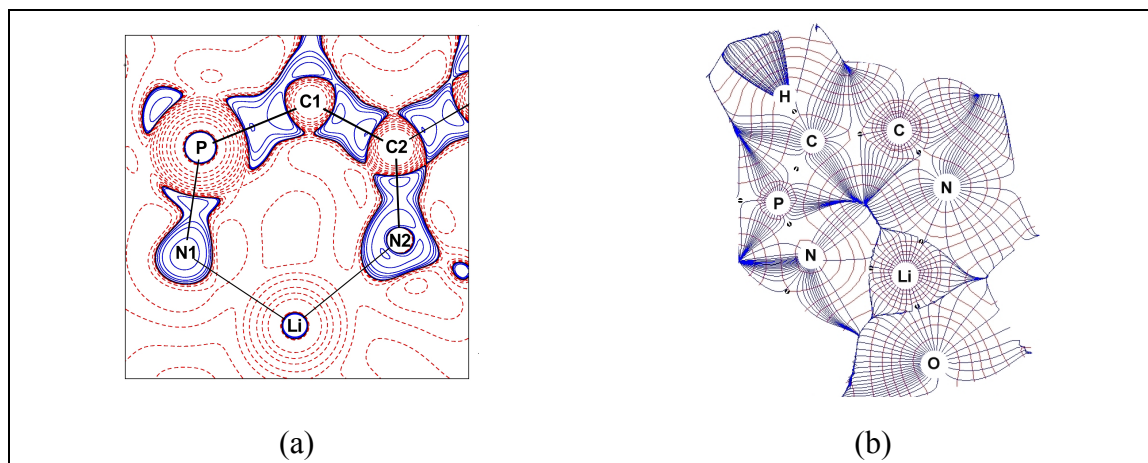


Figure 5.25 Laplacian (a) and a two dimensional trajectory plot in a plane of the six-membered metallacycle (b) in **VII**; positive values of $\nabla^2\rho(\mathbf{r})$ in (a) are depicted by red, negative by blue lines; contours drawn at $0.000, \pm 2.0 \cdot 10^n, \pm 4.0 \cdot 10^n, \pm 8.0 \cdot 10^n \text{ e}\text{\AA}^{-5}$, where $n = 0, \pm 1, \pm 2, \pm 3$; (b) visualises the different shape and size of the atomic basins; red lines denote electron density, blue lines are trajectories of the electron density; bond paths and BCPs are black.

The determination of the (3;-3) critical points in the spatial distribution of $-\nabla^2\rho(\mathbf{r})$ and quantification of the VSCCs around the electronegative atoms (N1, N2, O1, C1) confirm this view. Isosurface presentations around N1 and O1 and contour plots in the planes containing the (3;-3) critical points are presented in Figure 5.26. They indicate sp^3 hybridization at N1 and O1 with two lone-pairs each, both oriented towards the Li cation. Due to participation in the aromatic pyridyle system, only three VSCCs could be determined for N2. The angles LP1–N1–LP2 and LP1–O1–LP2 between the lone-pair maxima of 77.1° and 72.0° , respectively, are much more acute than the expected ideal 109° , but can be rationalized by the narrowing of the critical points by simultaneous interaction to the Li cation. Obviously, the lone-pairs at N1 and O1 act as a bifurcated donor to the electropositive metal acceptor. We found the same arrangement at S-bonded sp^3 -nitrogen atoms in an intramolecular hydrogen bond.¹¹

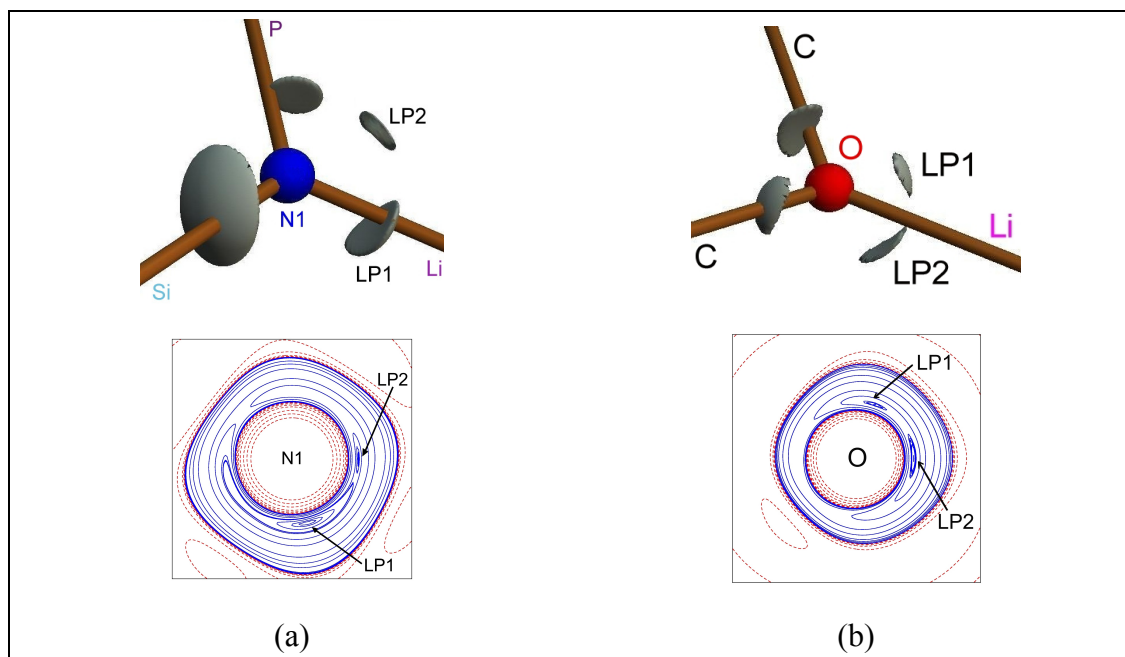


Figure 5.26 Isosurface maps at constant $\nabla^2\rho(\mathbf{r})$ values indicating bonding and non-bonding charge concentrations around the displayed atoms and contour plots in a plane with the two lone-pairs oriented towards Li1 for N1 (a) and O1 (b) in **VII**; (a) N1, $\nabla^2\rho(\mathbf{r}) = -48\text{e}\text{\AA}^{-5}$ (bonding-) and $-41\text{e}\text{\AA}^{-5}$ (non-bonding VSCCs); (b) O1, $\nabla^2\rho(\mathbf{r}) = -125\text{e}\text{\AA}^{-5}$ (bonding-) and $-105\text{e}\text{\AA}^{-5}$ (non-bonding VSCCs). Blue contours indicate charge concentration, red contours charge depletion, respectively.

The Laplacian along the bond path (Figure 5.24(c)), as well as the ratio $|\lambda_1|/\lambda_3$ and the electronic energy density, indicate absolute dominating ionic interaction for all Li–E (E = N, O) bonds in **VII**. A very low amount of electron density, no charge concentrations, monitored *via* positive values of $\nabla^2\rho(\mathbf{r})$ in the area next to the BCP, and ratios of $|\lambda_1|/\lambda_3$ below 0.25 emphasise this argumentation. The integration over the atomic basins reveals an almost unpopulated valence shell for Li1 and distinct negative charges for all electronegative atoms in the environment of the lithium cation (Table 5.11). Finally, the electronic energy density, H_i , is slightly positive for all Li–E bonds in **VII**, further validating almost pure ionic interaction. A detailed compilation of the H_i values and other properties of the metal–non-metal bonds are presented in chapter 5.6.

5.3.4 Molecular Properties from the Charge Density Distribution

The isosurface representation of the static deformation density and a contour plot of this property in the plane of the metallacycle reveal the larger amount of electron density in the C1–C2–N2-backbone, where the negative charge is delocalized. Furthermore, a huge amount of density, with a banana-like shape, is located in the lone-pair region of O1. The orientation of the lone-pairs from N1 and N2 are also clearly visible in Figure 5.27.

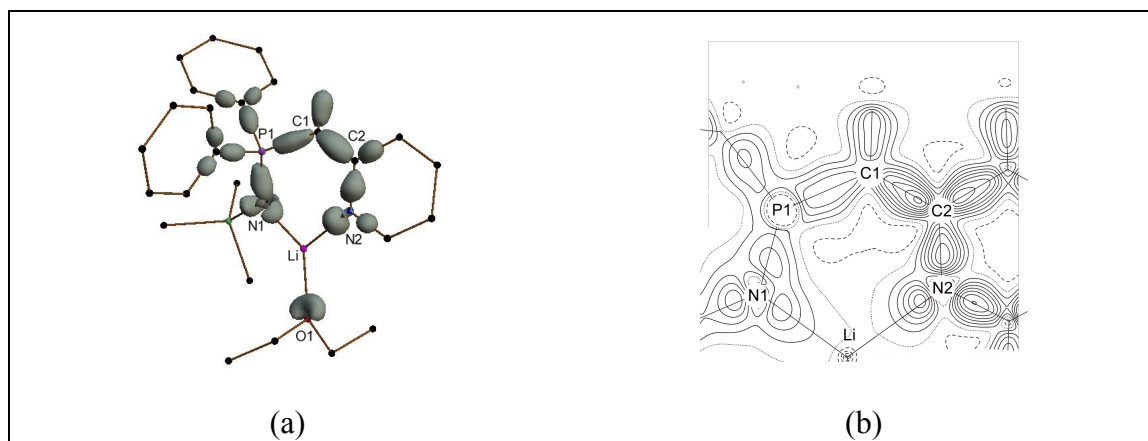
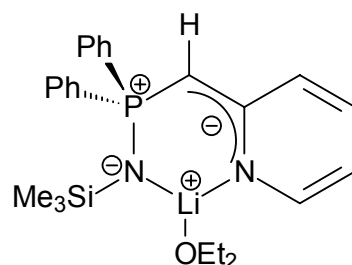


Figure 5.27 Isosurface representation (a) and contour plot (b) of the static deformation density in **VII**. For clarity reasons, in (a) only the isosurface of the metallacycle, the P–E (E = C, N) and the Li–E (E = N, O) bonds are drawn, respectively. The isosurface is plotted at the $0.25\text{e}\text{\AA}^{-3}$ level. Hydrogen atoms but H1 are also omitted for clarity. In (b), only the contours in the plane of the heterocycle are drawn. Positive contours solid, zero contour dotted, negative contours dashed; stepwidth is $0.1\text{e}\text{\AA}^{-3}$.

In conclusion, the experimental charge density distribution in $[(\text{Et}_2\text{O})\text{Li}\{\text{Ph}_2\text{P}(\text{CHPy})\text{-(NSiMe}_3)\}]$, **VII**, clearly proves, that the formal $\text{P}=\text{N}$ imino double bond and the potential ylenic $\text{P}=\text{C}$ double bond have to be formulated as polar P^+-N^- and P^+-C^- single bonds augmented by electrostatic contributions not by $\text{p}\pi\text{--d}\pi$ double bonding. As predicted from calculations,¹² hypervalent phosphorus is not required to describe the bonding – in other words: hypervalency, $\text{P}=\text{N}$ and $\text{P}=\text{C}$ double bonding can be ruled out. None of the canonical formulae given in the introduction gives a correct description of the bonding situation in **VII**. It is much more appropriate to assign charges in the resonance formula. According to the results of the topological analysis, the formula depicted in Scheme 5.2 contributes most to describe the bonding in **VII**; the polar single bonds correspond best with the reactivity.



Scheme 5.2 Lewis structure of **VII**, which describes according to the results of the topological analysis from experimental data the bonding best.

All Li–E (E = N, O) contacts in **VII** are close to purely ionic interactions. Very low total electron densities and positive Laplacians together with an electronic energy density that equals zero suggest only negligible covalent augmentation.

5.4 Comparison of E–N (E = Al, Si, P, S) Bonds

An examination of the charge density distribution *via* a detailed topological analysis and calculation of several density related properties of the Al–N, Si–N and the P–N bonds in inorganic compounds was given in the previous paragraphs of this thesis. The S–N bonding type was studied in our research group earlier. The results of this bonding type are taken from the PhD thesis of D. Leusser.¹⁰

The aim of this chapter is to deduce trends in the electronic properties, especially in the Laplacian distribution, the topological values at the BCP and the electronic energy density for both atoms of each bond, the electropositive element of the third row and the electronegative from the second row. Therefore the Al–N contacts in **V**, the deprotonated Si–N bonds in **IV**, the P–N bond of **VII** and the shortest S–N bond of the methylene-bis(triimido)sulfonic acid, $[\text{CH}_2\{\text{S}(\text{N}^t\text{Bu})_2(\text{NH}^t\text{Bu})\}_2]$,¹¹ are employed. In all these bonds, the third-row element is in the highest possible oxidation state. The series includes non-metals bonded to nitrogen from group 16 and 15, with silicon, group 14, an element often termed semimetal, and one metal from group 13. From this point of view differences in the charge density distributions of these E–N bonds should be remarkable.

Table 5.12 Topological properties of the E–N (E = Al, Si, P, S) bonds at the BCP.

A–B	d(A–B)	d(A–BCP)	d(BCP–B)	$\rho(\mathbf{r}_{\text{BCP}})$	$\nabla^2\rho(\mathbf{r}_{\text{BCP}})$	$ \lambda_1 /\lambda_3$	H_1
Al–N	1.8843	0.8140	1.0703	0.619(6)	7.000(10)	0.25	- 0.029
Si–N	1.6821	0.7319	0.9502	1.140(8)	9.146(7)	0.30	- 0.091
P–N	1.5903	0.6566	0.9337	1.508(10)	5.874(28)	0.37	- 0.216
S–N	1.5205	0.7184	0.8021	2.376(30)	-16.445(90)	1.33	- 0.442*

$d(\text{A–B})$ is the bond path length between the atoms A and B [\AA], $d(\text{A–BCP})$ and $d(\text{B–BCP})$ denote the distances of the atoms A and B from the BCP [\AA], $\rho(\mathbf{r}_{\text{BCP}})$ [$\text{e}\text{\AA}^{-3}$] is the charge density and $\nabla^2\rho(\mathbf{r}_{\text{BCP}})$ [$\text{e}\text{\AA}^{-5}$] the Laplacian at the BCP, respectively. H_1 is the electronic energy density [au] at the BCP. * Values from a sulfur–imido–nitrogen bond in sulfurdiimide^{10,146}, as the values from the present compound are not accessible due to program limitations.

An obvious common feature of all four species is the existence of at least one lone-pair at the nitrogen atom. One question is where the lone-pair densities are located. It can be seen from the analysis of the charge density distribution that the localization indeed needs special care. While the lone-pair densities at the nitrogen atoms in the Si–N and

Al–N bonds are rather distorted, and partially redistributed to the bond, this density is more pronounced, forming more distinct maxima for E–N with $E = P, S$. The two latter bonds are often formulated as double bonds because the bond length is much shorter than for a typical single bond. However, the charge density distribution clearly reveals sp^3 hybridization for the N atoms in these bonds. Hence, the P–N and the S–N bonds in these structures should be formulated as single bonds shortened from strong electrostatic interactions. In tetracoordinated aluminium and silicon compounds, the Al–N and Si–N bonds are not described as double bonds, the debate on these two bonding types is focused on the degree of ionic contribution. A comparison of the Laplacian distribution along the bond paths for all four bonding types and the topological properties at the BCPs are given in Figure 5.28 and Table 5.12, respectively.

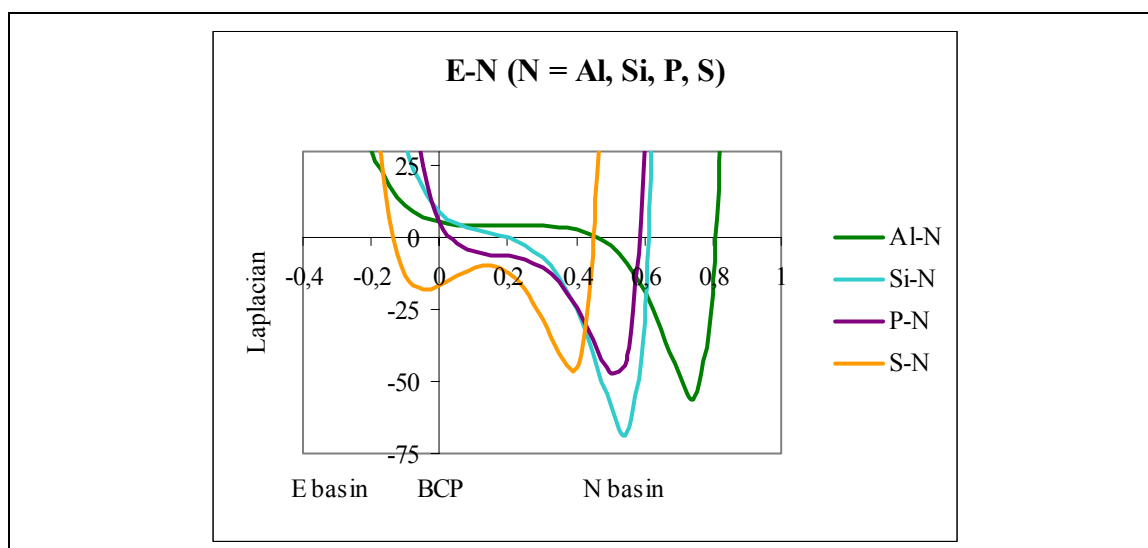


Figure 5.28 Laplacian [$e\text{\AA}^{-5}$] along the bond path of the E–N ($E = \text{Al}, \text{Si}, \text{P}, \text{S}$) bonds of the discussed compounds. The zero value of the x-axis [\AA] indicates the position of the BCP.

These shape of the Laplacian and the topological properties show some evident trends. All BCPs are located close to the electropositive atom. The length of the bond path increases from the bonds containing the non-metals *via* the semimetal to the metal–nitrogen bond. The short bonds of S and P are not only caused from the small radius of these atoms but from strong electrostatic interactions between two atoms with a large difference concerning the electronegativity. Deprotonation of the nitrogen atom results in additional electrostatic contributions. The Al–N interaction exhibits the longest bond path, although the Al^{3+} cation is relatively small.

The lowest amount of total electron density $\rho(\mathbf{r})$ is found at the BCP of the Al–N bond, the highest at the BCP of the S–N bond. However, the topological analysis revealed

redistribution of charge from the lone-pairs to the E–N bonding vectors for Si–N and to a small extend for S–N. A similar tendency is visible for the Laplacian. While charge is concentrated near the nitrogen atoms in all cases, the situation is different in the bonding region. Concerning the Al–N bond, charge is depleted in this area. The same is valid for the silicon–nitrogen bond, with a reduced range of charge depletion. A more positive value of $\nabla^2\rho(\mathbf{r})$ at the BCP for Si–N bond does not necessarily indicate the highest charge depletion in the entire bonding region as deducible from Figure 5.28. The charge concentration in the P–N bond is still limited to the nitrogen basin. Different to the former three bonding types, the Laplacian at the BCP is negative for the S–N bond. Furthermore, this bond is the only one with charge concentrations in the bonding region of the third-row element basin.

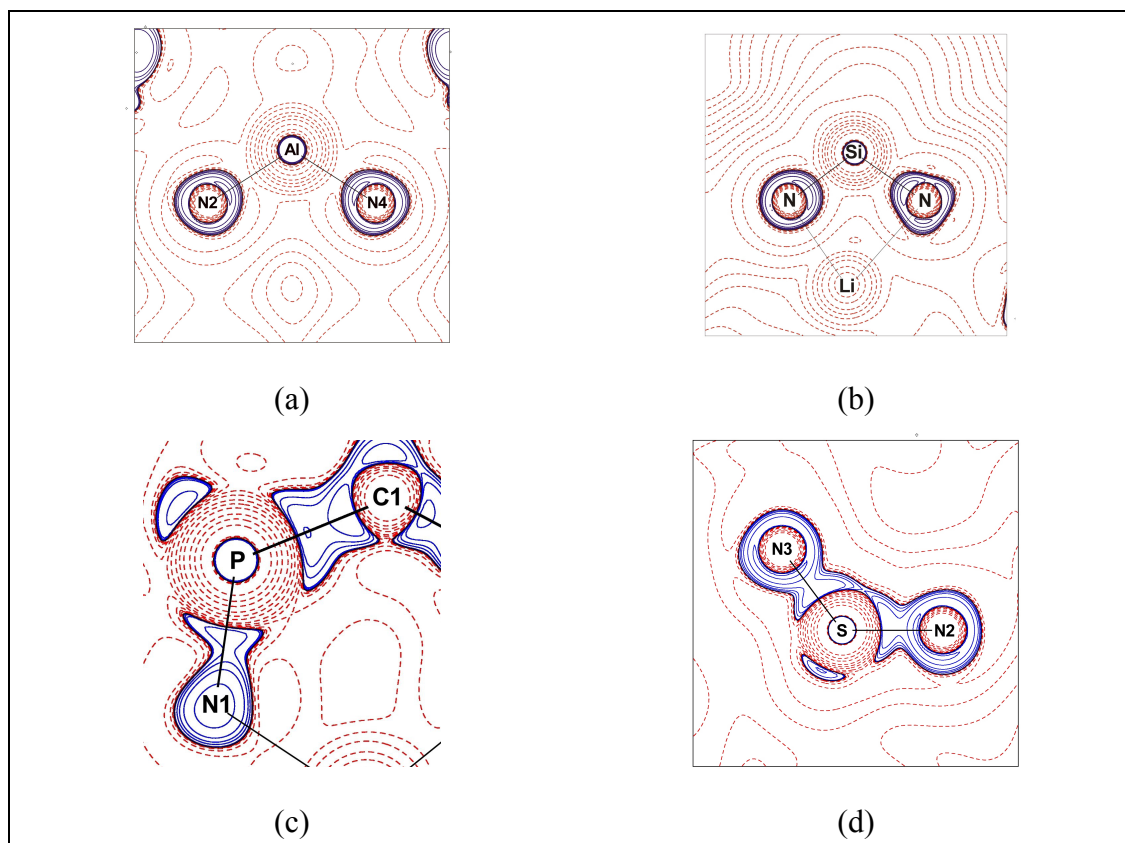


Figure 5.29 Contour plots of the Laplacian distribution in the N2–Al1–N4 plane of **V** (a), the N1–Si1–N4 plane of **IV** (b), the N1–P1–C1 plane of **VII** (c) and the N2–S1–N3 plane of the methylene-bis(trimido)sulfonic acid (d). Blue lines indicate charge concentration, red lines charge depletion. Contours drawn at $0.000, \pm 2.0 \cdot 10^n, \pm 4.0 \cdot 10^n, \pm 8.0 \cdot 10^n \text{ e}\text{\AA}^{-5}$, where $n = 0, -3, \pm 1, \pm 2$.

The Laplacian distribution in a plane enclosing the E and N atom support the findings from the distribution along the bond path. Planes with Al–N and S–N bonds, clearly demonstrating the differences in the charge distribution, are given in Figure 5.29.

Whereas the distribution around the nitrogen atom in the Al–N bond is almost atomic-like and the areas with charge concentration are located exclusively in the nitrogen basin, charge is concentrated along the entire bonding region of the S–N bond. The former suggests a strong domination of ionic contribution, the latter a significant covalent contribution to the bonding.

The ratios of the eigenvalues $|\lambda_1|/\lambda_3$, manifest the different electronic situations. The smallest ratio is calculated for Al–N, followed from Si–N and P–N; all ratios are remarkable below unity. In contrast, the value calculated for the S–N bond is above unity. The electronic energy density H_1 emphasizes this ranking. Although the energy is not accessible for the S–N bond of the present compound, calculation of H_1 in the S–N bond of another, comparable sample¹⁴⁶ strongly emphasizes this trend. It reveals a marginally negative value for Al–N, a low negative value for Si–N and distinct negative energies for the P–N and the S–N bonds.

Taking all these electronic properties into account, it is evident that the Al–N interaction exhibits the highest amount of ionic contribution with only small covalent augmentation. Ionic interaction also is the dominant force in the Si–N bonds investigated within this comparison. The topological analysis of the present P–N bond suggests a covalent single bond with distinct ionic contribution. Within this series, the bonding type with the highest amount of covalent character is the S–N bond. Although distinct covalent contribution are present in P^+-N^- and dominating in S^+-N^- , Lewis formulae with double bonds for these two bonding types are not justified due to the sp^3 character of the nitrogen bonds, ascertained from the topological analysis. Qualitatively, this trend for the series of four E–N (E = Al, Si, P, S) bonding types is predictable from the electronegativity, but a quantification is only possible from detailed a topological analysis.

5.5 Charge Density Study on *tert*-Butyllithium·(–)-Sparteine

tert-Butyllithium (*t*Buli) is one of the most important organolithium reagents. Like other organolithium species, this compound shows a high tendency towards aggregation.¹¹⁴ Therefore, attempts to synthesize and isolate monomeric *t*Buli failed so-far. Even the use of coordinating solvents did not result in monomeric structures. *t*Buli crystallizes from *n*-pentane as tetramers, in the presence of coordinating compounds as dimers, respectively.¹⁴⁷ However, a non-aggregated lithium species is of great importance as in most cases, the monomer is believed to be the rate-determining species in lithium organic chemistry. Recently, Strohmman et al. reported the first structurally

characterized monomeric *t*Buli compound, enclosing the chiral (-)-sparteine ligand: [*t*Buli·(-)-sparteine], **VIII**.³⁷

The Li–C contact in **VIII** is analyzed in detail to compare the electronic features of this bond to other Li–E (E = N, O) bonds in this thesis. Investigations of the Li–N interactions with the properties derived from other samples discussed above serve as standard.

5.5.1 Molecular Structure

Compound **VIII** crystallizes in the chiral monoclinic space group C2, the asymmetric unit contains one molecule. The solid-state structure of **VIII** is depicted in Figure 5.30.

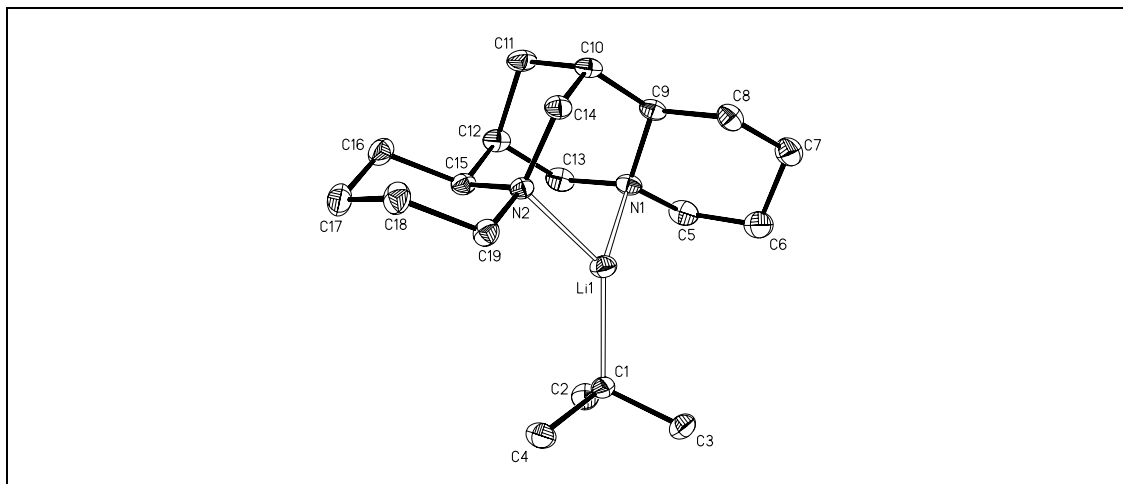


Figure 5.30 Solid-state structure of **VIII**. Hydrogen atoms are omitted for clarity. The anisotropic displacement parameters are depicted at the 50% probability level.

The conformation of the (-)-sparteine ligand is equal to those in other solid-state structures containing this moiety.¹⁴⁸ The (-)-sparteine ligand is sterically rather demanding, enclosing 15 sp^3 carbon atoms and two nitrogen atoms in the same hybridization state. The latter coordinate one lithium cation, forming a distorted six-membered metallacycle. Li is displaced 0.38 Å from a plane of the three atoms coordinating the metal. Furthermore, the sum of the angles around lithium equals 349.3° indicating partial tetrahedral environment around the lithium cation. Nevertheless, only three atoms are coordinated to Li and the coordination sphere is rather distorted. The N1–Li–N2 angle is solely 89.5° while both N–Li–C1 angles are close to 130°. In addition, the angle between a line connecting Li and C1 of the *tert*-butyl group and the N1–N2–Li-plane is only 25.4°. For the moment, the reason for this angular distortion, also found in theoretical calculations for this compound³⁷ remains unclear. Possibly, the charge density distribution provides an answer for the non-planar environment of

lithium. The chiral, bulky (–)-sparteine ligand shields the lithium centre. Hence, the coordination of additional ligands is hindered. Due to the non-planar environment of the lithium cation, one hemisphere of the lithium cation is completely shielded while the opposite side reveals a small area accessible for a potential nucleophile. Both Li–N bonds are almost equal in lengths (Li1–N1 = 2.0641(12) Å, Li1–N2 = 2.0687(12) Å). The Li–C contact of 2.1141(12) Å is at the short end of the range covered by this bonding type.¹¹⁴

Further elucidation of the Li–E (E = C, N) bonds and effects of the non-planar environment for the reactivity are limited to experimental charge density studies.

5.5.2 Multipole Refinement

The populations of the atoms bonded to lithium (C1, N1, N2) were refined to hexadecapolar level, the multipole populations of all other non-hydrogen atoms to the octapolar level. For the hydrogen atoms solely a bond-directed dipole population was included in the refinement. The lithium atom was treated spherically. Radial screening factors (κ and κ') were introduced and refined for each atom type. For three types of carbon atoms (the carbon atom bonded to the lithium cation, carbon as a part of sparteine and the methyl groups) different sets of κ and κ' values were refined. The expansion/contraction factors for Li were set to 1.20, taking a slight contraction of this atom into account, and kept fixed during the refinement. Reflections to $\sin\theta/\lambda_{\max} = 1.00 \text{ \AA}^{-1}$ with $I > 3(\sigma)I$ were included in the refinement. In the first step of the multipole refinement the U_{ij} and positional parameters of the non-hydrogen atoms were adjusted with reflections $\sin\theta/\lambda = 0.7 - 0.85 \text{ \AA}^{-1}$. In all following steps the molecule was treated as a rigid body. The other steps of the refinement followed the standard procedure with one exception described in detail below.

The following list contains additional constraints imposed to reduce the number of parameters:

- local symmetry:*
- three-fold axis along C1–C bond for the carbon atoms C2–C4 of the *tert*-butyl group,
 - mirror planes for all methylene carbon atoms of the sparteine ligand (C5–C8, C11, C13, C14, C16–C19).
- Similarity constraints:*
- *tert*-butyl carbon atoms (C3, C4 = C2),
 - C12 = C10,
 - all hydrogen atoms of the *tert*-butyl group,

- all hydrogen atoms of the sparteine ligand.

The DMSDA test reveals an excellent deconvolution of the electron density from thermal motion. All DMSDAs of the homonuclear bonds and the heteronuclear C–N bonds are between $0.0 \cdot 10^{-3} \text{Å}^2$ – $0.8 \cdot 10^{-3} \text{Å}^2$. Again, only the DMSDAs in the Li–E (E = C, N) with $1.2 \cdot 10^{-3} \text{Å}^2$ – $2.5 \cdot 10^{-3} \text{Å}^2$ exceed this range due to the mass differences of the bonded atoms.

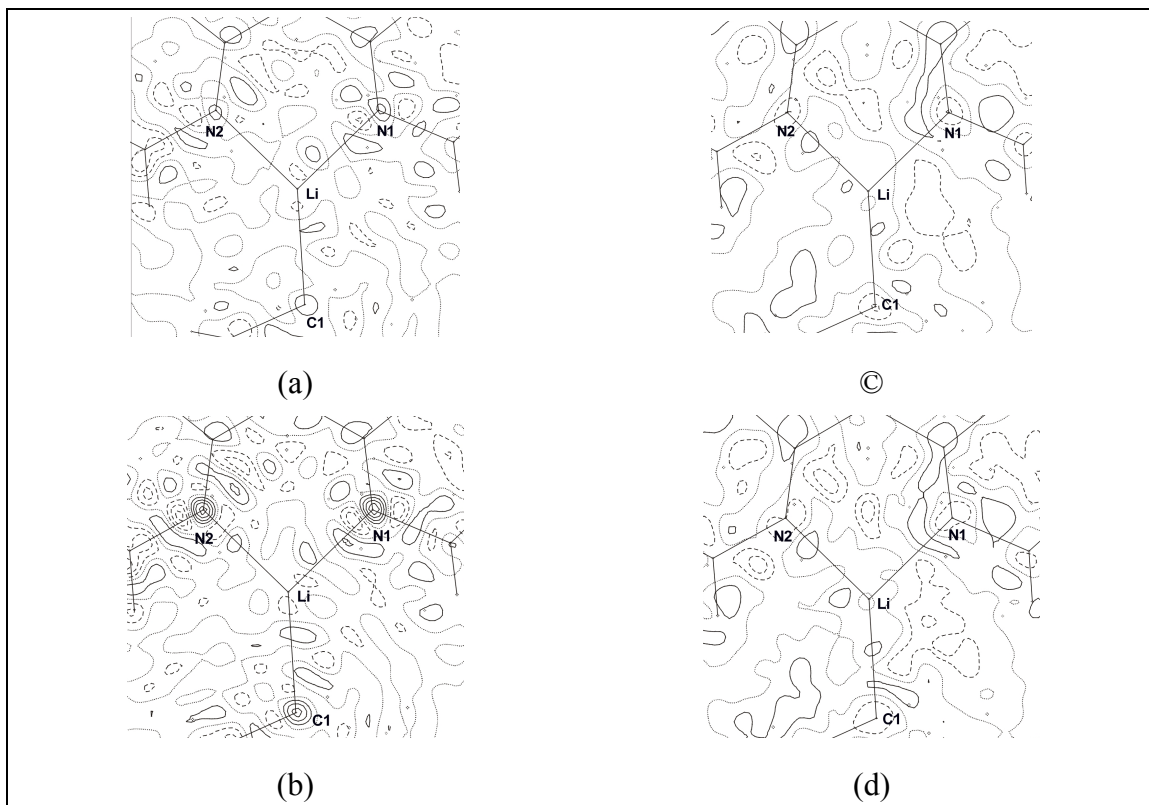


Figure 5.31 Contour plots of the residual densities after multipole refinement of **VIII** in the N1–N2–C1 plane. (a) and (b) show the residual densities with $\sin\theta/\lambda_{\max} = 0.85 \text{Å}^{-1}$ and $\sin\theta/\lambda_{\max} = 1.00 \text{Å}^{-1}$, respectively, without adjustment of the weighting scheme, (c) and (d) the same plane and the same resolutions with the adjusted weighting scheme. Positive contours solid, zero contour dotted, negative contours dashed. Stepwidth is 0.1eÅ^{-3} .

Despite the very good results of the DMSDA test the residual maps revealed significant residual densities at the atomic positions. As can be seen from Figure 5.31(a) the residual map is featureless to a resolution of $\sin\theta/\lambda_{\max} = 0.85 \text{Å}^{-1}$. However, including reflections from higher diffraction angles, the residual densities increase rapidly (Figure 5.31 (b)). Different models were tried during the refinement, but none of the final residual maps was featureless. As explained in chapter 3.3.2 statistical weights are used during standard multipole refinement. At the beginning, this weighting scheme was applied for the refinement of **VIII**, always resulting in significant residual densities at

atomic positions arising from the weak intensities of the reflections at the highest diffraction angles despite very long exposure times (300s per frame) for the high-angle batch. The data files from the integration of the high-angle batch show an extremely high background for the shells with the smallest lattice distances leading to underestimated intensities. However, reflections up to $\sin\theta/\lambda_{\max} = 1.00\text{\AA}^{-1}$ should be included in the refinement in order to get a satisfying data/parameter ratio and to achieve convergence.

Therefore it was necessary to introduce a scaling factor for the reflections with lower intensities. The weighting scheme implemented in the least square procedure of the XD program package is identical with that used in SHELXL:⁷⁹

$$w = 1 / [\sigma^2(F_{\text{obs}}^2) + (aP)^2 + bP]$$

where $P = [2F_{\text{calc}}^2 + \text{Max}(F_{\text{obs}}^2, 0)] / 3$. The variable a mainly influences the shells with reflections of high intensities, while b largely scales shells with a majority of reflections with middle and weak intensities. The standard procedure with $a, b = 0$, leads to the weighting scheme described in 3.3.1.

In the refinement of **VIII**, the variable b was adjusted at the end of the refinement; variable a was not changed. Results of this refinement are depicted in Figure 5.31 (c) and (d).

This strategy leads to a featureless residual map. The DMSDAs did not change within this procedure due to treatment of the molecule as rigid body. This proceeding displays the importance of any parameter in the refinement in a impressive way. Automatical adjustment of almost all parameters, as possible in recent standard refinement software does not enlight systematical problems of the data and can therefore lead to shortcomings in the density model.

Table 5.13 Crystallographic data after multipole refinement of **VIII**.

compound	V
formula	C ₁₉ H ₃₅ LiN ₂
crystal system	Monoclinic
space group	C2
a [Å]	181.1087(6)
b [Å]	9.3773(3)
c [Å]	12.2350(4)
α [°]	90
β [°]	119.4350(10)
γ [°]	90
V [Å ³], Z	1809.44(10), 4
μ [mm ⁻¹]	0.06
T _{min} / T _{max} (low-batch)	0.94 / 0.99
T _{min} / T _{max} (high-batch)	0.95 / 0.99
refl.used in the multipole refinement	11161
after cut-off *	
sinθ/λ _{max, cut} [Å ⁻¹]	1.00
completeness to sinθ / λ _{max, cut} [%]	96.1
no. of unique reflections	3716
(low-angle batch) / R _{int}	0.0350
no. of unique reflections	15331
(high-angle batch) / R _{int}	0.0537
limiting indices	-40 ≤ h ≤ 34, -20 ≤ k ≤ 20, 0 ≤ l ≤ 27
max. shift / esd in final cycle	0.15·10 ⁻¹
Flack X parameter ⁹⁵	0.5(7)
R1 (I>2σ(I)) after IAM refinement	0.0496
to sinθ/λ _{max, cut}	
wR2 (I>2σ(I)) after IAM refinement	0.1088
to sinθ/λ _{max, cut}	
R1 (I>2σ(I)) after multipole refinement	0.0324
to sinθ/λ _{max, cut}	
wR2 (I>2σ(I)) after multipole refinement	0.0532
to sinθ/λ _{max, cut}	
GoF	5.08
N _{refl.} / N _{param.}	33.12

* with respect to the cut off criteria: I>3σ(I) and sinθ/λ_{max} = 1.00

5.5.3 Topological Analysis

The topological properties of all carbon–carbon bonds are in the expected range. The same is true for the N–C bonds.⁸ At the BCP, the Li–E (E = C, N) bonds in **VIII** adopt values for almost pure electrostatic interactions (Table 5.14). The electron densities are below $0.2\text{e}\text{\AA}^{-3}$ for all bonds, the Laplacian at the BCPs is slightly positive and the ratio $|\lambda_1/\lambda_3|$ is in the range of 0.17–0.20. Moreover, all Li–E bonds show a positive electronic energy density H_i . The differences of the topological properties at the BCPs between Li–C and Li–N are relatively small; values for the Laplacian, $\nabla^2\rho(\mathbf{r})$ and the total electron densities, $\rho(\mathbf{r})$, are almost identical.

Table 5.14 Topological properties of the Li–E (E = C, N) bonds in **VIII** at the BCP.

A–B	d(A–B)	d(A–BCP)	d(BCP–B)	$\rho(\mathbf{r}_{\text{BCP}})$	$\nabla^2\rho(\mathbf{r}_{\text{BCP}})$	Charge B*	$ \lambda_1/\lambda_3 $	H_i
Li–N1	2.0647	0.7410	1.3237	0.196(5)	4.362(3)	-1.56	0.17	+0.007
Li–N2	2.0717	0.7480	1.3238	0.186(4)	4.125(3)	-1.61	0.18	+0.007
Li–C1	2.1147	0.7498	1.3648	0.197(10)	3.667(7)	-0.52	0.20	+0.005

$d(\text{A–B})$ is the bond path length between the atoms A and B [\AA], $d(\text{A–BCP})$ and $d(\text{B–BCP})$ denote the distances of the atoms A and B from the BCP [\AA], $\rho(\mathbf{r}_{\text{BCP}})$ [$\text{e}\text{\AA}^{-3}$] is the charge density and $\nabla^2\rho(\mathbf{r}_{\text{BCP}})$ [$\text{e}\text{\AA}^{-5}$] the Laplacian at the BCP, respectively. Charges [e] from the integration over atomic basins. * Charge of Li (atom A): +0.71e. H_i is the electronic energy density [au] at the BCP.

Inspection of the Laplacian in the bonding region reveals almost identical distributions for the two Li–N bonds. The Laplacian is about zero in an interval of 0.5\AA and charge is solely concentrated near the atomic positions.

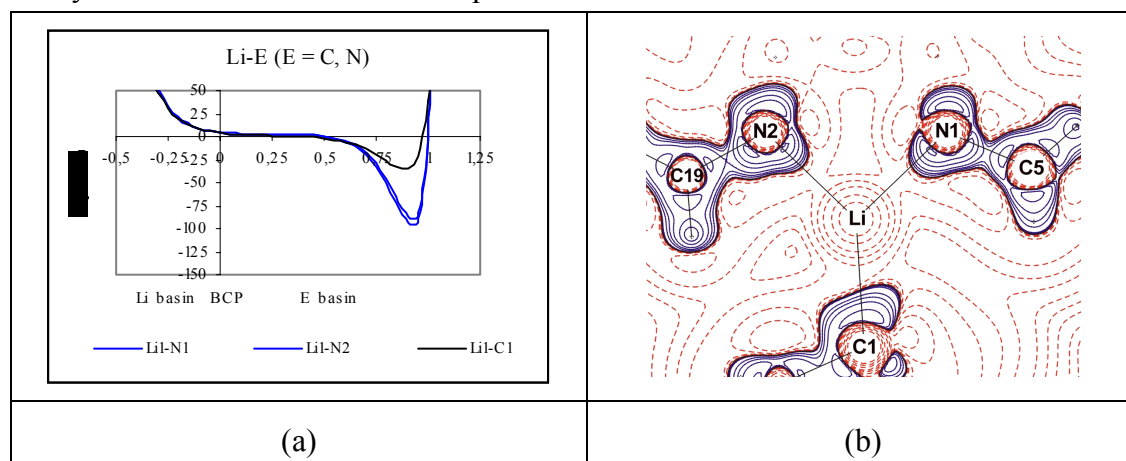


Figure 5.32 (a) Laplacian along the bond bath of the Li–E (E = C, N) bonds in **VIII**. The zero value of the x-axis indicates the position of the BCP; (b) Contour plots of the Laplacian distribution in the N1–N2–C1 plane of **VIII**. Blue lines indicate charge concentration, red lines charge depletion. Contours drawn at $0.000, \pm 2.0 \cdot 10^n, \pm 4.0 \cdot 10^n, \pm 8.0 \cdot 10^n \text{e}\text{\AA}^{-5}$, where $n = 0, -3, \pm 1, \pm 2$.

The course of the Laplacian of Li–C1 is almost identical in the bonding region while the charge concentration at the carbon atom is much lower (Figure 5.32 (a)). The Laplacian distribution in Figure 5.32 (b) displays distorted shapes at the lone-pairs of all three donating atoms. Especially the lone-pair of C1 exhibits a distinct deformation towards another carbon atom of the *tert*-butyl group.

A more detailed picture is given from the inspection of the VSCCs at the atoms coordinating the lithium cation. Searches for the maxima in the VSCCs revealed four maxima for C1, N1 and N2. The VSCCs show maxima around $-50\text{e}\text{\AA}^{-5}$ for the nitrogen atoms and $-13\text{e}\text{\AA}^{-5}$ for C1, respectively and are to a certain extent distorted. At high isosurface levels the four maxima in the valence shells of these three atoms are clearly visible (Figure 5.33) proving sp^3 hybridization for C1, N1 and N2.

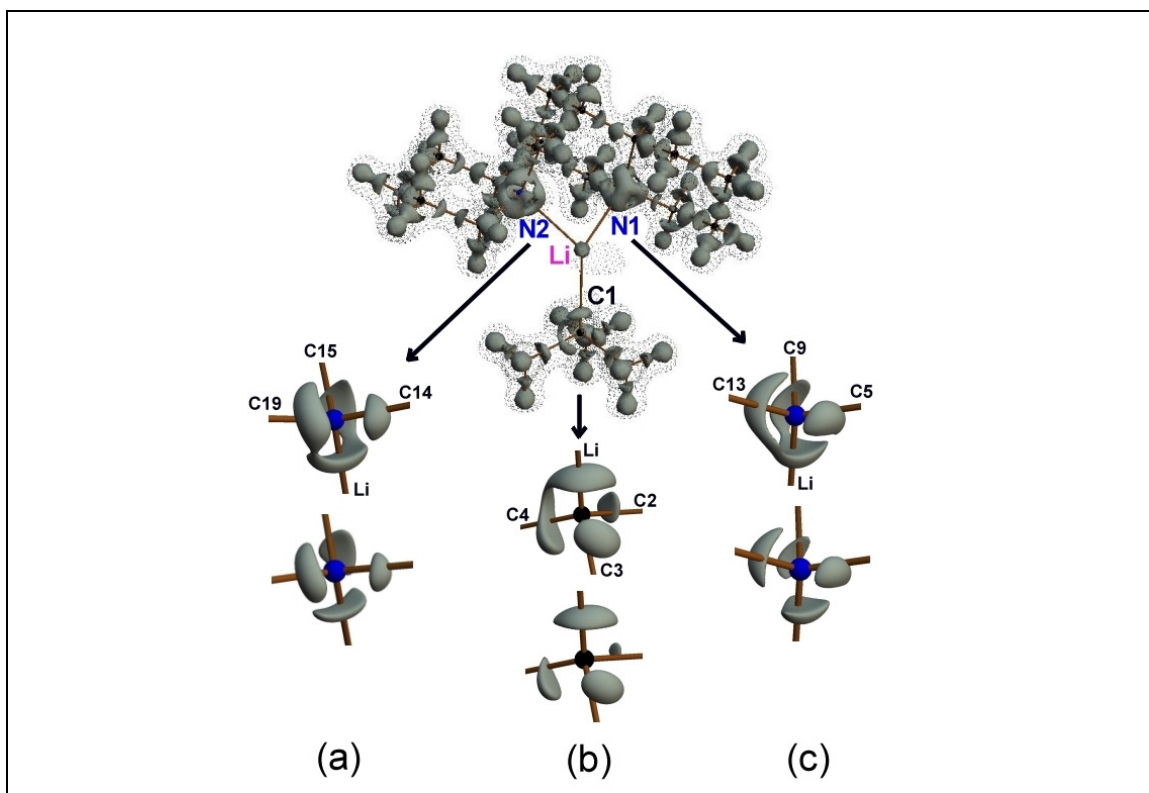


Figure 5.33 Isosurface maps at constant $\nabla^2\rho(\mathbf{r})$ values of **VIII**. The isosurfaces for the whole molecule are drawn at the $15\text{e}\text{\AA}^{-5}$ (gray) and $0\text{e}\text{\AA}^{-5}$ (dotted), respectively. The Laplacian of the C–C bonds displays the typical charge concentrations for non-polar covalent bonds. The isosurfaces of the atoms coordinating lithium are highlighted. The upper line (first value) shows lower levels with slightly smeared VSCCs, the lower line (second value) higher levels with four distinct VSCCs oriented towards the neighbouring atoms; (a) N2, $\nabla^2\rho(\mathbf{r}) = -49$ and $-58\text{e}\text{\AA}^{-5}$; (b) C1, $\nabla^2\rho(\mathbf{r}) = -18$, $-23\text{e}\text{\AA}^{-5}$; (c) N1, $\nabla^2\rho(\mathbf{r}) = -51$, $-64\text{e}\text{\AA}^{-5}$.

This situation is different to the VSCCs of the nitrogen atoms in the Si–N bonds of **III-V**, where the VSCCs are distorted at all levels. A slight distortion is particularly visible for N1–C13 and N2–C15. An inspection of the Laplacian in the bonding regions of all N–C bonds reveals the asymmetric distribution for polar bonds, less pronounced for the two quoted bonds above (Figure 5.34 (a)). Furthermore, these two bonds assign a higher total electron density at the BCPs than the other N–C bonds. In the butyl moiety, the weak polarity of the C1–C bonds, arising from the metallation is reduced *via* charge redistribution in C1–C3 and C1–C4. This is represented in the ellipticities ϵ of these two bonds (Figure 5.34 (c)).¹¹⁶ However, the redistribution of charge is too small to result in a significant shortening of the bond.

Integration over atomic basins resulted in distinct negative charges for N1 and N2. The charges for both atoms are almost equal (Table 5.14). This underlines together with the other properties quoted above the equal bonding situation for both nitrogen atoms. The charge of C1 is $-0.52e$, while the integrated charge of the lithium basin ($+0.70e$) hints to a very small amount of charge transfer towards the cation.

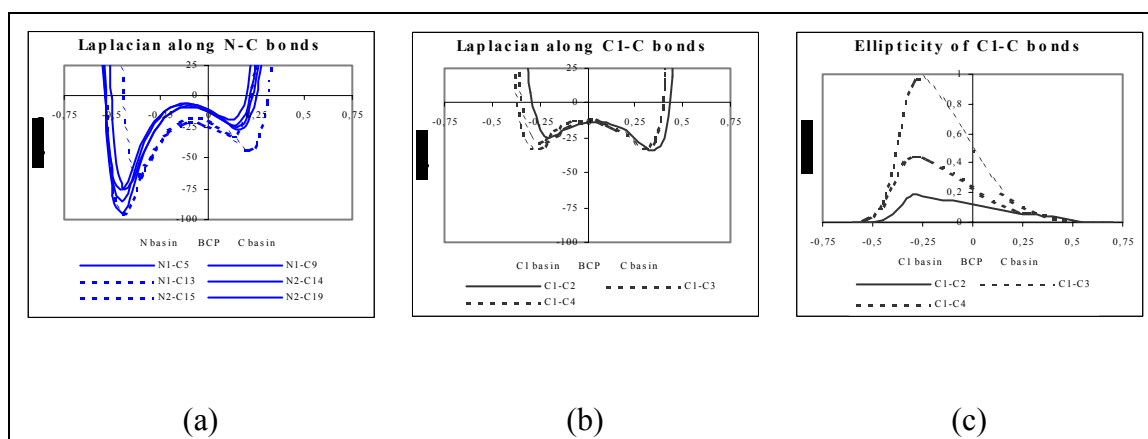


Figure 5.34 Laplacian [$e\text{\AA}^{-5}$] along the bond paths in (a) N–C bonds in the sparteine ligand and (b) C1–C bonds of the butyl moiety of **VIII**; (c) ellipticity of the C1–C bonds in the butyl moiety. The zero value of the x-axis [\AA] indicates the position of the BCP.

The monomeric *t*Buli(–)-sparteine encloses non-polar covalent C–C and polar covalent N–C bonds in the (–)-sparteine ligand. The analysis of the charge density distribution elucidates almost pure ionic interactions for the Li–E (E = C, N) bonds. The differences between the Li–C and Li–N bonds in the bonding regions and concerning the properties calculated from values at the BCPs turned out to be very small, whereas the charge concentrations in the valence shell of the nitrogen atoms are much higher than of C1.

5.5.4 Molecular Properties from the Charge Density Distribution

The non-planar environment of the lithium cation leads to a small area for potential additional coordination. A space filling model of the crystal structure clearly shows this free coordination site.³⁷ A nucleophilic reagent, potentially coordinating at the lithium centre is attracted from regions with a positive ESP. The ESP, associated to the long range coulomb force, determines the route, potential reagents approach the molecule. Figure 5.35 displays, that the less covered coordination site at Li is indeed attractive for additional coordination of a nucleophile. The area around the lithium center, not covered from the sparteine ligand assigns no negative ESP. The negative potential is limited to the covered site and the centre of the sparteine ligand. Therefore, the lack of an additional ligand is uniquely referred to the steric requirements of the bulky ligand.

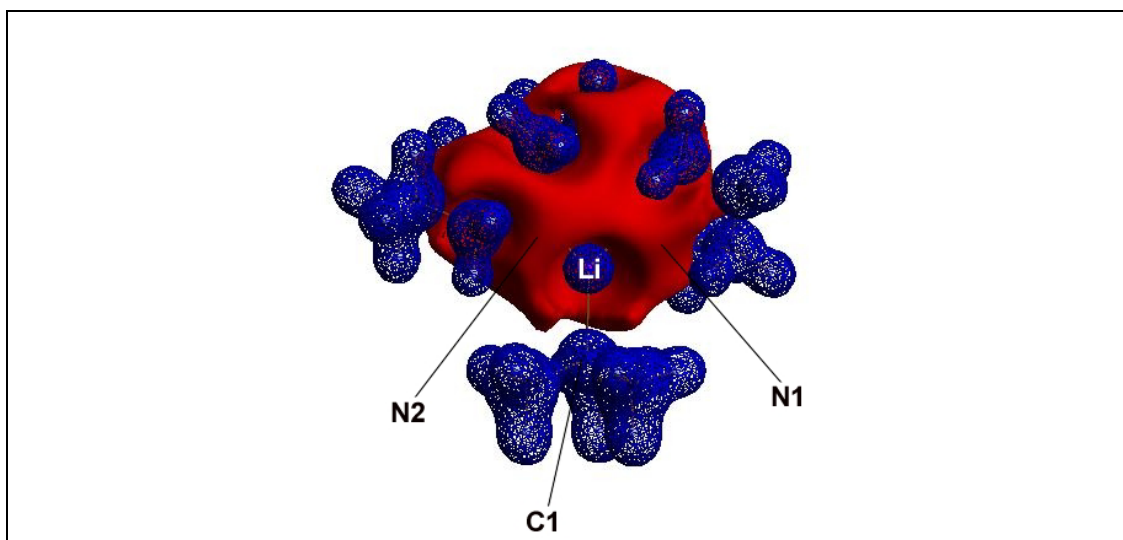


Figure 5.35 Electrostatic potential of **VIII**. Areas with negative potential are red, those with positive ESP are depicted in blue; isosurfaces are drawn at the $\pm 0.35\text{e}\text{\AA}^{-3}$ level.

The topological analysis subsequent to a multipole refinement allows a clear classification of the Li–E (E = C, N) bonds in **VIII** as ionic bonds with only marginal covalent contributions. The ESP, calculated from the multipole parameters, manifests that the accessible area at the lithium centre is not only sterically but also electronically suited for additional coordination of an incoming ligand. In addition small deviations of the C–C bonds from standard C–C single bonds are evident in the *tert*-butyl moiety.

5.6 Comparison of Li–E (E = C, N, O) Bonds

Several Li–E (E = C, N, O) bonds have been discussed in the previous chapters. A comparison of all these bonds in the compounds **IV**, **V**, **VII** and **VIII** should lead to a more general interpretation of the interactions in these bonding types.

All lithium cations investigated in this thesis are coordinated from three atoms, with the exception of Li2 in **IV** which reveals a fourth, relatively long and weak, contact to the nitrogen atom N4. While the studied Li–N contacts of 1.9297 Å – 2.3945 Å cover a wide range, the length differences for the Li–O bonds are only 5 pm (1.8906 Å – 1.9428 Å). In addition, one Li–C bond was studied (2.1147 Å). Although these lengths differences, the ratio Li–BCP/E–BCP is almost identical for all bonds of one bonding type (Table 5.15). Even the very long Li2–N4 bond in **IV** fits in this pattern. The distances of the more electronegative atoms to the BCPs are much larger than those of Li–BCP in any case. The average ratio Li–BCP/E–BCP for Li–O is 0.62 and 0.58 for Li–N. In the Li–C bond this ratio is 0.55. This finding differs from the situation in the investigated Si–N bonds. The Si–N bond in **VI** is about 25 pm longer than those in **III–V**, but the Si–BCP distance is similar in both bonds. It is only the N–BCP distance which increases drastically in **VI**, leading to completely different ratios.

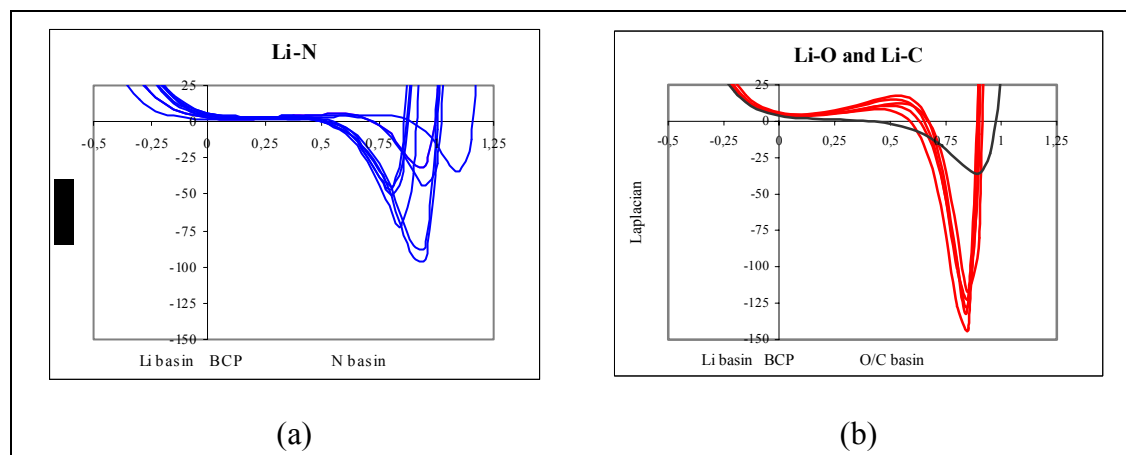


Figure 5.36 Laplacian [$\text{e}\text{\AA}^{-5}$] along the bond path of the Li–N (a), Li–O and Li–C (b) bonds. The zero value of the x-axis [\AA] indicates the position of the BCP.

The same agreement is found for the ratio of the largest contraction of electron density perpendicular to the bonding vector at the BCP, λ_1 , and the depletion parallel to the bond path at this point, λ_3 . This ratio is between 0.14 and 0.19 for all Li–O and Li–N bonds. In the Li–C bond this property has a value of 0.20. The similar bonding situation is furthermore reflected by the calculated electronic energy densities of the Li–E bonds:

they are all slightly positive. The Laplacian at the BCP is also positive in all Li–E bonds, the values are between $+1.308(1)\text{e}\text{\AA}^{-5}$ and $+6.028(3)\text{e}\text{\AA}^{-5}$.

All these findings suggest comparable bonding situations and dominating forces for the Li–E bonds. A more detailed inspection of the Laplacian is necessary to verify or falsify this. While there are no striking differences in the interatomic region concerning the Laplacian along the bond path of the Li–N bonds and in the lithium basin, there are discrepancies in the area closer to the location of the nitrogen core. The Laplacian is flat and close to zero in a range of 0.5\AA starting from the BCP towards the nitrogen core. In the lithium basin, distinct positive values of the Laplacian indicate severe charge depletion. Near the atomic coordinates of nitrogen, the charge concentration in the valence shell clusters around $-50\text{e}\text{\AA}^{-5}$ for most of the N atoms. The charge concentrations of the pyridyle nitrogen atom ($\approx -75\text{e}\text{\AA}^{-5}$) in **VII** and the two nitrogen atoms in **VIII** ($\approx -100\text{e}\text{\AA}^{-5}$) are more pronounced (Figure 5.36 (a)). The highest charge concentrations are located in the valence shell of the oxygen atoms (Figure 5.36 (b)). The Laplacian distribution is equal for all studied Li–O bonds, with oxygen donors from THF and diethyl ether moieties. Compared to the curvatures of the Li–N bonds, the charge depletion in the bonding region is more prominent in the Li–O bonds. The course of the Laplacian is not flat, but the charge depletion slightly increases from the BCP to the oxygen core before the Laplacian changes rapidly to negative values in the proximity of the atomic position. The Laplacian along the bond path of the Li–C bond is close to zero in the bonding region of the carbon basin; the charge depletion changes smoothly to charge accumulations towards the atomic core (Figure 5.36 (c)).

The VSCCs around the nitrogen atoms in **IV** and **V** are depicted in Figure 5.9 chapter 5.2.1.3. Distinct maxima are missing towards the lithium cation. The VSCCs at the nitrogen atom of the P–N bond in **VII** display two maxima (bifurcated donor) towards the lithium atom (Figure 5.26 in chapter 5.3.3) - one close to the bonding vector, the second oriented towards Li, but shifted apart from the bond path. This separation in two maxima leads to a lower maximum charge concentration towards the metal compared to the second N atom in this sample, assigning only one maximum towards Li due to its participation in the pyridyle ring. The highest maxima are found for the two nitrogen atoms of the sparteine ligand. Both atoms reveal one distinct maximum towards the Li cation (Figure 5.33).

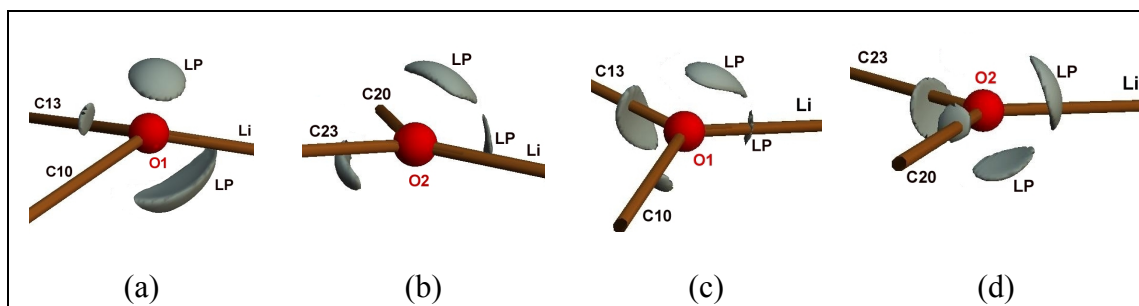


Figure 5.37 Isosurface representation at constant values of the Laplacian $\nabla^2\rho(\mathbf{r})$ around the oxygen atoms in **IV** and **V**, indicating bonding and non-bonding VSCCs. The isosurfaces are plotted at the following levels [$\text{e}\text{\AA}^{-5}$]; (a): O1 in **IV**; $\nabla^2\rho(\mathbf{r}) = -125\text{e}\text{\AA}^{-5}$ (the maximum on the O1–C10 bond vanished at the chosen level); (b): O2 in **IV**; $\nabla^2\rho(\mathbf{r}) = -150\text{e}\text{\AA}^{-5}$ (the maximum on the O2–C20 bond vanished at the chosen level); (c): O1 in **V**; $\nabla^2\rho(\mathbf{r}) = -110\text{e}\text{\AA}^{-5}$ (bonding-) and $-135\text{e}\text{\AA}^{-5}$ (non-bonding VSCCs); (d): O2 in **V**; $\nabla^2\rho(\mathbf{r}) = -90\text{e}\text{\AA}^{-5}$ (bonding-) and $-125\text{e}\text{\AA}^{-5}$ (non-bonding VSCCs).

All oxygen atoms coordinating lithium cations assign two additional O–C_{sp3} single bonds. The identical Laplacian distribution reflects similar donor properties. Two charge concentrations, oriented towards lithium are clearly resolved at each atom. It is remarkable, that these two maxima are also visible in the proximity of atoms belonging to the disordered moieties further underlining the successful refinement of the THF moieties in **IV**. As already pointed out for some N donors, one of these maxima is approximately on the bonding vector, the other forms in any case an angle about 70° with this vector and is oriented in the same direction. Angles in this range are always found between two lone-pairs in our research group if both lone-pairs act as a donor.¹¹ Figure 5.37 displays the VSCCs around the oxygen atoms of **IV** and **V**; the VSCCs of the O atom in **VII** are depicted in Figure 5.26.

The integrated charges of the lithium cations in **IV**, **V**, **VII** and **VIII** reveal only small deviations (+0.71e to +0.87e); all suggest a very low amount of charge transfer from the donor atoms to the lithium cation. Furthermore, these equal charges manifest a proper refinement of Li in all compounds, although different models were used in the various multipole refinements. Li was refined aspherically with multipole populations to the octapolar level in **VII**, while it was treated spherically in **IV**, **V** and **VIII**.

All inspected electronic properties, not far from those determined for NaCl,¹²¹ reveal practically pure ionic bonding for the studied Li–E (E = C, N, O) bonds:

- very low amount of total electron density at the BCPs,
- positive Laplacian in the entire bonding regions,
- the ratio $|\lambda_1|/\lambda_3$ much below unity,
- positive electronic energy densities at the BCPs and

- very small charge transfer towards the lithium cations.

The donor atoms in **VII**, involved in two covalent single bonds (together with the interaction to the lithium acceptor) act as bifurcated donors. This is concluded from the existence of two maxima in the valence shell oriented towards Li. For the N-donors of this type in the Si₄N₄ heterocycles of **IV** and **V** these findings can not be validated due to the smeared VSCCs. All other investigated donors (involved in aromatic bonds or bonded to three other atoms) show only one maximum towards the lithium cation.

Table 5.15 Topological properties of NaCl⁹ and the Li–E (E = C, N, O) bonds in **IV**, **V**, **VII** and **VIII** at BCP.

A–B	compound	d(A–B)	d(A–BCP)/ d(B–BCP)	$\rho(\mathbf{r}_{\text{BCP}})$	$\nabla^2\rho(\mathbf{r}_{\text{BCP}})$	$ \lambda_1 /\lambda_3$	H _i
Na ⁺ Cl [–] *		*	*	0.242	4.830	*	+0.047
<u>Li–O</u>							
Li1–O1	IV	1.9428	0.62	0.184(4)	4.674(3)	0.17	**
Li1–O2	IV	1.9257	0.63	0.169(5)	5.022(4)	0.15	**
Li1–O1	V	1.8906	0.61	0.224(4)	6.028(3)	0.17	+0.011
Li1–O2	V	1.9116	0.62	0.190(4)	5.317(3)	0.14	+0.011
Li1–O1	VII	1.9216	0.61	0.175(9)	5.239(16)	0.18	+0.012
<u>Li–N</u>							
Li1–N3	IV	1.9446	0.59	0.235(2)	5.352(2)	0.17	**
Li2–N1	IV	2.1421	0.59	0.134(2)	2.721(2)	0.15	**
Li2– N1A	IV	2.1003	0.58	0.165(1)	3.322(1)	0.15	**
Li2–N3	IV	2.1641	0.58	0.129(2)	2.747(1)	0.15	**
Li2–N4	IV	2.3945	0.58	0.086(2)	1.308(1)	0.14	**
Li1–N3	V	1.9297	0.59	0.238(2)	5.525(1)	0.16	+0.008
Li1–N1	VII	1.9454	0.59	0.271(9)	4.762(17)	0.23	+0.003
Li1–N2	VII	1.9628	0.57	0.203(9)	5.867(16)	0.19	+0.012
Li1–N1	VIII	2.0647	0.56	0.196(5)	4.362(3)	0.17	+0.007
Li1–N2	VIII	2.0717	0.57	0.186(4)	4.125(3)	0.18	+0.007
<u>Li–C</u>							
Li1–C1	VIII	2.1147	0.55	0.197(10)	3.667(7)	0.20	+0.005

d(A–B) is the bond path length between the atoms A and B [Å], d(A–BCP)/d(B–BCP) denote the ratio of the distances from atoms A and B to the BCP, $\rho(\mathbf{r}_{\text{BCP}})$ [eÅ^{–3}] is the charge density and $\nabla^2\rho(\mathbf{r}_{\text{BCP}})$ [eÅ^{–5}] the Laplacian at the BCP, respectively. H_i is the electronic energy density [au] at the BCP. * esds and missing values are not given in literature; ** not accessible due to program limitations.

The differences in the electronic properties of these three bonding types are only small. From the on average highest positive Laplacian for the Li–O bonds together with the slightly smaller ratio of $|\lambda_1|/\lambda_3$ as well as the more pronounced charge concentrations in the valence shell the strongest electrostatic forces can be deduced for this bonding type.

6 Conclusion

Within the scope of this work, eight high resolution X-ray data sets were measured at low temperatures. The measurement and processing of the data followed a procedure developed in our lab. All data sets were evaluated using the multipole formalism, which allows an accurate determination of the electron density distribution in a crystal.

The main aim of this work was the classification of highly polar E–N (E = Al, Si, P) and Li–E' (E' = C, N, O) bonds in terms of ionic (closed-shell) or covalent (shared) interactions. To answer this question the experimentally determined electron density was analyzed using Bader's theory of 'Atoms in Molecules' (AIM). This allows a quantitative evaluation of properties derived from the electron density $\rho(\mathbf{r})$, such as the Laplacian $\nabla^2\rho(\mathbf{r})$, the ellipticity ε and the ratio of the highest charge concentration perpendicular to the bond path, λ_1 , to the largest charge depletion along the bonding vector, λ_3 . Most of these properties were monitored along the entire bonding region and not limited to the BCP as in former studies. The analyses are completed by the calculation of the electronic energy densities H_1 at the BCPs and the integration of atomic basins also defined within the AIM theory. The electrostatic potential (ESP) was computed from the multipole parameters to reveal preferred reactive sites of the structures under investigation. Apart from that, the multipole formalism was applied to problematic crystal structures in order to open this method for twinned samples or those including disordered groups in the molecule.

Methodical Development

The proper multipole refinement and subsequent topological analysis of the twinned structure **I** revealed the opportunity to handle problematic samples with the aspherical atom approach. Further studies of disordered moieties in **IV** were also successful but demonstrated the limits of the method. According to the obtained results, refinement of disordered *rigid groups*, like phenyl moieties, is possible including a variety of constraints in the least-squares procedure. As long as two parts of the disorder assign almost exactly the same geometry, the multipole populations are transferable. *Conformational unstable* moieties like THF remain problematic. Due to the free rotation about single bonds, often leading to two deviating geometries for the two parts, it is difficult to transfer the multipole parameters from one fragment to another.

Therefore, inspection and comparison of the geometry in both parts in advance of the multipole refinement is obligate for a proper treatment of the disordered section.

Classification of E–N (E = Al, Si, P) Bonds

All these bonding types contain one electropositive third-row element and an electronegative nitrogen atom. Hence, the electronic properties of these bonds show some similarities. However, the detailed inspection of the properties derived from the electron density distribution allows a clear separation. A positive Laplacian, found in the entire bonding region of the studied Al–N and Si–N bonds, suggests ionic domination. The atomic-like Laplacian distribution and the ratio $|\lambda_1|/\lambda_3$ underline the assumption of dominating ionic interaction in the Al–N bonds of **V**. The amount of electron density at the BCP and a slightly negative value of the electronic energy density yield a small covalent augmentation in this type. Ionic interaction is the dominating force in the Si–N bonds of **III–V**. The more negative electronic energy density together with a higher amount of electron density hint to an increased covalent attribute.

The studies on a dative N→Si bond in the hexacoordinated organosilicon compound **VI** display significant differences to the Si–N bonds in **III–V**. The electron density on the bonding vector of the former type is halved compared to the latter, the electronic energy density equals zero and the $|\lambda_1|/\lambda_3$ ratio of 0.2 is much below one. All these features together with the positive Laplacian in the bonding region indicate absolute ionic domination in the dative N→Si bond; the covalent contributions are very small with regard to the properties from experimental X-ray data. These findings together with a high ionic character of the Si–O and Si–F bonds in **VII** lead to the conclusion that the hexacoordinated silicon atom should not be classified as hypervalent.

The topological analyses of the P–N bond in the lithiated picolylphosphane **VII** suggest a covalent single bond strengthened by electrostatic contributions. The charge concentrations in the bonding region of the P–N bond are still limited to the nitrogen basin, while the electronic energy density, as well as the prominent electron density at the BCP, are typical for polar covalent single bonds.

Moreover, the determination of four maxima in the valence shell of the phosphorus bonded nitrogen atom of **VII** proves sp^3 -character. Thus, the formulation of a P=N bond, arising from merely bond length considerations, and leading to the assumption of valence expansion at the phosphorus atom is not justified and consequently, hypervalency for the phosphorus atom in **VII** can be ruled out.

Classification of Li–E' (E' = C, N, O) Bonds

The results of the topological analyses in these three metal–non-metal bonding types allow a straightforward interpretation of the interactions: they are almost purely ionic. The covalent augmentation, if any, is negligible. The differences between the electronic properties of the investigated Li–C, Li–N and Li–O bonds are rather small. However, the highest charge concentrations at the oxygen atoms suggest the strongest electrostatic forces for this type. Any of the evaluated properties suggests closed-shell interactions. The Laplacian as well as the electronic energy densities are positive, the ratio $|\lambda_1|/\lambda_3$ is below 0.21 in all Li–E bonds and the total electron density at the BCP clusters around $0.2\text{e}\text{\AA}^{-3}$ – all these topological properties are not far from those determined for NaCl.

In addition, the charges from the integration of the lithium basins in **IV**, **V**, **VII** and **VIII** hint to a very low charge transfer towards the lithium cations in all samples.

Charge density studies are a powerful tool to elucidate the bonding situation even in highly polar bonds far beyond bond lengths and angles considerations. The results of topological analyses based on low-temperature high-resolution X-ray data yield information for an exact classification of all studied highly polar bonds - ionic contributions turned out to be dominating in almost all cases. Careful proceeding allowed to adopt the multipole model even for problematic structures.

Prospects

Experimental charge density studies including third-row elements are still rare in the literature. The same is valid for metal–non-metal bonds. Topological analyses of twinned or disordered samples are missing. Therefore, more detailed investigations of highly polar bonds in terms of Bader's AIM theory are necessary to generalize the findings of this thesis. Additional knowledge, provided from other studies, about compounds enclosing disordered areas is required to open this field for 'real' rather than 'ideal' crystals because lots of chemists deal with crystals including disordered moieties, located especially in the periphery of the molecules.

Adopting the multipole model exclusively to ideal model compounds definitively belongs to the past. Recent and future studies have to evaluate the charge density distribution in chemically relevant compounds.

7 Zusammenfassung

Im Rahmen dieser Arbeit wurden acht hochaufgelöste Tieftemperaturdatensätze mit Röntgenbeugungsmethoden gemessen. Die verwendete Strategie zur Datensammlung, ebenso wie die Methode zur Datenreduktion, sind weitgehend in unserem Arbeitskreis entwickelt worden. Um die Elektronendichteverteilung im Kristall möglichst genau zu bestimmen, wurden alle Datensätze mit dem Multipolformalismus ausgewertet.

Die zentrale Fragestellung der Arbeit war die Klassifizierung der stark polaren Bindungen E–N (E = Al, Si, P) sowie Li–E' (E' = C, N, O) im Hinblick auf ionische und kovalente Wechselwirkungen. Um diese Frage zu beantworten wurde die experimentell bestimmte Elektronendichte mit der ‚Atoms in Molecules‘ Theorie von Bader analysiert. Sie ermöglicht eine quantitative Auswertung von Eigenschaften wie dem Laplacian $\nabla^2\rho(\mathbf{r})$, der Elliptizität ε oder dem Verhältnis der Eigenwerte $|\lambda_1|/\lambda_3$, die aus der Elektronendichte $\rho(\mathbf{r})$ erhalten werden. Die meisten dieser elektronischen Eigenschaften wurden entlang des gesamten Bindungspfad untersucht; die Analyse war nicht, wie in früheren Arbeiten auf die bindungskritischen Punkte (BCPs) beschränkt. Die Untersuchungen wurden durch die Berechnung der Energiedichte H_1 am BCP und die Integration der atomaren Basins vervollständigt. Weiterhin wurde aus den Multipolpopulationen das Elektrostatische Potential bestimmt, um reaktive Zentren der untersuchten Verbindungen zu quantifizieren. Das Multipolmodell wurde auch auf Kristalle mit problematischer Elektronendichteverteilung angewendet, um die Methode für verzwilligte Kristalle bzw. solche mit fehlgeordneten Gruppen zu erschließen.

Methodische Weiterentwicklung

Die erfolgreiche Multipolverfeinerung mit anschließender topologischer Analyse der im Kristall verzwilligten Verbindung **I** zeigt die Anwendbarkeit eines Atommodells, das asphärische Anteile einschließt, auf Verbindungen mit problematischer Elektronendichteverteilung. Weitere Untersuchungen an fehlgeordneten Gruppen in der Verbindung **IV** waren ebenso erfolgreich, stießen aber an die Grenzen der Methode. Gemäß der erhaltenen Ergebnisse ist die Verfeinerung von *starr* Gruppen wie Phenylringen möglich, sofern viele Constraints bei der Strukturverfeinerung vorgegeben werden. Zeigen die zwei Teile der fehlgeordneten Gruppen eine fast identische Geometrie, sind die Multipolparameter von einem Teil auf den anderen übertragbar. Bei

Gruppen mit *flexibler Konformation* wie THF ist die Anwendung allerdings problematisch. Aufgrund der freien Drehbarkeit um Einfachbindungen, die oft zu unterschiedlichen Geometrien der zwei Gruppen einer Fehlordnung führt, ist es kritisch, die Multipolparameter von einem Fragment auf das andere zu übertragen. Daher sind eine genaue Bestimmung und ein Vergleich der Geometrien beider Gruppen der Fehlordnung unerlässlich, um das Multipolmodell erfolgreich auf den betroffenen Teil einer Verbindung anzuwenden.

Klassifizierung der E–N (E = Al, Si, P) Bindungen

Diese Bindungen werden zwischen einem elektropositiven Element der dritten Reihe und einem elektronegativen Stickstoffatom gebildet. Daher sollte es einige Ähnlichkeiten und beobachtbare Trends in den elektronischen Eigenschaften geben. Die detaillierte Untersuchung der Elektronendichteverteilung erlaubt weiterhin eine klare Klassifizierung dieser Bindungen. Ein positiver Wert für den Laplacian, wie er in der gesamten Bindungsregion der untersuchten Al–N und Si–N Bindungen gefunden wurde, ist ein Zeichen für die Dominanz ionischer Wechselwirkungen. Die sphärische Verteilung der Ladungskonzentrationen um das Stickstoffatom und das Verhältnis $|\lambda_1|/\lambda_3$ unterstreichen diese Annahme für die Al–N Bindung in Verbindung **V**. Die Höhe der Elektronendichte am BCP und ein leicht negativer Wert für die Energiedichte an diesem Punkt weisen auf einen kleinen kovalenten Anteil hin. Die ionischen Wechselwirkungen sind immer noch die dominierende Kraft in den untersuchten Si–N Bindungen in **III–V**. Allerdings weisen der stärker negative Wert der Energiedichte zusammen mit einem höheren Betrag der Elektronendichte im Bindungsbereich auf einen höheren kovalenten Anteil als in der Al–N Bindung hin.

Die Untersuchung der dativen N→Si Bindung im metallorganischen Komplex mit hexakoordiniertem Silicium, **VI**, dokumentiert signifikante Unterschiede zu den Si–N Bindungen in **III–V**. Die Höhe der Elektronendichte auf dem Bindungspfad der dativen Bindung ist verglichen mit der in den Cyclosilazanen nur halb so hoch, die Energiedichte ist fast null und das Verhältnis $|\lambda_1|/\lambda_3$ ist mit 0.2 viel kleiner. Die Summe dieser Eigenschaften belegt, zusammen mit einem positiven Laplacian in der Bindungsregion, eine absolute Dominanz des ionischen Charakters in dieser dativen N→Si Bindung. Der kovalente Beitrag, der sich aus den topologischen Eigenschaften der Daten aus dem Röntgenbeugungsexperiments ergibt, ist sehr klein. Dieses Ergebnis zusammen mit dem ausgeprägt ionischen Charakter der Si–O und Si–F Bindung und der positiven Ladung aus der Integration des Siliciumbasins führen zu der

Schlussfolgerung, dass das hexakoordinierte Siliciumatom in **VI** nicht als hypervalent eingestuft werden sollte.

Die topologische Analyse der P–N Bindung im lithiierten Picolylphosphan **VII** klassifiziert diese als kovalente Einfachbindung, die durch elektrostatische Wechselwirkungen verkürzt wird. Die Ladungskonzentrationen in der Bindungsregion sind immer noch auf das Basin des Stickstoffs begrenzt, allerdings sind die Werte für die Energiedichte und die hohe Elektronendichte am BCP typisch für eine kovalente Einfachbindung. Außerdem beweist die Ermittlung von vier Maxima im Laplacian der Valenzschale des Phosphors eindeutig den sp^3 Charakter dieses Atoms. Daher ist die Formulierung einer P=N Doppelbindung, deduziert aus dem kurzen Bindungsabstand, nicht gerechtfertigt. Folglich kann Hypervalenz für das Phosphoratom ausgeschlossen werden.

Klassifizierung der Li–E' (E' = C, N, O) Bindungen

Die Ergebnisse der topologischen Analysen dieser drei Metall–Nichtmetall-Bindungstypen erlauben eine klare Interpretation der Wechselwirkungen: sie sind fast ausschließlich ionisch. Der kovalente Beitrag ist vernachlässigbar. Die Unterschiede der elektronischen Eigenschaften in den Bindungsregionen der untersuchten Li–C, Li–N und Li–O Bindungen sind relativ klein. Die stärksten elektrostatischen Wechselwirkungen werden für die Li–O Bindung gefunden, da sich die höchsten Ladungsdichtekonzentrationen um das Sauerstoffatom befinden. Jede der ausgewerteten Eigenschaften unterstützt die Klassifizierung als geschlossenschalige Wechselwirkung. Der Laplacian und die Energiedichte sind positiv, das Verhältnis $|\lambda_1|/\lambda_3$ ist kleiner als 0.21 in allen Li–E' Bindungen und die Elektronendichte am BCP überall im Bereich von $0.2e\text{\AA}^{-3}$. Diese topologischen Eigenschaften liegen im Bereich der Werte, die für die Bindung in Kochsalz angegeben werden. Weiterhin deuten die Ergebnisse der Integrationen der atomaren Basins der Lithiumkationen in den Verbindungen **IV**, **V**, **VII** und **VIII** darauf hin, dass der Ladungstransfer der Donorbasen zum Lithiumkation überall nur schwach ausgeprägt ist.

Alle Ergebnisse zeigen, dass Untersuchungen der Ladungsdichteverteilung ein leistungsfähiges Werkzeug sind, um den Bindungscharakter stark polarer Bindungen aufzuklären. Die Bindungsverhältnisse werden dabei auf der Basis von elektronischen Eigenschaften beschrieben, die weit über den bloßen Vergleich von Bindungslängen und -winkeln hinausgehen. Die topologischen Analysen, basierend auf experimentellen

Röntgenbeugungsdaten, liefern Informationen für eine exakte Klassifizierung aller untersuchten polaren Bindungen. Dabei hat sich herausgestellt, dass ionische Beiträge in fast allen Bindungen dominieren. Sorgfältiger Einsatz von Constraints erlaubt die Anwendung des Multipolmodells sogar für Problemstrukturen.

Ausblick

Die vorliegende Arbeit belegt, dass experimentelle Ladungsdichteuntersuchungen an polaren Bindungen von Elementen der dritten Periode aussagekräftige Ergebnisse liefern. Gleiches gilt für die Metal–Nichtmetall-Bindung. Hier liegt ein besonders großes Potential der Methode, da die Kenntnis der Elektronendichteverteilung in reaktiven metallorganischen Molekülen das rationale Design erleichtert und die Reaktivität zu einer graduell regelbaren Größe macht. An zwei Beispielen in der Arbeit konnte gezeigt werden, dass sogar verzwillingte Kristalle und fehlgeordnete Strukturen tragfähige topologische Analysen liefern, wenn die Constraints der lokalen Symmetrie sorgfältig angepasst werden. Trotz der vorhandenen Grenzen zeigen diese Ergebnisse den Weg für zukünftige Programmentwicklungen. Die Methode wird somit nicht mehr nur auf „ideale“ sondern auch auf „reale“ Einkristalle anwendbar sein. Die noch vorherrschende Multipolverfeinerung und topologische Analyse kleiner organischer Modellverbindungen wird der Vergangenheit angehören, da zunehmend chemisch relevante Systeme zugänglich sind.

8 References

- 1 W. C. Röntgen, Über eine neue Art von Strahlung. Vorläufige Mitteilung. *Sitzungsberichte der Physikalisch-Medizinischen Gesellschaft zu Würzburg*, 1895.
- 2 W. H. Bragg, W. L. Bragg, The reflection of X-rays by crystals, *Proc. R. Soc. Lond.*, **1913**, A88, 428.
- 3 (a) T. Kottke, D. Stalke, *J. Appl. Crystallogr.* **1993**, 26, 615. (b) T. Kottke, R. J. Lagow, D. Stalke, *J. Appl. Crystallogr.* **1996**, 29, 465. (c) D. Stalke, *Chem. Soc. Rev.* **1998**, 27, 171.
- 4 F. L. Hirshfeld, *Acta Crystallogr.* **1971**, B27, 769.
- 5 N. K. Hansen, P. Coppens, *Acta Crystallogr.* **1978**, A34, 909.
- 6 P. Coppens, *X-Ray Charge Densities and Chemical Bonding*, Oxford University Press, Oxford and New York, 1997.
- 7 M. A. Spackman, A. S. Brown, Charge Densities from X-ray Diffraction Data. In *Annual Reports on the Progress of Chemistry*, vol. 91 of *Physical Chemistry, Section C*. The Royal Society of Chemistry, Cambridge, 1994, 175.
- 8 T. S. Koritsanszky, P. Coppens, *Chem. Rev.* **2001**, 101, 1568.
- 9 R. F. W. Bader, *Atoms in Molecules: A Quantum Theory*, Oxford University Press, Oxford, 1990.
- 10 D. Leusser, PhD thesis, Universität Würzburg, **2002**.
- 11 D. Leusser, B. Walfort, D. Stalke, *Angew. Chem. Int. Ed.* **2002**, 41, 2079.
- 12 (a) W. Kutzelnigg, *Angew. Chem.* **1984**, 96, 262; *Angew. Chem. Int. Ed. Engl.* **1984**, 23, 272; (b) A. E. Reed, P. v. R. Schleyer, *J. Am. Chem. Soc.* **1990**, 112, 1434; (c) J. A. Dobado, H. Martinez-García, J. M. Molina, M. R. Sundberg, *J. Am. Chem. Soc.* **1998**, 120, 8461; (d) D. B. Chesnut, *J. Phys. Chem. A* **2003**, 107, 4307.
- 13 (a) D. S. Yufit, J. A. K. Howard, M. G. Davidson, *J. Chem. Soc., Perkin Trans.*, 2, **2000**, 249; (b) S. Pillet, M. Souhassou, Y. Pontillon, A. Caneschi, D. Gatteschi, C. Lecomte, *New. J. Chem.* **2001**, 25, 131.

- 14 G. S. Smith, L. E. Alexander, *Acta Crystallogr.* **1963**, *16*, 1015.
- 15 (a) D. Seyferth, G. Wiseman, *J. Am. Ceram. Soc.* **1984**, *67*, C132. (b) Y. D. Blum, K. B. Schwarz, R. M. Laine, *J. Mat. Sci.* **1989**, *24* 1707. (c) G. E. Legrow, T. F. Lim, J. Lipowitz, R. S. Reaach, *Am. Ceram. Soc. Bull.* **1987**, *60*, 363. (d) R. Riedel, M. Seher, G. Becker, *J. Eur. Ceram. Soc.* **1989**, *5*, 113.
- 16 E. Werner, U. Klingebiel, F. Pauer, D. Stalke, R. Riedel, S. Schaible, *Z. Anorg. Allg. Chem.* **1991**, *596*, 35.
- 17 W. Schnick, H. Huppertz, *Chem. J. Eur.* **1997**, *3*, 679.
- 18 K. Dippel, U. Klingebiel, M. Noltemeyer, F. Pauer, G. M. Sheldrick, *Angew. Chem.* **1988**, *100*, 1093.
- 19 T. Kottke, D. Stalke, *Organometallics* **1996**, *15*, 4552.
- 20 (a) R. R. Holmes, *Chem. Rev.*, 1996, Rev. 96, 927; (b) D. Kost, I. Kalikhman in *Chemistry of Organosilicon Compounds*; Wiley, Chichester, 1998. (c) D. Kost, V. Kingston, B. Gostevskii, A. Ellern, D. Stalke, B. Walfort, I. Kalikhman, *Organometallics* **2002**, *21*, 2293. (d) D. Kost, B. Gostevskii, N. Kocher, D. Stalke, I. Kalikhman, *Angew. Chem. Int. Ed.* **2003**, *42*, 1023.
- 21 I. Kalikhman, B. Gostevskii, O. Girshberg, A. Sivaramakrishna, N. Kocher, D. Stalke, D. Kost, *J. Organomet. Chem.*, in press.
- 22 (a) C. Chuit, R. J. P. Corriu, C. Reye, J. C. Young, *Chem. Rev.* **1993**, *93*, 1371. (b) G. P. Schiemenez, B. Schiemenez, S. Petersen, C. Wolff, *Chirality*. **1998**, *10*, 180.
- 23 G. Wittig, G. Geissler, *Justus Liebigs Ann. Chem.* **1953**, *580*, 44.
- 24 H. Staudinger, J. Meyer, *Helv. Chim. Acta* **1919**, *2*, 635.
- 25 A. W. Johnson, *Ylides and Imines of Phosphorus*, Wiley, New York 1993.
- 26 K. Dehnicke, F. Weller, J. Strähle, *Chem. Soc. Rev.* **2001**, *30*, 125.
- 27 K. Dehnicke, M. Krieger, W. Massa, *Coord. Chem. Rev.* **1999**, *182*, 19.
- 28 (a) D. W. Stephan, J. C. Stewart, F. Guerin, S. Courtenay, J. Kickham, E. Hollink, C. Beddie, A. Hoskin, T. Graham, P. Wie, R. E. v. H. Spence, W. Xu, L. Koch, X. Gao, D. G. Harrison, *Organometallics* **2003**, *22*, 1937-1947; (b) R. E. v. H. Spence, S. J. Brown, R. P. Wurz, D. Jeremic, D. W. Stephan, *PCT Int. Appl.* **2001**, WO 2000-CA978 20000824; CA 99-2282070.
- 29 D. G. Gilheany, *Chem. Rev.* **1994**, *94*, 1339.

- 30 G. Fries, J. Wolf, M. Pfeiffer, D. Stalke, H. Werner, *Angew. Chem. Int. Ed.* **2000**, 39, 564.
- 31 (a) A. Steiner, D. Stalke, *Angew. Chem. Int. Ed. Engl.* **1995**, 34, 1752; (b) S. Wingerter, M. Pfeiffer, A. Murso, C. Lustig, T. Stey, V. Chandrasekhar, D. Stalke, *J. Am. Chem. Soc.* **2001**, 123, 1381.
- 32 F. Baier, Z. Fei, H. Gornitzka, A. Murso, S. Neufeld, M. Pfeiffer, I. Rüdenauer, A. Steiner, T. Stey, D. Stalke, *J. Organomet. Chem.* **2002**, 661, 111.
- 33 (a) M. Albrecht, G. van Koten, *Angew. Chem.* **2001**, 113, 3866; *Angew. Chem. Int. Ed.* **2001**, 40, 3750; (b) H. Hagen, J. Boersma, G. van Koten, *Chem. Soc. Rev.* **2002**, 31, 357.
- 34 N. Kocher, D. Leusser, A. Murso, D. Stalke, *Angew. Chem. Int. Ed.*, submitted.
- 35 W. Scherer, P. Sirsch, D. Shorokhov, G. S. Mc grady, S. A. Mason, M. Gardiner, *Chem. Eur. J.* **2002**, 8, 2324.
- 36 (a) E. Kaufmann, K. Raghavachari, A. E. Reed, P. von P. Schleyer, *Organometallics* **1988**, 7, 1597; (b) F. M. Bickelhaupt, N. J. R. van Eikema Hommes, C. F. Guerra, E. J. Baerends, *Organometallics* **1996**, 15, 2923.
- 37 C. Strohmann, T. Seibel, K. Strohfeldt, *Angew. Chem. Int. Ed.* **2003**, 42, 4531.
- 38 M. Born, *Z. Physik* **1926**, 38, 803.
- 39 R. F. Stewart, D. Feil, *Acta Crystallogr.* **1980**, A36, 503.
- 40 C. A. Coulson, M. W. Thomas, *Acta Crystallogr.* **1971**, B27, 1354.
- 41 C. K. Johnson, H. A. Levy, *International Tables for X-Ray Crystallography, Vol. 4*, Kynoch Press, Birmingham, 1974.
- 42 P. Coppens, in *Neutron Diffraction*, H. Dachs (ed.), *Top. Curr. Phys.* 6, Springer Verlag, Berlin, 1978.
- 43 G. A. Jeffrey, D. W. J. Cruickshank, *Quart. Rev. Chem. Soc. London* **1953**, 7, 335.
- 44 a) P. Coppens, M. S. Lehmann, *Acta Cryst.* **1976**, B32, 1777; b) M. S. Lehmann, P. Coppens, *Acta Chem. Scand.* **1977**, A31, 530.
- 45 a) R. F. Stewart, *J. Chem. Phys.* **1968**, 48, 4882. b) R. F. Stewart, *J. Chem. Phys.* **1969**, 51, 4569. c) R. F. Stewart, *J. Chem. Phys.* **1973**, 58, 1668. d) R. F. Stewart, *J. Chem. Phys. Lett.* **1979**, 65, 5335.

- 46 T. Koritsanszky, S. Howard, P. R. Mallinson, Z. Su, T. Richter, N.K. Hansen, *XD - A Computer Program Package for Multipole Refinement and Analysis of Electron Densities from Diffraction Data*, Berlin **1996**.
- 47 E. Clementi, D. L. Raimondi, *J. Chem. Phys.* **1963**, *38*, 2686.
- 48 E. Clementi, C. Roetti, *At. Data Nucl. Data Tables* **1974**, *14*, 177.
- 49 Z. Su, P. Coppens, *Acta Crystallogr.* **1998**, *A54*, 646.
- 50 J. D. Dunitz, W. B. Schweizer, P. Seiler, *J. Am. Chem. Soc.* **1983**, *105*, 7056.
- 51 J. M. Savariault, M. S. Lehmann, *J. Am. Chem. Soc.* **1980**, *102*, 1298.
- 52 Z. Su, P. Coppens, *Acta Crystallogr.* **1992**, *A48*, 188.
- 53 M. A. Spackman, *Chem. Rev.* **1992**, *92*, 1769.
- 54 W. D. Arnold, L. K. Sanders, G. Wu, P. Coppens, E. Oldfield, *J. Am. Chem. Soc.* **2000**, *122*, 4708.
- 55 free from: R. J. Gillespie, P. A. Popelier, *Chemical Bonding and Molecular Geometry*, Oxford University Press, New York, 2001.
- 56 G. N- Lewis, *J. Am. Chem. Soc.* **1916**, *38*, 762.
- 57 a) R. J. Gillespie, I. Hargittai, *The VSEPR Model of Molecular Geometry*; Allyn and Bacon: Boston **1991**; b) R. J. Gillespie, *Molecular Geometry*; Reinhold Van Nostrand: London 1972; c) I. Bytheway, R. J. Gillespie, T.-H. Tang, R. F. W. Bader, *Inorg. Chem.* **1995**, *34*, 2407. d) R. J. Gillespie, E. A. Robinson, *Angew. Chem.* **1996**, *108*, 539; *Angew. Chem. Int. Ed. Engl.* **1996**, *35*, 477.
- 58 R. F. W. Bader, P. M. Beddall, *J. Chem. Phys.* **1972**, *56*, 3320.
- 59 D. A. Kirzhnits, *Sov. Phys. – JEPT*, **1957**, *32*, 115.
- 60 a) D. Cremer, E. Kraka, *Angew. Chem.* **1984**, *96*, 612; b) R. G. A. Bone, R. F. W. Bader, *J. Phys. Chem.* **1996**, *B100*, 10892.
- 61 A. Volkov, C. Gatti, Y. A. Abramov, *Acta Crystallogr.* **2000**, *A56*, 252.
- 62 A. Volkov, C. Gatti, private communication.
- 63 based on a talk from C. Gatti at the XD-workshop in Buffalo, May 2003.
- 64 A. Stash, V. Tsirelson, *WINXPRO: a Program for Calculating Crystal and Molecular Properties Usign Multipole Parameters of the Electron Density*. *J. Appl. Cryst.* **2002**, *35*, 371.

- 65 (a) C. Chuit, R. J. P. Corriu, A. Mehdi, C. Reye, *Angew. Chem. Int. Ed.* **1993**, 32, 1311; (b) C. Chuit, R. J. P. Corriu, C. Reye, *Chemistry of hypervalent compounds* **1999**, 81.
- 66 M. Tafipolsky, W. Scherer, K. Oefele, G. Artus, B. Pedersen, W. A. Herrmann, G. S. McGrady, *J. Am. Chem. Soc.* **2002**, 124, 5865.
- 67 W. Scherer, M. Spiegler, B. Pedersen, M. Tafipolsky, W. Hieringer, B. Reinhard, A. J. Downs, G. S. McGrady, *J. Chem. Soc. Chem. Commun.* **2000**, 635.
- 68 J. R. Cheeseman, M. T. Carroll, R. W. F. Bader, *Chem. Phys. Lett.* **1988**, 143, 451.
- 69 K. B. Wiberg, P. R. Rablen, *J. Comput. Chem.* **1993**, 14, 1504.
- 70 M. Messerschmidt, A. Wagner, M. W. Wong, P. Luger, *J. Am. Chem. Soc.* **2002**, 124, 732.
- 71 Bruker Nonius Inc., *SMART-NT: Program for Diffractometer Controlling*, Madison WI **2000**.
- 72 Bruker Nonius Inc., *SAINT-NT: Program for Integration of Diffraction Data from Area Detectors*, Madison WI **2000**.
- 73 G. M. Sheldrick, *SADABS 2.05: Program for Area Detector Absorption Correction*, University of Göttingen, **2002**.
- 74 L. J. Farrugia, *J. Appl. Cryst.* **1999**, 32, 837.
- 75 B. Blessing, *Acta Crystallogr.* **1995**, A51, 33.
- 76 Bruker Nonius Inc., *SHELXTL-97*, Madison, WI, **1997**.
- 77 D. Leusser, *BATCH - Program for Batch Number Assignment*, Universität Würzburg, **2000**.
- 78 G. M. Sheldrick, *Acta Crystallogr.* **1990**, A46, 467.
- 79 G. M. Sheldrick, *SHELXL-97 – Program for Structure Refinement*, Universität Göttingen, **1997**.
- 80 A. Volkov, Y. Abramov, P. Coppens, C. Gatti, *Acta Crystallogr.* **2000**, A56, 332.
- 81 F. A. Allen, *Acta Crystallogr.* **1986**, B42, 515.
- 82 E. Espinosa, E. Molins, C. Lecomte, *Phys. Rev.* **1997**, B56, 1820.
- 83 G. R. Moss, M. Souhassou, R. H. Blessing, *Acta Crystallogr.* **1995**, B51, 650.
- 84 A. Volkov, Y. A. Abramov, P. Coppens, *Acta Crystallogr.* **2000**, A57, 272.

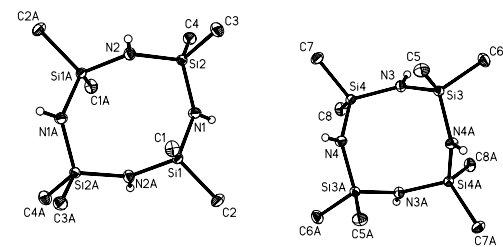
- 85 There is a controversial debate about the weighting scheme in a multipole refinement, especially in a discussion group in the internet; nevertheless, to date, almost all research groups use statistical weights in their refinements.
- 86 Systematical errors (e.g. affecting weak reflections in shells with $d < 0.5 \text{ \AA}^{-1}$) are not recognised if the weighting scheme is adjusted and thus introduced in the refinement.
- 87 F. L. Hirshfeld, *Acta Crystallogr.* **1976**, *A32*, 239.
- 88 T. Koritsanszky, J. Buschmann, D. Lentz, P. Luger, G. Perpetuo, M. Röttger, *Chem. Eur. J.* **1999**, *5*, 3413.
- 89 Bruker Nonius Inc., *RLATT: A program for Reciprocal Lattice Inspection*, Madison WI **2000**.
- 90 B. Waldorf, PhD Thesis, Universität Würzburg, **2001**.
- 91 E. Lippert, W. Lüder, F. Moll, W. Nägele, H. Boos, H. Prigge, I. Seibold-Blankenstein, *Angew. Chem.* **1961**, *73*, 695.
- 92 V. Schomaker, K. N. Trueblood, *Acta Crystallogr.* **1968**, *B24*, 63.
- 93 A. Volkov, Y. A. Abramov, P. Coppens, *Acta Crystallogr.* **2000**, *A57*, 272.
- 94 A. Heine, R. Herbst-Irmer, D. Stalke, K. A. Zachariasse, *Acta Crystallogr.* **1994**, *B50*, 363.
- 95 (a) H. D. Flack, *Acta Crystallogr.* **1983**, *A39*, 876. (b) G. Bernardinelli, H. D. Flack, *Acta Crystallogr.* **1985**, *A41*, 500; (c) H. D. Flack, G. Bernardinelli, *Acta Crystallogr.* **1999**, *A55*, 908; (d) H. D. Flack, G. Bernardinelli, *J. Appl. Cryst.* **2000**, *33*, 1143.
- 96 K. Rotkiewicz, K. H. Grellmann, Z. R. Grabowski, *Chem. Phys. Lett.* **1973**, *19*, 315.
- 97 I. Rückert, A. Demeter, O. Morawski, W. Kühnle, E. Tauer, K. A. Zachariasse, *J. Phys. Chem.* **1999**, *A103*, 1958.
- 98 (a) I. Rückert, A. Hebecker, A. B. J. Parusel, K. A. Zachariasse, *Z. Phys. Chem.* **2000**, *241*, 1597. (b) A. Demeter, S. Druzhinin, M. George, E. Haselbach, J. L. Roulin, K. A. Zachariasse, *Chem. Phys. Lett.* **2000**, *323*, 351.
- 99 M. Colapietro, A. Domenicano, C. Marciante, G. Portalone, *Acta Crystallogr.* **1981**, *B37*, 387.
- 100 P. Rademacher, In *Strukturen organischer Moleküle*, VCH, Weinheim / New York, 1987.

- 101 (a) G. R. Desiraju, T. Steiner, *The Weak Hydrogen Bond in Structural Chemistry and Biology*, Oxford University Press, Oxford, 1999; (b) T. Steiner, *Angew. Chem.* **2002**, *114*, 50.
- 102 Z. Fei, N. Kocher, C. J. Mohrschladt, H. Ihmels, D. Stalke, *Angew. Chem. Int. Ed.* **2003**, *42*, 783.
- 103 some related systems are published in: (a) S. T. Howard, M. B. Hursthouse, C. W. Lehmann, E. A. Poyner, *Acta Crystallogr.* **1995**, *B51*, 328. (b) F. Hamzaoui, F. Baert, G. Wojcik, *Acta Crystallogr.* **1996**, *B52*, 159. (c) J. R. Roubie, A. Galvao, *Acta Crystallogr.* **1995**, *B51*, 835. (d) R. F. Stuart in *The Application of Charge Density Research to Chemistry and Drug Design*, eds. G.A. Jeffrey and J. F. Piniella, NATO ASI Series, *Vol. B250*, **1991**, Plenum Press, NY, 63-101. A much more detailed list is presented in the review: M. A. Spackman, *Annu. Rep. Chem., Sect. C: Phys. Chem.* **1998**, *94*, 177.
- 104 A. Bach, D. Lentz, P. Luger, *J. Phys. Chem. A* **2001**, *105*, 7405.
- 105 U. Koch, P. L. A. Popelier, *J. Chem. Phys.* **1995**, *99*, 9747.
- 106 especially to results of other studies in our research group.
- 107 (a) D. E. Hibbs, C. J. Austin-Woods, J. A. Platts, J. Overgaard, P. Turner, *Chem. Eur. J.* **2003**, *9*, 1075; (b) Y. Abramov, A. Volkov, P. Coppens, *Chem. Phys. Lett.* **1999**, *311*, 81; (c) A. Wagner, R. Flaig, D. Zobel, B. Dittrich, P. Bombicz, M. Strümpel, P. Luger, *J. Phys. Chem. A* **2002**, *106*, 6581.
- 108 This is the opinion of the author, some scientists working in this field state, refining the κ' parameters in a refinement based on experimental data would only introduce bias and not lead to meaningful values. In their opinion only refinements from theoretical data leads to reasonable figures. Unfortunately, theoretical data are not available – the compounds in this thesis are either too large or refinement does not converge.
- 109 (a) S. Larsen, C. Flensburg, H. S. Bengacted, H. O. Sorensen, *Acta Crystallogr.* **1999**, *A55*, 38; (b) J. Buschmann, T. Koritsanszky, D. Lentz, P. Luger, N. Nickelt, S. Willemsen, *Z. Kristallogr.* **2000**, *215*, 487.
- 110 A. Volkov, Y. Abramov, P. Coppens, C. Gatti, *Acta Crystallogr.* **2000**, *A56*, 332.
- 111 Cambridge Structural Database (CSD), Version 5.24, Nov **2002**.
- 112 C. Glidewell, C. Thomson, *J. Comput. Chem.* **1982**, *3*, 495.
- 113 R. D. Shannon, C. T. Prewitt, *Acta Crystallogr.* **1976**, *A32*, 751.

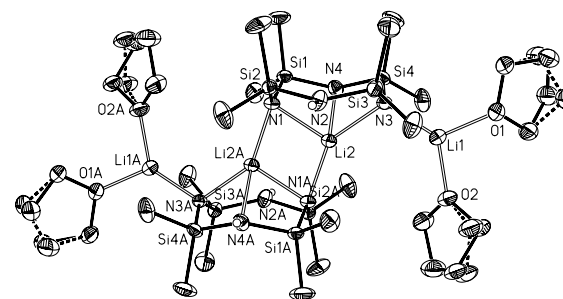
- 114 T. Stey, D. Stalke, *Lead structures in lithium organic chemistry*, in Z. Rappoport I. Marek (Eds), *The chemistry of organolithium compounds*, Wiley, 2003.
- 115 (a) K. Dippel, U. Klingebiel, T. Kottke, F. Pauer, G. M. Sheldrick, D. Stalke, Z. *Anorg. Allg. Chem.* **1990**, 584, 87; (b) U. Klingebiel, M. Noltemeyer, H. J. Rakebrandt, Z. *Naturforsch.* **1997**, B52, 775.
- 116 W. Scherer, P. Sirsch, M. Grosche, M. Spiegler, S. A. Manson, M. G. Gardiner, *Chem. Commun.* **2001**, 2072.
- 117 B. Dittrich T. Koritsanszky, M. Grosche, W. Scherer, R. Flaig, A. Wagner, H. G. Krane, H. Kessler, C. Riemer, A. M. M. Schreurs, P. Luger, *Acta Crystallogr.* **2002**, B58, 721.
- 118 see e. g. S. Kuntzinger, N. E. Ghermani, Y. Dusauroy, C. Lecomte, *Acta Crystallogr.* **1998**, B54, 819.
- 119 H. Buerger, U. Götze, W. Sadowny, *Spectrochimica Acta* **1970**, A26, 671.
- 120 R. W. F. Bader, T. S. Slee, D. Cremer, E. Kraka, *J. Am. Chem. Soc.* **1983**, 105, 5061.
- 121 Y. A. Abramov, *Acta Crystallogr.* **1997**, A53, 264.
- 122 The formerly identical number of atoms in **IV** and **V** increases in **IV** due to the two disordered THF groups (26 additional atoms).
- 123 (a) R. Flaig, T. Koritsansky, R. Soyka, L. Häming, P. Luger, *Angew. Chem.* **2001**, 113, 368; (b) R. Flaig, T. Koritsanszky, B. Dittrich, A. Wagner, P. Luger, *J. Am. Chem. Soc.* **2002**, 124, 3407.
- 124 T. Koritsanszky, R. Flaig, D. Zobel, H.-G. Krane, W. Morgenroth, P. Luger, *Science* **1998**, 276, 356.
- 125 For reviews on hypercoordinated silicon atoms see: (a) R. R. Holmes, *Chem. Rev.* **1996**, 96, 927; (b) C. Chuit, R. J. P. Corriu, C. Reye, J. C. Young, *Chem. Rev.* **1993**, 93, 1371; (c) M. Kira, L. C. Zhang, in: Kin Ya Akiba (Ed.), *The Chemistry of Hypervalent Compounds*, Wiley-VCH, Weinheim, Germany, 1999, 147, (d) D. Kost, I. Kalikhman, *Adv. Organomet. Chem.*, in press.
- 126 R. Tacke, M. Pülm, B. Wagner, *Adv. Organomet. Chem.* **1999**, 44, 221.
- 127 The geometrical parameters of the molecular structure discussion are again based on a data set up to a diffraction angle of $\sin\theta/\lambda = 1.14\text{\AA}^{-1}$; the angles and bond lengths are taken from the results of the multipole refinement.

- 128 (a) D. Kost, V. Kingston, B. Gostevskii, A. Ellern, D. Stalke, B. Walfort, I. Kalikhman, *Organometallics* **2002**, *21*, 2293; (b) I. Kalikhman, B. Gostevskii, O. Grishberg, S. Krivonos, D. Kost, *Organometallics*, 2002, *21*, 2551; (c) D. Kost, B. Gostevskii, N. Kocher, D. Stalke, I. Kalikhman, *Angew. Chem., Int. Ed. Engl.* **2003**, *42*, 1023.
- 129 D. Kost, I. Kalikhman, S. Krivonos, D. Stalke, T. Kottke, *J. Am. Chem. Soc.* **1998**, *120*, 4209.
- 130 J. Wang; L. A. Eriksson, R. J. Boyd, Z. Shi, *J. Phys. Chem.* **1994**, *98*, 1844.
- 131 J. R. Herster, E. N. Maslen, *Acta Crystallogr.* **1995**, *B51*, 913.
- 132 V. Jonas, G. Frenking, M. T. Reetz, *J. Am. Chem. Soc.* **1994**, *116*, 8741.
- 133 D. B. Chesnut, *Chem. Phys.* **2003**, *291*, 141.
- 134 R.F.W. Bader, H. J. Essen, *J. Chem. Phys.* **1984**, *80*, 1943.
- 135 P. Fuhrmann, T. Koritsanszky, P. Luger, *Z. Kristallogr.* **1997**, *212*, 213.
- 136 M. Kubicki, T. Borowiak, G. Dutkiewicz, M. Souhassou, C. Jelsch, C. Lecomte, *J. Phys. Chem. B* **2002**, *106*, 3706.
- 137 S. T. Howard, M. B. Hursthouse, L. W. Lehmann, *Acta Crystallogr.* **1995**, *B51*, 328.
- 138 (a) A. Steiner, D. Stalke, *J. Chem. Soc. Chem. Commun.* **1993**, 444; (b) H. Gornitzka, D. Stalke, *Angew. Chem.* **1994**, *106*, 695; *Angew. Chem. Int. Ed. Engl.* **1994**, *33*, 693; (c) A. Steiner, D. Stalke, *Organometallics* **1995**, *14*, 2422.
- 139 M. T. Gamer, P. W. Roesky, *Z. Anorg. Allg. Chem.* **2001**, *627*, 877.
- 140 R. P. Kamalesh Babu, K. Aparna, R. McDonald, R. G. Cavell, *Organometallics* **2001**, *20*, 1451.
- 141 (a) K. Gregory, P. v. R. Schleyer, R. Snaith, *Adv. Inorg. Chem.* **1991**, *37*, 47; (b) R. E. Mulvey, *Chem. Soc. Rev.* **1998**, *27*, 339.
- 142 P. B. Hitchcock, M. F. Lappert, Z.-X. Wang, *J. Chem. Soc. Chem. Commun.* **1997**, 1113.
- 143 T. Chivers, A. Downard, M. Parvez, *Inorg. Chem.* **1999**, *38*, 4347.
- 144 (a) A. Steiner, D. Stalke, *Inorg. Chem.* **1993**, *32*, 1977; (b) R. Fleischer, D. Stalke, *Inorg. Chem.* **1997**, *36*, 2413; (c) A. Steiner, S. Zacchini, P. I. Richards, *Coord. Chem. Rev.* **2002**, *227*, 193.

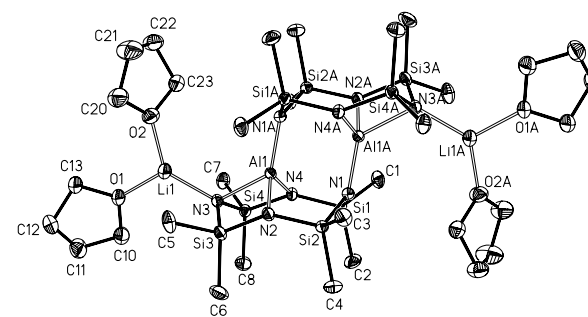
-
- 145 Y. A. Abramov, L. Brammer, W. T. Klooster, R. M. Bullock, *Inorg. Chem.* **1998**, 37, 6317.
- 146 Value of the electronic energy density at the BCP for the S1–N1 bond in Sulfurdiimide S(N^tBu)₂.
- 147 (a) T. Kottke, D. Stalke, *Angew. Chem.* **1993**, 105, 619; *Angew. Chem. Int. Ed. Engl.* **1993**, 32, 580; (b) M. A. Nichols, P. G. Willard, *J. Am. Chem. Soc.* **1993**, 115, 1568; (c) N. D. R. Barnett, R. E. Mulvey, *J. Am. Chem. Soc.* **1993**, 115, 1573.
- 148 see e. g. (a) G. Boche, M. Marsch, J. Harbach, K. Harms, B. Ledig, F. Schugert, J. C. W. Lohrenz, H. Ahlbrecht, *Chem. Ber.* **1993**, 126, 1887; (b) D. J. Pippel, G. A. Weisenburger, S. R. Wilson, P. Beak, *Angew. Chem. Int. Ed.* **1998**, 37, 2522.



III



IV



V

Publikationen

1. I. Fernandez, G. Alvarez, M. Julia, N. Kocher, D. Leusser, D. Stalke, J. Gonzalez, L. F. Ortiz, „[Li{CH(Me)P(Ph)₂(NCO₂Me)}₂(THF)₂]: Crystal, Solution, and Calculated Structure of a N-Delocalized Lithium Phosphazene“, *J. Am. Chem. Soc.* **2002**, *124*, 15184-15185.
2. Z. Fei, N. Kocher, C. J. Mohrschladt, H. Ihmels, D. Stalke, „Single Crystals of the Disubstituted Anthracene 9,10-(Ph₂P=S)₂C₁₄H₈ Selectively and Reversibly Detect Toluene by Solid-State Fluorescence Emission“, *Angew. Chem. Int. Ed.* **2003**, *42*, 783-787.
3. D. Kost, B. Gostevskii, N. Kocher, D. Stalke; I. Kalikhman, „An Unexpected, Sterically Driven, Methyl Halide Elimination in Pentacoordinate Siliconium Halide Salts: Silicon Complexes with Equatorial Nitrogen Coordination“, *Angew. Chem. Int. Ed.*, **2003**, *42*, 1023-1026.
4. I. Kalikhman, B. Gostevskii, O. Girshberg, A. Sivaramakrishna, N. Kocher, D. Stalke, D. Kost, „Donor-Stabilized Silyl Cations. Part 7: Neutral Hexacoordinate and Ionic Pentacoordinate Silicon Chelates with N-Isopropylideneimino-Acylimidato ligands“, *J. Org. Chem.* **2003**, *686*, 202-214.
5. D. Leusser, J. Henn, N. Kocher, B. Engels, D. Stalke, „S=N versus S⁺-N⁻ - An Experimental Charge Density Study“, *J. Am. Chem. Soc.*, in press.
6. B. Gostevskii, K. Adair, A. Sivaramakrishna, D. Stalke, N. Kocher, I. Kalikhman, D. Kost, „Balance between Neutral and Ionic Dissociation Patterns in Hexacoordinated Silicon Chelates: a Model Nucleophilic Substitution at Pentacoordinated Silicon“, *Angew. Chem. Int. Ed.*, submitted.
7. N. Kocher, D. Leusser, A. Murso, D. Stalke, P=E versus P⁺-E⁻ (E = C, N) - Experimental Evidence against Hypervalent Phosphorus (V)“, *Angew. Chem. Int. Ed.*, submitted.
8. N. Kocher, J. Henn, B. Gostevskii, I. Kalikhman, D. Kost, B. Engels, D. Stalke, „Si-E (E = N, O, F) Bonding in a Hexacoordinated Silicon Complex – New Facts from Experimental and Theoretical Charge Density Studies“, *J. Am. Chem. Soc.*, submitted.

Posterpräsentationen

1. N. Kocher, C. Zachariasse, D. Stalke, „Charge Density Distribution in Donor Acceptor Molecules, 20th European Crystallographic Meeting **2001**, Krakau, Polen.
2. N. Kocher, D. Leusser, A. Murso, D. Stalke, „ Experimental Charge Density Study on a Lithiated Iminophosphorane, 3rd Alkchem Conference, **2003**, Würzburg, Deutschland.

Lebenslauf

Persönliche Daten

Name: Nikolaus Kocher
Geburtsdatum: 6. Mai 1973
Geburtsort: Gunzenhausen
Familienstand: ledig

Schulbildung

1979 – 1983 Grundschohle Großenried
1983 – 1984 Volksschule Bechhofen
1984 – 1993 Platen-Gymnasium Ansbach, Abschluss: Abitur

Grundwehrdienst

7/1993 – 6/1994 in Landshut

Studium

10/1994 – 7/2000 Studium der Biologie und Chemie (LAGym) an der Universität Würzburg
7/1998 – 1/1999 Zulassungsarbeit im Arbeitskreis Prof. Dr. D. Stalke am Institut für Anorganische Chemie der Universität Würzburg mit dem Titel:
Experimentelle Konzeptionierung des anorganisch-chemischen Fortgeschrittenenpraktikums „Studentische Projektarbeiten“ für StudentInnen des Lehramts an Gymnasien
7/2000 Studienabschluss: 1. Staatsexamen;
Gesamtnote Chemie: „sehr gut“
Gesamtnote Biologie: „gut“
seit 10/2000 Arbeiten an der Dissertation mit dem Titel:
Experimental Charge Density Studies of Highly Polar Bonds
im Arbeitskreis von Prof. Dr. D. Stalke am Institut für Anorganische Chemie der Universität Würzburg
seit 10/2000 Wissenschaftlicher Angestellter am Institut für Anorganische Chemie der Universität Würzburg